

# Parameter Estimation of the Global 21cm Signal

*Aryana Haghjoo*



Department of Physics  
McGill University  
Trottier Space Institute  
Montréal, Québec, Canada

August 2023

---

A thesis submitted to McGill University in partial fulfillment of the requirements of the degree of

*Master of Science in Physics*

©Aryana Haghjoo, 2023

# Abstract

The global 21cm signal has emerged as a new observable in cosmology and astrophysics, with the potential to provide insights into the study of the period between the end of the cosmic dark ages and the formation of the first stars and galaxies.

The 21cm signal is sensitive to the density and temperature of neutral hydrogen in the early universe and the presence of the first stars and galaxies. Therefore, any deviation from the predictions of the standard cosmological model of this signal could indicate the presence of new physics beyond the standard model of particle physics. In this study, we explore the potential of the global 21cm signal to reveal the signatures of non-standard physics through constraining the values of astrophysical parameters.

The literature review of this thesis provides an overview by exploring the physical principles, simulations, imprints of non-standard effects, and observation attempts of the global 21cm signal. The physical principles encompass the mechanisms forming the global 21cm signal and its evolution through cosmic history. Simulations play a pivotal role in generating models of the global 21cm signal, aiding in understanding the influence of

different astrophysical scenarios on the ultimate behavior of this signal. Furthermore, the effects of non-standard physics on the global 21cm signal are examined, including scenarios such as cosmic strings, exotic particle interactions, or different dark matter candidates. The review also explores ongoing efforts and challenges in observing the global 21cm signal and the complexities of foreground removal.

Furthermore, parameter estimation techniques are discussed, highlighting the methodologies employed to extract valuable astrophysical information from the observed 21cm data. Ultimately, this thesis focuses on a specific parameter estimation method, which adopts the combinations of Markov Chain Monte Carlo (MCMC) with the Levenberg-Marquardt (LM) algorithm to estimate the best-fit physical parameters of the 21cm curves. The Accelerated Reionization Era Simulations (ARES) are employed to generate theoretical models of the global 21cm signal.

The knowledge of these best-fit parameters is expected to assist in constraining future proposed models and set theoretical limits for the precision of upcoming experiments to observe desired non-standard effects.

# Résumé

Le signal global de 21cm est devenu une nouvelle observable en cosmologie et en astrophysique, avec le potentiel de fournir des informations sur l'étude de la fin des âges sombres cosmiques et la formation des premières étoiles et galaxies. l'âge sombre cosmique et la formation des premières étoiles et galaxies.

Le signal 21cm est sensible à la densité et à la température de l'hydrogène neutre dans l'univers primitif, ainsi qu'à la présence des premières étoiles et galaxies. Par conséquent, tout écart par rapport aux prédictions du modèle cosmologique standard de ce signal pourrait indiquer la présence d'une nouvelle physique au-delà du modèle standard de la physique des particules. Dans cette étude, nous explorons le potentiel du signal global 21cm pour révéler les signatures de la physique non-standard en contraintes sur les valeurs des paramètres astrophysiques.

La revue de la littérature de cette thèse offre une vue d'ensemble en explorant les principes physiques, les simulations, les empreintes d'effets non-standard et les tentatives d'observation du signal global de 21cm. Les principes physiques englobent les mécanismes formant le

signal global de 21cm et son évolution à travers l'histoire cosmique. Les simulations jouent un rôle essentiel dans la création de modèles du signal global 21cm, aidant à comprendre l'influence de différents scénarios astrophysiques sur le comportement final de ce signal. De plus, les effets de la physique non standard sur le signal global 21cm sont examinés, y compris des scénarios tels que les cordes cosmiques, les interactions de particules exotiques ou les différents candidats à la matière noire. La revue explore également les efforts et les défis actuels dans l'observation du signal global de 21cm ainsi que les complexités de l'élimination des interférences.

En outre, les techniques d'estimation des paramètres sont discutées, mettant en évidence les méthodologies utilisées pour extraire des informations astrophysiques précieuses à partir des données observées du 21cm. Finalement, cette thèse se concentre sur une méthode spécifique d'estimation des paramètres, qui associe les techniques de MCMC avec l'algorithme LM pour estimer les paramètres physiques en ajustant au mieux les courbes du 21cm. ARES sont utilisés pour générer des modèles théoriques du signal global 21cm.

La connaissance de ces paramètres les mieux ajustés devrait contribuer à restreindre les futurs modèles proposés et à établir des limites théoriques pour la précision des futures expériences visant à observer les effets non standard souhaités.

# Acknowledgements

I would like to express my gratitude to my supervisors, Jonathan Sievers and Oscar Hernández, for their invaluable help and patience throughout this project. I want to recognize the assistance provided by fellow members from both research teams, of which I was a part during my master's program. I must acknowledge Jordan Mirocha for developing the ARES code and responding to my questions on the specific applications of this package. I would like to thank the *Digital Research Alliance of Canada* for offering the computational resources needed for the analysis of this thesis.

I am deeply grateful to my parents for their unwavering support and enthusiasm. Even though we were thousands of kilometers apart, I could always rely on them being there for me. They kept me motivated during my hard days by reminding me of my reasons for pursuing physics academically. I wish one day I will be able to return their kindness.

Additionally, I want to thank my roommates and new friends in Montreal for the joyful moments, unique adventures, and wonderful experiences we shared. Our late-night scientific debates acted as an inspiration for my research.

Furthermore, I would like to acknowledge the significant role of the staff at McGill Wellness Hub. They kindly helped me overcome the health issues that I faced during my graduate journey. Their constant presence and willingness to support was a true blessing.

I learned a lot during the past two years, both scientifically and non-scientifically. To recap all the experiences in a sentence, I would say that pursuing this master's resulted in notable personal growth for the younger inexperienced version of me.

*To all lifelong learners and doers: you are changing the world every day!*

## Contribution of Authors

The author carried out all the work presented in chapters 4 and 5. She wrote the code to do the LM and MCMC fits, ran the ARES simulations, and carried out the MCMC fits to extract parameters. She also carried out the convergence tests and constrained cosmic dawn parameters based on EDGES data.



# Contents

<b>1</b>	<b>Introduction</b>	<b>1</b>
1.1	Background and Motivation . . . . .	2
1.2	Research Questions and Objectives . . . . .	3
1.3	Overview of The Thesis . . . . .	4
<b>2</b>	<b>The Global 21cm Signal</b>	<b>6</b>
2.1	Theoretical Basis of the 21cm Signal . . . . .	7
2.1.1	Physical Principles of The 21cm Spectral Line . . . . .	8
2.1.2	Wouthuysen-Field Coupling . . . . .	12
2.1.3	Sky-Averaged 21cm Signal . . . . .	13
2.2	Simulating the Global 21cm Signal . . . . .	16
2.2.1	21 Centimeter Fast Approximate Signal Toolbox (21cmFAST) . . . . .	19
2.2.2	The Accelerated Reionization Era Simulations (ARES) . . . . .	19
2.3	Signature of Non-Standard Physics . . . . .	20

---

2.3.1	Dark Matter (DM)	22
2.3.2	Cosmic Strings	25
<b>3</b>	<b>Observations of the Global 21cm Signal</b>	<b>29</b>
3.1	Challenges of Global 21cm Observations	30
3.1.1	Astronomical Foreground Emission	31
3.1.2	Ionospheric Effects	32
3.1.3	Radio Frequency Interference (RFI)	33
3.2	Global 21cm Experiments	34
3.3	On The Interpretation of EDGES Data	40
<b>4</b>	<b>Parameter Estimation Methods</b>	<b>43</b>
4.1	Levenberg-Marquardt (LM)	44
4.1.1	Covariance Matrix	45
4.1.2	Derivation of the Levenberg-Marquardt Algorithm	48
4.2	Markov Chain Monte Carlo (MCMC)	50
4.2.1	Convergence Test	51
4.3	Combination of MCMC and LM	52
4.3.1	Generating Correlated Noise	54
4.4	Algorithm Validation	55
4.4.1	The Chi-Square Consistency Test	55

4.4.2	The Chi-Square Parameter Correlation Test . . . . .	56
<b>5</b>	<b>Results and Analysis</b>	<b>64</b>
5.1	Key Astrophysical Parameters . . . . .	65
5.2	Parameter Estimation of Mock Data . . . . .	69
5.3	Parameter Estimation of EDGES data . . . . .	70
5.3.1	Error Bar Calculation . . . . .	71
5.3.2	Results . . . . .	72
<b>6</b>	<b>Summary and Conclusion</b>	<b>88</b>

# List of Figures

2.1	Spin-flip Transition of Neutral Hydrogen . . . . .	8
2.2	Time evolution of the global 21cm differential brightness temperature . . . .	17
2.3	Typical global 21cm curve generated using ARES . . . . .	21
2.4	Effect of different DM models on the global 21cm differential brightness temperature curve . . . . .	24
2.5	The global 21cm for different values of superconducting cosmic string tension	28
3.1	Results of EDGES Experiment . . . . .	41
4.1	Flow chart of LM . . . . .	57
4.2	Flow chart of MCMC . . . . .	58
4.3	An unconverged MCMC chain and its power spectrum . . . . .	59
4.4	A converged MCMC chain and its power spectrum . . . . .	59
4.5	Flow chart of the procedure to combine MCMC and LM . . . . .	60
4.6	Corner plots of an MCMC chain . . . . .	61

4.7	Histogram of disparity in the chi-square values of drawn samples . . . . .	62
4.8	Chi-Square vs. parameters plots . . . . .	63
5.1	Behaviour of global 21cm theoretical model with respect to underlying astrophysical parameters . . . . .	68
5.2	Results of fitting mock data . . . . .	74
5.3	Trend of parameters in the mock data MCMC chain . . . . .	75
5.4	Power spectrum of mock data MCMC chain . . . . .	76
5.5	Histogram of disparity in the chi-square of drawn samples for the mock data MCMC chain . . . . .	77
5.6	Chi-Square of Drawn samples as a function of parameter values for the mock data . . . . .	78
5.7	Chi-Square of Drawn samples as a function of parameter values for the mock data, zoomed version . . . . .	79
5.8	Corner plots of the mock data chain . . . . .	80
5.9	Results of fitting EDGES data . . . . .	81
5.10	Trend of parameters in the EDGES data MCMC chain . . . . .	82
5.11	Power spectrum of EDGES data MCMC chain . . . . .	83
5.12	Histogram of disparity in the Chi-Square of drawn samples for the data MCMC chain . . . . .	84

5.13	Chi-Square of Drawn samples as a function of parameter values for EDGES	
	data . . . . .	85
5.14	Chi-Square of Drawn samples as a function of parameter values for the EDGES	
	data, zoomed version . . . . .	86
5.15	Corner plots of the EDGES data MCMC chain . . . . .	87

## List of Tables

5.1	Results of fitting a mock data set . . . . .	71
5.2	Results of fitting EDGES data with MCMC chain . . . . .	74

# List of Acronyms

<b>21cmFAST</b>	21 Centimeter Fast Approximate Signal Toolbox.
<b>AGN</b>	Active Galactic Nuclei.
<b>ANN</b>	Artificial Neural Networks.
<b>ARES</b>	The Accelerated Reionization Era Simulations.
<b>BIGHORNS</b>	Broadband Instrument for Global HydrOgen ReioNisation Signal.
<b>CDM</b>	Cold Dark Matter.
<b>CMB</b>	cosmic microwave background.
<b>DLS</b>	Damped Least-Squares.
<b>DM</b>	Dark Matter.
<b>EDGES</b>	Experiment to Detect the Global EoR Signature.
<b>EoR</b>	Epoch of Reionization.
<b>FM</b>	Frequency Modulation.
<b>HYPERION</b>	Hydrogen Probe of the Epoch of REIONization.
<b>IGM</b>	Intergalactic Medium.



---

<b>LDM</b>	Light Dark Matter.
<b>LEDA</b>	Large aperture Experiment to Detect the Dark Ages.
<b>LM</b>	Levenberg-Marquardt.
<b>LWA</b>	Long Wavelength Array.
<b>Ly<math>\alpha</math></b>	Lyman $\alpha$ .
<b>MCMC</b>	Markov Chain Monte Carlo.
<b>MIST</b>	Mapper of the IGM Spin Temperature.
<b>OVRO</b>	Owen’s Valley Radio Observatory.
<b>PRI<sup>Z</sup>M</b>	Probing Radio Intensity at high-Z from Marion.
<b>REACH</b>	Radio Experiment for the Analysis of Cosmic Hydrogen.
<b>RFI</b>	Radio Frequency Interference.
<b>RTE</b>	Radiative Transfer Equation.
<b>SARAS</b>	Shaped Antenna measurement of background RAdio Spectrum.
<b>SCI-HI</b>	Small Radio Telescope for Cosmic Hydrogen Intensity Mapping.
<b>SED</b>	Spectral Energy Distribution.
<b>SFR</b>	Star Formation Rate.
<b>UV</b>	ultraviolet.
<b>WDM</b>	Warm Dark Matter.
<b>WF</b>	Wouthuysen–Field.

# Chapter 1

## Introduction

21cm cosmology is a relatively new window in the study of the universe during its early stages of evolution. Its applications range from the study of dark ages and cosmic dawn to cosmic structure formation [1]. The field holds great potential for revolutionizing our understanding of the first stars, galaxies, and black holes by leveraging the temporal and spatial information embedded in the cosmic 21cm signal [2].

In this chapter, our initial focus will be on providing a concise introduction to the global 21cm signal and its various applications. Subsequently, we will delve into the motivations for conducting this research. Lastly, within the final section of this chapter, we will provide an overview of all the materials furnished in this thesis.

## 1.1 Background and Motivation

The global 21cm signal is the average over the brightness temperature of the 21cm line across the entire sky. It is a measure of the overall state of the Intergalactic Medium (IGM) and presents itself as an excess absorption or emission in comparison to the cosmic microwave background (CMB). This radiation is a piece of observational evidence for certain characteristics of the IGM in the early universe (e.g., temperature, density, and ionization state). These properties are determined by the complex interplay between the cosmic radiation field, the formation and evolution of the first stars and galaxies, and the feedback processes that these sources exert on their surroundings [3].

Besides all the above-mentioned applications, the global 21cm signal is a **strong probe for non-standard physics** during the dark ages and Epoch of Reionization (EoR). It has the potential to shed light on mysteries surrounding dark matter/dark energy, the existence of cosmic strings, and even certain particle interactions (e.g., primordial electron-proton interactions) [4–8]<sup>1</sup>. This capacity of the global 21cm signal is the main motivation of this research.

---

<sup>1</sup>These effects will be discussed more in section 2.3.

## 1.2 Research Questions and Objectives

The effects of non-standard physics on 21cm signal have gained lots of attraction in the recent literature [5, 9–11]. These effects were investigated through the application of analytical and semi-analytical methods. However, the majority of these studies were predominantly analytical in nature, and the results were not evaluated against the observational data<sup>2</sup>. We aim to fill this research gap by continuing these semi-analytical efforts and analyzing them using the currently available observational data (Experiment to Detect the Global EoR Signature (EDGES) [12]). The ultimate goal is to introduce a generalized framework to probe these non-standard effects.

With the recently released data at our disposal (EDGES [12]), we use certain fitting algorithms (Levenberg-Marquardt (LM) and Markov Chain Monte Carlo (MCMC)) to compare them to theoretically simulated models provided by The Accelerated Reionization Era Simulations (ARES) [13]. The first step is to estimate the physical parameters of these curves by only taking the standard physics mechanisms into account.

In future studies, we will include a realistic foreground model and upgrade our simulator to include desired non-standard effects. We will again fit the observational data into the upgraded version of the theoretical model. This approach will allow us to investigate patterns of change in the best-fit physical parameters. The insights from this study will be used to constrain the physical parameters found by the newly proposed models. Moreover, it will

---

<sup>2</sup>For most of these studies, the appropriate observational data did not exist at the time of publications.

empower us to determine whether the upcoming radio interferometers have enough precision to detect our targeted non-standard effects.

## 1.3 Overview of The Thesis

This thesis consists of two major components: the literature review and the research.

In the literature review chapters (chapters 2 and 3), we first talk about the global 21cm signal and its physical principles. We continue by exploring the effects of non-standard physics on the global 21cm signal in the recent literature.

In chapter 3, we will briefly introduce all of the present and future observational projects aiming to detect the global 21cm signal. From all these experiments, we will thoroughly discuss the results from the EDGES [12] and the Shaped Antenna measurement of background RAdio Spectrum (SARAS) [14] <sup>3</sup>.

In the research half of this thesis (chapters 4 and 5), we place a stronger emphasis on computational aspects. In chapter 4, we examine the importance of estimating the parameters of the global 21cm signal. Furthermore, we briefly describe different methods used to serve this purpose and the advantages of each one. Subsequently, we will bring forth the details of the specific method used in this study. Chapter 5, demonstrates the results of applying this computational method to EDGES observational data.

---

<sup>3</sup>The selection of these two experiments is justified by their explicit emphasis on observing the global 21cm signal rather than spatial signal, coupled with the availability of their released cosmological data.

Finally, in chapter 6, we summarize all the findings of this research and compare them to previous similar studies. Moreover, the future steps of the project are discussed in detail.

## Chapter 2

# The Global 21cm Signal

The 21cm cosmology has been a rapidly evolving field of study since its onset in the early 2000s. Elaboration of this branch of cosmology assists us in forming a better understanding of primordial hydrogen and the physical mechanisms affecting its evolution. On the other hand, besides all the advantages associated with 21cm studies, there is still room for further investigations into the theory.

This chapter is specifically dedicated to the investigation of the **global 21cm signal**. In section 2.1, we initiate the discussion by describing the nature of the 21cm line and how the related interactions give rise to the global curve. Then we briefly portray the computational efforts in this field by introducing two semi-numerical simulations of this radiation (21 Centimeter Fast Approximate Signal Toolbox (21cmFAST) and ARES). As we move along to the last section, we pursue our discussion by stating the latest findings

on the signature of non-standard physics on the 21cm signal. These effects originate from the proposed corresponding theories beyond the standard model of cosmology and particle physics.

## 2.1 Theoretical Basis of the 21cm Signal

After the occurrence of the big bang and recombination, prior to the formation of the first stars and galaxies ( $200 \lesssim z \lesssim 1100$ ), the universe was composed of neutral gas ( $\approx 75\%$  hydrogen, helium, and trace quantities of heavy elements), free electrons, and the residual photons originating from the big bang (CMB) [3, 15]. Since neutral hydrogen is the most abundant component of the IGM before reionization, it provides a convenient tracer for the behavior of baryonic matter in the early universe. Neutral hydrogen has a hyperfine splitting in its 1s ground state caused by the interaction between the magnetic moment of the proton and the electron (Figure 2.1). This spin-flip transition results in the absorption or emission of a photon with the frequency of 1420.4057 MHz [16] corresponding to a wavelength of 21.1cm [3] <sup>1</sup>.

Given that the CMB encompasses photons with the wavelength of 21cm, hydrogen atoms are able to engage in interactions with the CMB. As a consequence of this interaction, the brightness temperature of the 21cm line experiences an alteration <sup>2</sup>. This influence can be

---

<sup>1</sup>The existence of this spectral line was theoretically predicted by van de Hulst in 1942, and Ewen and Purcell reported the first ever detection in 1951 [3].

<sup>2</sup>For the sky averaged 21cm signal, this alteration can go up to 250mK. The interaction of CMB with hydrogen atoms will be discussed thoroughly in the next section as the coupling of the spin temperature  $T_s$



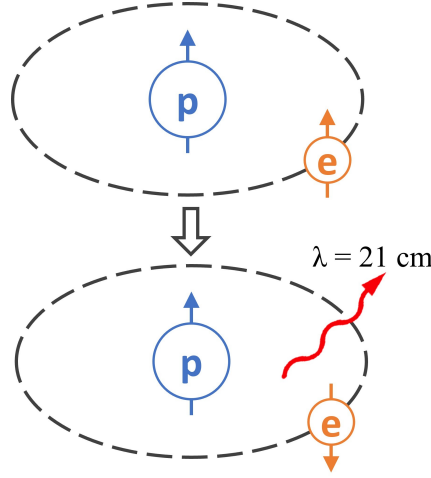


**Figure 2.1:** A basic depiction of the spin-flip transition on the ground energy state of the neutral hydrogen. The upper and lower plots demonstrate the classical cartoons of the triplet and singlet states. The energy difference associated with this transition is  $\Delta E = 5.9 \times 10^{-6} \text{ eV}$  [3]. Figure from Kit Gerodias [17].

detected using radio telescopes over the frequency range of approximately 30 to 200 MHz (due to the redshifting of 21cm photons). [16]. These observations are capable of giving us valuable information about the distribution of neutral hydrogen and the evolution of cosmic structure over time [16].

### 2.1.1 Physical Principles of The 21cm Spectral Line

The 21cm signal is a result of interaction between the CMB and the matter along its way. The characteristics of the signal depend on the radiative transfer along the line of sight. To find the brightness temperature of the 21cm line, we start with the basic Radiative Transfer

---

with the kinetic temperature of the gas  $T_k$ .

Equation (RTE) for the specific intensity  $I_\nu$ :

$$\frac{dI_\nu}{ds} = -\alpha_\nu I_\nu + j_\nu, \quad (2.1)$$

Where  $\alpha_\nu$  and  $j_\nu$  are absorption and emission coefficients, respectively. This equation is written under the assumption of zero scattering [3, 16].

We relate the  $I_\nu$  to temperature by the assumption of working in Rayleigh-Jeans limit, which gives:  $I_\nu = 2k_B T \nu^2 / c^2$ . Moreover, the optical depth along the line of sight is defined as  $\int \alpha_\nu(s) ds$ , where  $ds$  is a path length. Now, we may rewrite equation 2.1 to find the observed brightness temperature  $T_b^{obs}$  at a frequency  $\nu$  along the line of sight from a background radio source of brightness temperature  $T_R$ . This radiation passes through a cloud with the optical depth  $\tau_\nu$ , and uniform excitation temperature  $T_{ex}$  [3, 16]:

$$T_b^{obs} = T_{ex} (1 - e^{-\tau_\nu}) + T_R(\nu) e^{-\tau_\nu} \quad (2.2)$$

For 21cm applications, the excitation temperature is referred to as spin temperature  $T_S$ . It is defined based on the population (number densities) of hydrogen atoms in the triplet ( $n_0$ )

and singlet state ( $n_1$ ) [3, 16]<sup>3</sup>.

$$\frac{n_1}{n_0} = \frac{g_1}{g_0} e^{-\frac{T_*}{T_S}} \quad (2.3)$$

$$g_0 = 1, g_1 = 3 \quad (2.4)$$

$$T_* \equiv \frac{E_{10}}{k_B} = \frac{hc}{k_B \lambda_{21cm}} = 0.068\text{K} \quad (2.5)$$

$g_0$  and  $g_1$  are the statistical degeneracy factors. The deviation of the spin temperature from the background temperature is the key to the detectability of the 21cm signal.

To further investigate the evolution of spin temperature according to equation 2.2, it is required to study the behavior of the optical depth of a cloud of hydrogen. Given that the optical depth is a function of absorption coefficient  $\alpha_\nu$ , in the presence of absorbing atoms, it would be written as:

$$\tau_\nu = \int ds \sigma_0 \phi(\nu) n_0, \quad (2.6)$$

$$n_0 = \frac{n_H}{4}, \quad (2.7)$$

$$\sigma_0 \equiv \frac{3c^2 A_{10}}{8\pi\nu^2}, \quad (2.8)$$

where  $n_H$  is the hydrogen number density, and the 1/4 factor is the ratio of hydrogen atoms in the hyperfine triplet state to the total number of atoms.  $\phi(\nu)$  is the line profile, which is normalized such that  $\int \phi(\nu) d\nu = 1$ .  $\sigma_0$ , which is the normalization factor of the line profile,

---

<sup>3</sup>Refer to figure 2.1 for the definition of hydrogen hyperfine singlet and triplet state.

represents the 21cm cross-section as a function of the spontaneous decay rate of the spin-flip transition  $A_{10} = 2.85 \times 10^{-15} \text{s}^{-1}$  [3, 16]. The relatively small value of  $A_{10}$  implies the rare occurrence of the transition [17]. To account for the ratio of emitting atoms, the optical depth alters to the following form [3, 16]:

$$\tau_\nu = \int ds \left[ 1 - e^{-\frac{T_\star}{T_S}} \right] \sigma_0 \phi(v) n_0. \quad (2.9)$$

Three competing processes influence the spin temperature: 1) interaction of hydrogen atoms with the radio background (mostly CMB), 2) collisions of hydrogen atom with other particles (a mixture of hydrogen atoms, free electrons, and protons with hydrogen atoms as the leading component), and 3) resonant scattering of Lyman  $\alpha$  ( $\text{Ly}\alpha$ ) photons which is mediated by an intermediate excited state and cause a spin-flip transition. Therefore, the spin temperature will be expressed using the equilibrium between these mechanisms and their corresponding coefficients [3, 16]:

$$T_S^{-1} = \frac{T_\gamma^{-1} + x_\alpha T_\alpha^{-1} + x_c T_K^{-1}}{1 + x_\alpha + x_c}, \quad (2.10)$$

where  $T_\gamma$  is the temperature of the surrounding bath of radio photons ( $T_\gamma = T_{\text{CMB}}$ ).  $T_K$  is the kinetic temperature of gas, and  $T_\alpha$  is the color temperature of the  $\text{Ly}\alpha$  radiation field (at the  $\text{Ly}\alpha$  frequency). There is a strong coupling between the  $T_\alpha$  and  $T_K$  as a result of recoil during the repeated scatterings of  $\text{Ly}\alpha$  photons.  $x_c$  and  $x_\alpha$  are the coupling coefficients due to atomic collisions and scattering of  $\text{Ly}\alpha$  photons, respectively. The spin

temperature becomes strongly coupled to the gas temperature when coupling coefficients become dominant:  $x_c + x_\alpha \gtrsim 1$ . On the other hand, it relaxes to  $T_\gamma$  when the coefficients are relatively small:  $x_c + x_\alpha \ll 1$  [3, 16].

The coupling coefficients  $x_c$  and  $x_\alpha$  are defined as a function of collisional scattering (spin de-excitation) rate  $C_{10}$ , and Ly $\alpha$  scattering rate  $P_{10}$  (or equivalently  $P_\alpha$ ) [16, 18]:

$$x_c \equiv \frac{C_{10}T_*}{A_{10}T_\gamma} \quad (2.11)$$

$$x_\alpha \equiv \frac{P_{10}T_*}{A_{10}T_\gamma} \quad (2.12)$$

### 2.1.2 Wouthuysen-Field Coupling

As previously mentioned, a hydrogen atom in the early universe is able to interact with CMB background through photon exchange. However, with the onset of star formation, the CMB will no longer be the only source of photons for the hydrogen atom to interact with. The newly formed objects (massive stars) are capable of generating ultraviolet (UV) photons and reheating the IGM. This excess heat is responsible for the increased collisions, triggering the ionization and de-excitation of IGM gas. This process generates a new source of photons that are injected into the Ly $\alpha$  frequency band by resonant scattering rather than being redshifted from outside of the line. The existence of this second source of the photons increases the probability of the hydrogen-background interaction, further assisting the spin temperature  $T_S$  in coupling to  $T_K$  [3, 16].

The process of coupling the spin temperature of neutral hydrogen to the Ly $\alpha$  background is called **Wouthuysen–Field (WF) effect** [19]<sup>4</sup>. This process plays a pivotal role in the observability of the global 21cm signal by forcing it to deviate from the temperature of the CMB. The Ly $\alpha$  coupling coefficient, indicating the strength of WF effect, was defined in equation 2.12.

### 2.1.3 Sky-Averaged 21cm Signal

We previously mentioned that the global 21cm signal is the average over the 21cm field. We study the behavior of this signal in comparison to a roughly uniform source of radio background. Thus, we define the differential brightness temperature of the global 21cm signal as the excess brightness temperature (due to emission or absorption) of the global 21cm signal with respect to that of the CMB background. Therefore,

$$\delta T_b = T_S - T_\gamma = T_S - T_{CMB}. \quad (2.13)$$

This differential brightness temperature is found using the following expression [16]:

$$\delta T_b \approx 27 (1 - \bar{x}_i) \left( \frac{\Omega_{b,0} h^2}{0.023} \right) \left( \frac{0.15}{\Omega_{m,0} h^2} \frac{1+z}{10} \right)^{1/2} \left( 1 - \frac{T_\gamma}{T_S} \right), \quad (2.14)$$

---

<sup>4</sup>The WF coupling is named after two physicists who independently described the phenomenon in 1952 and 1958: Robert H. Wouthuysen [20], and George B. Field [21].

where  $x_i$  is the ionization fraction, and  $h$  is the dimensionless Hubble constant.  $\Omega_{b,0}$  and  $\Omega_{m,0}$  are the ratio of the current energy density of baryonic and total matter with respect to the critical energy density of the universe.

To further investigate the evolution of the global 21cm signal through the thermal history of the universe and the involved physical mechanisms, we split the early universe era into different redshift regions<sup>5</sup>:

- $200 \lesssim z \lesssim 1100$  (Dark Ages): The universe is filled with high-density gas and the residual free electrons from the recombination. Compton scattering maintains the thermal coupling of gas to CMB ( $T_K = T_\gamma$ ). Due to high density, the collisional coupling is dominant, forcing the spin temperature to the kinetic temperature of the gas ( $T_S = T_K$ ). Therefore, the differential brightness temperature of the 21cm signal is zero during this redshift regime ( $T_S = T_\gamma$ ) [3].
- $40 \lesssim z \lesssim 200$  (Dark Ages): Baryonic matter experiences thermal decoupling from the CMB, making it possible for the non-relativistic gas to cool adiabatically with the expansion of the universe [3]. The temperature of the gas and CMB both drop as a function of redshift with the rate of  $T \propto (1+z)^2$  and  $T \propto (1+z)$ , respectively. This rate discrepancy leaves the gas cooler than radiation while stopping heat exchange between these two components. Therefore, the gas spin temperature decouples from that of

---

<sup>5</sup>It is crucial to mention that there is still considerable uncertainty in the exact values of the redshift bounds and the sequence of events due to our highly limited knowledge on the characteristics and effects of early sources. This uncertainty is such significant that there might even be an overlap between these discussed regions [3].

the CMB. Since collisional coupling is still dominant, the spin temperature remains coupled to the gas kinetic temperature ( $T_S = T_K$ ). Consequently, the 21cm differential brightness temperature becomes negative (absorption) in this redshift region [3, 15].

- $40 \lesssim z \lesssim 80$ : As the density keeps dropping through the expansion, the influence of collisional couplings becomes less significant, causing the spin temperature to again couple with the CMB temperature ( $T_S \rightarrow T_\gamma$ ). Thus, the 21cm differential brightness temperature goes back to zero again [15]. The first blue regions in the upper panel of figure 2.2 and the corresponding absorption trough in the lower panel depict the above-mentioned process [3, 15].
- $z_\alpha \lesssim z \lesssim z_*$ : As large halos begin to collapse and form first stars and galaxies, they generate X-ray emission. These photons are capable of heating their surrounding gas and elevating the probability of collisions. On the other hand, two mechanisms create Ly $\alpha$  photons: 1) Continuous redshifting of background radiation to the Ly $\alpha$  wavelength (continuum photons), and 2) Collisional ionization and deexcitation of IGM gas (injected photons). As a result, a Ly $\alpha$  background is formed. Due to the high cross-section of Ly $\alpha$  photons and hydrogen atoms, the spin temperature tends to couple to  $T_k$ . Therefore, we will again observe the global 21cm signal in absorption (the second trough in the lower panel of Figure 2.2) [3, 15].
- $z_r \lesssim z \lesssim z_\alpha$  (Reionization): Eventually, the gas is reheated by ionizing X-ray photons



from early sources [3], and the 21cm differential brightness temperature becomes positive. The influence of this reheating mechanism is so strong that the 21cm radiation can be observed in emission in this redshift range (red region in the upper panel of figure 2.2). From this point on in the thermal history of the universe, we do not expect to see any more 21cm radiation from IGM since the majority of the gas will be ionized by emergent stars, galaxies, and accreting black holes. Therefore, the 21cm differential brightness temperature goes to zero (the black region in the upper panel of figure 2.2). However, in the regions with higher recombination rates inside galaxies and dark matter halos, the neutral hydrogen is shielded and preserved. Consequently, the 21cm signature originating from inside the galaxies will continue to be emitted [3, 15].

## 2.2 Simulating the Global 21cm Signal

With the current advancements in radio telescope instrumentation, we have entered a data-driven era in 21cm cosmology, empowering us to constrain the properties of astrophysical sources responsible for generating this signal. Nevertheless, extracting astrophysical insights from the collected data is a complex task that necessitates the fast and efficient generation of theoretical templates spanning over the parameter space [23].

As the first attempts to simulate 21cm signal, fully hydrodynamic simulations of the 3-

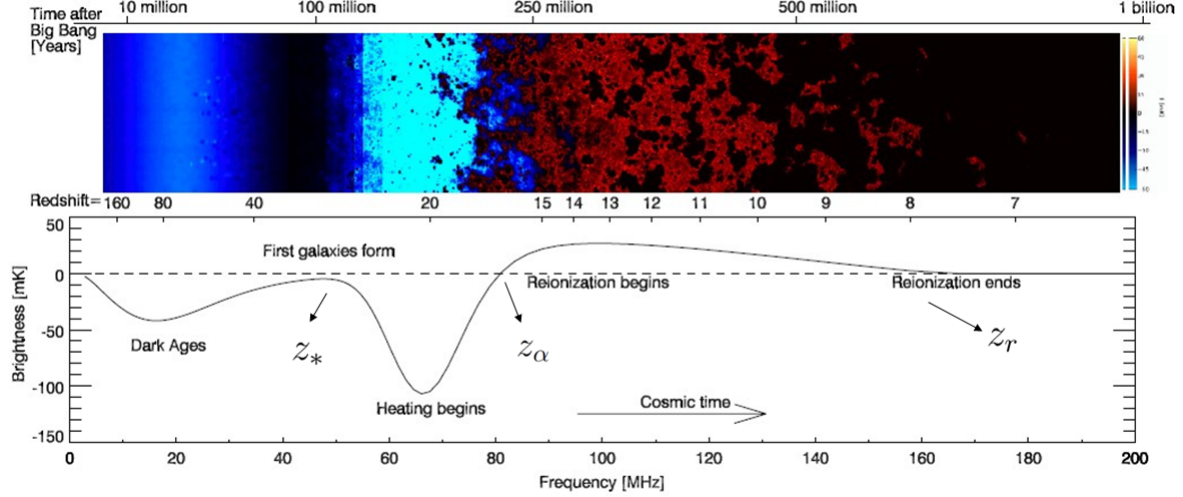


**Figure 2.2:** Time evolution of the global 21cm differential brightness temperature (solid line). The top panel is a color plot demonstrating fluctuations arising from variations in density. The coloration depicts the two absorption phases of 21cm brightness temperature (coupling of  $T_S$  to  $T_K$ , blue regions), emission phase (red regions), and the interval where it disappears completely (coupling of  $T_S$  to  $T_\gamma$ , black region). The lower panel represents the evolution of sky-average (global) 21cm signal from the dark ages to the reionization. The frequency range of the absorption and emission regions exactly matches the corresponding regions in the upper panel. The precise details of the shape of this signal are still unidentified due to our lack of knowledge on the nature of early sources [22]. Figure from Pritchard and Loeb, 2011 [3].

dimensional evolution of the 21cm signal have been adapted [24]. However, these simulations are computationally expensive, and this restriction will considerably decrease our ability to search the parameters space [13]. Semi-analytical methods are the proposed state-of-the-art solutions employing a middle-ground approach between these simulations and fully analytical studies. The results of these semi-analytical calculations are in remarkable agreement with

corresponding hydrodynamic simulations while consuming a significantly lower amount of run-time [25–29].

On top of these simulators, some studies have proposed the use of emulators [23, 30, 31]. These statistical models are trained using the output data of simulators. They emulate the behavior of simulators of global 21cm signal by learning the complex relationships between input parameters and the corresponding output. Emulators create a fast and approximate surrogate model of the simulator, which can be used to predict the outcome for new input parameter values. While emulators allow rapid explorations of parameter space, it should be noted that they are inherently approximations of the underlying physics. Thus, they may not capture all the fine details of the system’s behavior.

In this section, we introduce two powerful tools capable of simulating the theoretical 21cm curves over a wide range of astrophysical and cosmological parameters. The first one is 21cmFAST [2, 32], which is a tool to simulate the spatial 21cm signal. It is also capable of generating the global curve by averaging over all the signals in different directions. The other one is ARES, which calculates the global curve directly by solving the cosmological RTE (equation 2.1) [13]. The main difference between these two comes from the fact that they use different parameterizations of the 21cm theory as the basis of their simulations. For global 21cm applications, the use of ARES is preferred over 21cmFAST based on its direct approach for generating the global 21cm curve.

### 2.2.1 21 Centimeter Fast Approximate Signal Toolbox (21cmFAST)

21cmFAST is a Python-integrated C package designed to produce 3D cosmological realizations of physical fields playing a role in the early universe. It is based on a semi-numerical approach combining the excursion set formalism with perturbation theory. 21cmFAST is capable of simulating the 3D realizations of matter density, peculiar velocity, ionization state, spin temperature field, ionizing flux fields, and 21cm signal [2, 32–34].

As mentioned above, the original simulation was developed as a C code. Later, in 2020, the equivalent Python package was introduced as the third version of 21cmFAST. The core C code is a high-performance script aiming to identify regions of ionized hydrogen in a complex cosmological density field based on excursion set formalism. The evolution of the field is analyzed using first- or second-order Lagrangian perturbation theory. Taking this approach will result in revealing the history of thermal and ionization states of the IGM, alongside X-ray, and UV radiation fields, derived from galaxy models [2].

### 2.2.2 The Accelerated Reionization Era Simulations (ARES)

ARES is a Python package for generating global 21cm curves [13, 35, 36]. Alongside these applications, it can be used as a stand-alone non-equilibrium chemistry solver, global radiation background calculator, galaxy semi-analytic modeling [37–39], PopIII star modeling [40], 1D radiative transfer, and Spectral Energy Distribution (SED)

optimization [41].

ARES draws the globally-averaged 21cm curve through the numerical calculation of RTE (equations 2.1 and 2.2). This approach necessitates the numerical evaluation of optical depth  $\tau_\nu$ , which is a computationally heavy task. A clever solution is to tabulate the optical depth values on an arbitrary number of redshift points in look-up tables. This approach avoids the extensive calculation of this term on each run. However, the accuracy of this method is dependent on the number of chosen redshift points in the look-up table, and undersampling might result in large deviations in background radiation intensity.

Figure 2.3 shows an ARES-generated global 21cm signal as a function of redshift.

## 2.3 Signature of Non-Standard Physics

The physics of the 21cm signal indicates that if the IGM ionization state is close to neutral and the coupling terms are dominant (equation 2.10), the brightness temperature of this line is strongly dependent on the temperature fluctuations of the IGM. Therefore, any physical process involving heat exchange with the IGM is expected to print their signature on the 21cm global signal [3]. Many proposed models of physics beyond the standard model of cosmology and particle physics predict exotic heating of the IGM [3]. Therefore, we dedicate this section to the investigation of these effects. The exact calculation of these fluctuations on the 21cm signal will determine the ability of upcoming observational data to detect these effects.

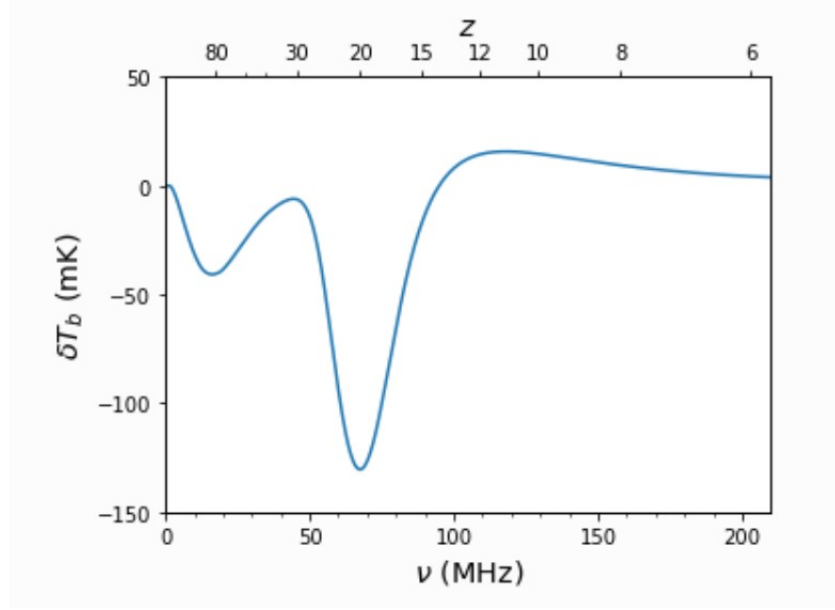


**Figure 2.3:** An example of a global 21cm signal generated using ARES, illustrating the evolution of the brightness temperature of 21cm line against the background radio sources as a function of frequency/redshift. The evolution discussed in section 2.1.3 is perfectly demonstrated in the simulated signal. Note the similarities to corresponding regions in figure 2.2. Figure from Jordan Mirocha in the ARES documentation [35].

Among these beyond standard models, different dark matter candidates play a pivotal role. For example, it is expected that decaying or annihilating dark matter and evaporation of primordial black holes can inject energy into the IGM and lead to a stronger brightness temperature of 21cm signal through the EoR. Therefore, we might be able to constrain these theories by observing their features on the global 21cm signal [42–46] or even rule out some of these candidates [47].

Another significant effect comes from the interactions associated with cosmic strings. The non-linear gravitational influence of cosmic string wakes or the decay of cosmic string

cusps has the ability to alter the brightness temperature of 21cm signal [9, 11, 48].

Moreover, rapidly growing radio-luminous black holes of intermediate mass emit radio signals on their way to becoming supermassive black holes. Thus, they are a type of astrophysical radio source with the ability to enhance the amplitude of the global 21cm signal [10]<sup>6</sup>.

In the remainder of this section, we will focus on two of these distinctive non-standard effects, which attracted the attention of the majority of recent literature related to this area of research.

### 2.3.1 Dark Matter (DM)

The majority of the proposed Dark Matter (DM) candidates encompass physical mechanisms capable of affecting the baryon temperature and the ionization state of the IGM. These features can be employed to reveal the interactions of DM with the visible sector. Formerly, CMB power spectra were used to investigate these signatures. However, the 21cm background can probe energy injection rates approximately above  $10^{-24}\text{eVcm}^{-3}\text{sec}^{-1}$ , which is a much higher sensitivity compared to CMB power spectra<sup>7</sup>.

Decaying or annihilating DM produces a secondary source for high-energy particles which, in fact, can heat and ionize the IGM, contribute to the  $\text{Ly}\alpha$  background, and leave an imprint

---

<sup>6</sup>The author of [10] claims that the effect of rapidly growing radio-luminous black holes is a reasonable explanation for the signal reported by EDGES.

<sup>7</sup>The energy density of the CMB is approximately  $0.26\text{eVcm}^{-3}$ , thus  $10^{-24}\text{eVcm}^{-3}\text{sec}^{-1}$  is equivalent to  $3.85 \times 10^{-24}\text{s}$  of CMB emission.

on the 21cm signal.

Among these various candidates, decaying or annihilating DM may eject energy into the IGM through the interaction of DM particles with known standard model particles. The primordial black hole can also thermally interact with the IGM in the process of Hawking evaporation and the associated radiations. These effects may lead to a stronger brightness temperature of 21cm signal through the EoR. Therefore, we might be able to constrain the characteristics of these theories by their absorption feature in the global 21cm signal (e.g., the lifetime of sterile neutrinos) or even rule out some of the possible candidates (e.g., 3KeV warm DM) [5, 42–47, 49–54].

It must be noted that the presence of additional heating during very high redshifts has the potential to elevate  $T_k$  along a higher adiabatic path during the era of collisional decoupling. As a result, this diminishes the depth of the absorption trough around  $20 \lesssim z \lesssim 30$ . Additionally, if DM annihilations contribute to Ly $\alpha$  pumping and heating, the observed signal would exhibit a smoother progression throughout the absorption epoch. A roughly similar process takes place in other extreme astrophysical models with enhanced production of hard X-rays. This degeneracy is an issue in distinguishing the signature of annihilating DM in the global 21cm signal. However, the spatial distribution of these two heating sources is different, making it possible to differentiate them [4].

Moreover, any particle scenario encompassing an astrophysically relevant suppressed power spectrum leads to a postponement in the process of galaxy formation [55]. Since the



generation of global 21cm signal is dependent on the UV radiation of first stars, the corresponding absorption through will occur later than expected. This consequence is stronger in non-cold DM models, and their absorption signal models are consistently shifted towards smaller redshifts compared to Cold Dark Matter (CDM). Therefore, The amount by which the signal is delayed can be used to test non-cold DM models [56, 57].

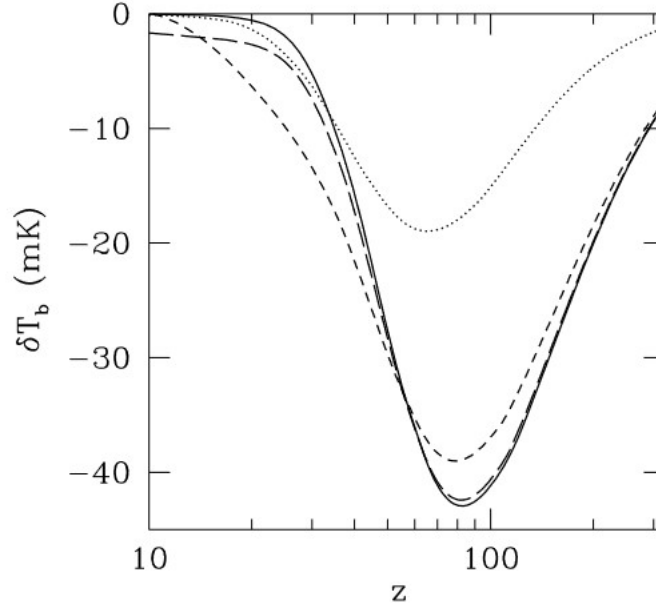


**Figure 2.4:** Effect of different DM models on the global 21cm differential brightness temperature curve. The solid line shows  $\delta T_b$  without decaying/annihilating DM, while the long dashed, short dashed, and dotted lines refer to  $\delta T_b$  with 25keV sterile neutrino decaying Warm Dark Matter (WDM), 10MeV decaying Light Dark Matter (LDM) and 10MeV annihilating LDM, respectively. Figure from [5].

### 2.3.2 Cosmic Strings

Cosmic strings are hypothetical one-dimensional topological defects in space-time that are predicted as the solution of the field equation in many theories beyond the standard model of particle physics. They are thought to be formed during phase transitions in the early universe [58, 59]. It is expected that cosmic strings leave a distinguished signature on the 21cm signal depending on the value of string tension  $G\mu$  [6, 60].

Two key types of cosmic strings are long strings and cosmic string loops. Long strings refer to the straight or curved sections of cosmic strings that extend over cosmic scales. These strings can be indefinitely long, potentially stretching across vast regions of the universe. Long strings are generally stable and do not decay over time. On the other hand, A cosmic string loop is a closed loop configuration of cosmic string that forms when the string self-intersects or undergoes a reconnection event. These loops are typically much smaller than the cosmic strings themselves and can have a variety of sizes. Cosmic string loops are dynamic structures that can oscillate, radiate gravitational waves, and eventually decay through various processes [61].

Long moving strings make wake regions in space-time. The presence of wakes can lead to the formation of overdense regions, to the point that the baryon density becomes twice that of the cosmic gas. Moreover, the column length line profile of 21cm inside the wake region differs from that of the surrounding IGM, which itself results in a stronger coupling of  $T_S$  to  $T_K$  in this region. In other words, the WF coupling is stronger in the presence of cosmic

strings and causes the brightness temperature of the 21cm signal from the wake region to be at least two times more negative compared to the other regions of IGM [11].

The signature is also more evident in lower redshifts since string wake width increases as a function of time [6]. For small string tensions ( $G\mu < 10^{-7}$ ), wake-induced shock heating is not expected. Consequently, the temperature of the gas inside the wake and the IGM are approximately equal [11]. On the other hand, the shock-heated cosmic string scenario yields an even stronger WF coupling (and hence a stronger 21cm brightness temperature with a larger amplitude). By the assumption of a diffuse wake (which influences a relatively large region of space rather than being localized to a single region), it is found that the effect is extended over a wider redshift interval [9, 11, 62]. In order to study the signature of cosmic wakes on the global 21cm signal, which is the sky-averaged 21cm signal, it is required to calculate the contribution of a cosmic string network rather than a single string wake. Therefore, by conducting this evaluation, it was found that the amplitude of the global 21cm signal will be enhanced between 10% to a factor of 2 for string tension in the range of  $10^{-8} \lesssim G\mu \lesssim 10^{-7}$  [11].

Another possibility is to investigate the effect of decay of cosmic string cusps (ordinary string loops [63]) on the global 21cm signal. As calculated by [64], the depth of the absorption through will only be modified by one part in  $10^4$  considering this scenario, which is too weak to constrain the parameter space of the proposed theory.

It is also possible to study the effect of cosmic strings in the cross-correlation of 21cm

radiation and CMB since their existence will simultaneously fluctuate both signals. The cross-correlation observation of these signatures is more reliable compared to individual signals <sup>8</sup> and can be considered evidence of new physics [65].

Within certain string models, strings bear conserved electromagnetic currents, thereby exhibiting superconducting behavior [59]. Some studies have computed the contribution of electromagnetic radiation of annihilating super-conducting cosmic strings to the radio background and derived constraints on the parameter space of superconducting cosmic strings [59, 63, 66]. By including the effects of these strings to the standard theory, the second absorption trough of the global 21cm curve ( $z = 20$ ) corresponds to the trough reported by EDGES for string tension of  $G\mu = 10^{-10}$ . However, the slope on the low redshift end tends to be smoother than that of EDGES data. The corresponding string tension is the same order of magnitude as the upper bound reported by pulsar timing array measurements [67, 68]. The results of this study are shown in figure 2.5.

---

<sup>8</sup>The foreground radiation in CMB observations is milder compared to the intense foreground emissions in 21cm data. Therefore, CMB-21cm observations offer greater reliability in comparison to singular signal studies.

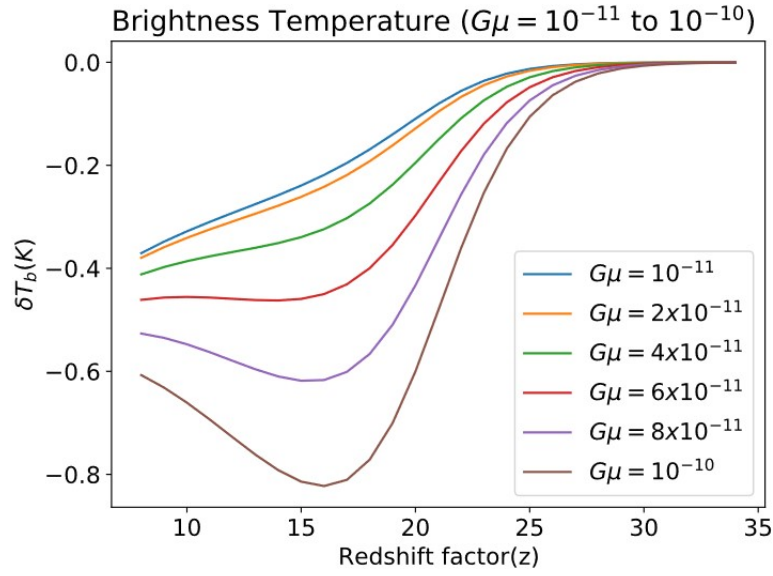


**Figure 2.5:** The differential brightness temperature of 21cm signal as a function of redshift for six different values of superconducting cosmic string tension. The electromagnetic radiation emitted from the decay of superconducting cosmic strings modifies the radio background based on the value of string tension. This alteration of radio background amplifies the absorption features of the global 21cm signal (note the difference of this signal with the corresponding redshift range of Figures 2.2 and 2.3, which do not include the effect of superconducting cosmic strings). For the critical tension value of  $G\mu = 10^{-10}$ , the trough approaches that of EDGES data. Figure from [67].

## Chapter 3

# Observations of the Global 21cm

## Signal

The global 21cm signal acts as an astrophysical probe to study the early universe. However, as promising as the theory sounds, the actual detection is not a straightforward task. In fact, the challenges of this specific observation are significantly more than those of CMB or tomographic 21cm maps. This radiation possesses the ability to partially penetrate into the Earth's atmosphere, making it possible to be detected with ground-based observations. Since this signal is associated with the dark ages in the redshift range of  $30 \lesssim z \lesssim 1100$ , corresponding to the frequency range of  $1.3\text{MHz} \lesssim \nu \lesssim 50\text{MHz}$ , the observations are considered as low-frequency radio experiments [69, 70]. Global 21cm observations do not require high spatial sensitivity; therefore, they can be carried out by

single dipole antennas rather than large interferometric arrays used in measuring spatial 21cm signal [71]<sup>1</sup>.

In this chapter, we first discuss the obstacles to the detection of the global 21cm signal. Then, we introduce a number of experiments specifically designed to observe this emission. Finally, we will revisit the claimed observation by the EDGES group, the corresponding interpretation, and its contrast with SARAS observations [72].

### 3.1 Challenges of Global 21cm Observations

Detection of the global 21cm signal is one of the major challenges of radio cosmology. The complexity of this assignment is a result of the noise sources in low frequencies. Unlike CMB observations which have minor foregrounds in the desired frequency range, the intensity of the global 21cm noise is typically 4 to 5 orders of magnitude stronger than the desired cosmological signal and therefore dominates the data entirely. The mitigation process is also complicated as both the noise contamination and the desired signal are smooth as a function of frequency, making it difficult to use noise subtraction techniques formerly used for spatial maps [22, 70, 71].

To overcome these concerns, the first step is to avoid noise sources. Several precautions in terms of timing and location of observations are taken to ensure the data is being collected

---

<sup>1</sup>There exist some exceptions to this statement, such as Large aperture Experiment to Detect the Dark Ages (LEDA) experiment, which will be discussed in the next section.

with the least possible noise. The remainder of the noise shall be removed by data analysis techniques through the construction of a practical noise model. To ensure accurate noise mitigation, this noise model should closely mimic the characteristics of the noise sources. Three major sources contribute to the noise associated with low-frequency observations in the frequency range favored by global 21cm experiments: astronomical foregrounds (galactic and extra-galactic), ionospheric effects, and human-generated Radio Frequency Interference (RFI) [69, 71, 73]. This section is dedicated to the study of these sources and their associated behaviors.

### 3.1.1 Astronomical Foreground Emission

The main obstacle of global 21cm observations is a consequence of astronomical foreground emission, which is particularly stronger at lower frequencies. The foreground consists of two main types: galactic and extra-galactic. The galactic case comes from the diffuse synchrotron and free-free emission from the Milky Way (such as thermal bremsstrahlung of free electrons). The contribution of synchrotron radiation is approximately two to three orders of magnitude larger than free-free emission<sup>2</sup>. Moreover, the synchrotron emission is generally stronger along the galactic plane of the Milky Way [69, 71, 74, 75]. In the extra-galactic case, the emission is a cause of the Active Galactic Nuclei (AGN), star-forming galaxies, quasars, and other radio-loud sources [73]. Furthermore, the same radiation process described for Milky

---

<sup>2</sup>The exact ratio depends highly on the frequency of interest.



Way applies to other galaxies as well. Overall, the contribution of galactic sources is larger than extra-galactic ones [74, 75].

Several methods have been proposed to remove the astronomical foregrounds from the highly contaminated raw data provided by global 21cm experiments. Mapping of Galactic foregrounds, statistical techniques, including principal component analysis [76], filtering [77], and machine learning algorithms [74, 78–81] appears to be the most promising [69].

### 3.1.2 Ionospheric Effects

The ionosphere is a layer in the Earth’s upper atmosphere ( $50km \lesssim h \lesssim 1000km$ ). When high-energy particles or sunlight (which includes X-ray and UV radiation) pass through the atmosphere, the interaction leaves the gas molecules ionized, resulting in the creation of plasma. The generated ions are capable of reflecting or absorbing radio emissions and therefore interfere with other radio signals passing through this layer. This influence is even more severe in low frequencies, overlapping with the frequency range of the dark ages signal. The ionosphere is the primary origin of systematic aberration, restricting our capacity to investigate the low-frequency domain via radio interferometers [69, 82].

The threshold frequency under which the ionosphere scatters all radio waves and becomes completely opaque is called the *plasma cut-off frequency* [69, 83]. This cut-off is a function of electron density in the ionosphere and generally varies between  $2 - 20MHz$ . The electron density itself depends on the time of day, season, altitude, and solar activity. This effect is

more severe during the summer days and in regions with higher altitudes, forcing the cut-off frequency to higher amounts during these periods. Thus, winter nights in polar locations during the solar minima have a balance of the best accessible features for earth-based low-frequency observations [69]<sup>3</sup>.

Constructing theoretical models for ionospheric effects is the key to the mitigation of this foreground from data collected by Earth-based low-frequency observations, resulting in the extraction of the original cosmological signal [84, 85]. However, the most effective way to avoid contamination of data with ionospheric influences is to observe from outside of Earth [71]. A few such experiments have been proposed, yet none of them has been implemented [86–89].

### 3.1.3 Radio Frequency Interference (RFI)

Terrestrial RFI is another cause of challenge for low-frequency observations, which comes from both human-generated sources and natural ones. The observation frequency band of 21cm observations overlaps with a portion of those employed by television stations, satellite or aircraft communications, and ground-based radio transmitters. Particularly, Frequency Modulation (FM) radio broadcasting band (88 – 108MHz corresponding to  $z \approx 12 - 15$ ) is a crowded frequency region and interferes with the detection of the cosmological signal [90].

Besides human-made RFI, ionized meteor shower trails can reflect radio waves and increase

---

<sup>3</sup>Long winter nights allow ions to have more time to recombine.

the occurrence of RFI. They collide with the Earth’s atmosphere and ionize the molecules [91]. This effect is more evident in remote locations where radio antennas are installed. Moreover, telescopes themselves may self-generate RFI through unshielded electronics [69].

As the first step in the procedure of avoiding and removing the effects of RFI from cosmological data, telescopes are deployed in remote radio-quiet locations (e.g., South African Karoo desert [92], the Western Australian desert [12], and sub-Antarctic Marion Island [91, 93, 94]). Furthermore, major observations are scheduled during low-RFI periods (e.g., nights) [95]. A more productive approach is to position them in locations outside of Earth. Some studies propose radio interferometers to be installed on the far side of the Moon [96, 97] to avoid interference from both the ionosphere and human-made RFI [69].

## 3.2 Global 21cm Experiments

Several experiments are dedicated to the observation of the spatial 21cm signal, but only a few of them are specifically designed to detect the global 21cm signal. As mentioned earlier, this detection is very challenging due to the powerful foregrounds in the desired frequency band of the cosmological signal. The ongoing Global 21 cm experiments are generally composed of wideband antennas connected with a correlation spectrometer. They vary in terms of antenna frequency response and the approach employed for calibration of the systematic instrumental effects [98]. Successful detection of global 21cm signature is dependant on measurements with the accuracy of order  $1 : 10^5$ . Accomplishing this sensitivity requires

smart system engineering and tuned electrical performance [99]. In this section, we will present a brief review of some of the ongoing global 21cm experiments.

### Experiment to Detect the Global EoR Signature (EDGES)

The collaboration between MIT Haystack Observatory and Arizona State University, aiming to detect the global 21cm, is known as EDGES [100, 101]. Located at the Murchison Radio-astronomy Observatory and Mileura Station in Western Australia, the EDGES group has developed four versions of the instruments in the past decade. Each radiometer is basically a single compact dipole-like antenna alongside a well-calibrated radio receiver. The measurement calibration of the instrument has proven to possess the levels of accuracy needed for 21cm observations [102, 103]. The early results of this experiment ruled out models of rapid reionization as well as models of early star formation, especially those with little or late X-ray heating [104, 105]. In 2018, the EDGES team reported the first-ever claim of the detection of the global 21cm signal [12]. They found an absorption profile in the global radio spectrum centered at a frequency of 78MHz ( $z \approx 17$ ) with an amplitude of 500mK. The depth of the observed trough is more than a factor of two greater than the largest standard theoretical predictions. Moreover, the overall behavior (shape) of the signal is significantly different from the expectation of the Lambda Cold Dark Matter ( $\Lambda$ CDM) model. Currently, the 21cm community endeavors to build new radiometers to confirm the EDGES detection or attempt to explain the reported signal

through the utilization of non-standard scenarios [71, 106, 107].

### Shaped Antenna measurement of background RAdio Spectrum (SARAS)

Initially sited at the Raman Research Institute in India, SARAS is another experiment with the goal of detecting global spectral distortions from redshifted 21cm signal during Cosmic Dawn and Reionization. The radiometer utilized a fat-dipole antenna with a frequency-independent beam [14]. Motivated by the advantages of monopole antennas over dipoles in terms of frequency independence, the modified SARAS2 version was a shaped monopole antenna deployed at the radio-quiet Timbaktu Collective in Southern India [108]. SARAS2 eventually provided more promising results compared to the original SARAS1 experiment. The collected data targeting the 110 – 200MHz frequency band were examined for signatures of cosmological reionization, and soon they rejected the class of cosmological models offering rapid reionization or inefficient primordial gas heating (very cold IGM at the epoch of the Cosmic Dawn, resulting in deep 21cm absorption troughs) [109, 110]. These findings were inconsistent with the EDGES claimed detection<sup>4</sup> [71, 72, 106].

The design was later progressed in terms of calibration techniques to eliminate errors in the receiver system and avoid unwanted structures from intense foregrounds. The efforts paved the way for the SARAS3 experiment that is optimized for the 50 – 100MHz band [106, 111]. Later, in 2022, findings of SARAS3 experiment revealed the non-detection of signal reported by EDGES [112].

---

<sup>4</sup>This inconsistency will be discussed thoroughly in section 3.3.

### Probing Radio Intensity at high-Z from Marion (PRI<sup>Z</sup>M)

Probing Radio Intensity at high-Z from Marion (PRI<sup>Z</sup>M) is a recent effort to study the cosmic dawn and dark ages. This experiment is specially designed to collect global 21cm data in the frequency range of 50 – 150MHz. The distinguishing feature of this experiment is its exceptionally isolated and radio-quiet location on an island in the sub-Antarctic Southern Indian Ocean called *Marion*. This island is approximately 2000km away from the nearest continental land masses and any human-inhabited regions. With no detected RFI contamination in the FM band, Marion is one of the prime locations on Earth for radio observations. The experiment consists of two modified four-square radiometers, operating at center frequencies of 70 and 100 MHz, and a dual-polarization spectrometer back end. The antenna was originally designed for Small Radio Telescope for Cosmic Hydrogen Intensity Mapping (SCI-HI) experiment [90, 113] and later modified for PRI<sup>Z</sup>M. After its deployment in Marion in 2017, PRI<sup>Z</sup>M started its science observations. Currently, the collected raw data is being analyzed to extract the cosmological sky-averaged 21cm signal [91, 93].

### Radio Experiment for the Analysis of Cosmic Hydrogen (REACH)

The Radio Experiment for the Analysis of Cosmic Hydrogen (REACH) experiment is another wideband global 21cm project led by Cambridge University, covering both the cosmic dawn and the epoch of reionization. The antenna is designed as a seven-pointed blade (hexagonal

dipole) with conical log spirals, covering the frequency range of  $50 - 135\text{MHz}$  ( $7.5 < z < 28$ ). In the future, multiple antennas (scaled and/or different types) will be added to form a joint confident detection. REACH phase I was deployed in the RFI-quiet Karoo radio astronomy reserve in South Africa in 2022 [92, 114, 115].

### **Mapper of the IGM Spin Temperature (MIST)**

The Mapper of the IGM Spin Temperature (MIST) experiment plans to perform measurements of the global radio spectrum within the frequency range of  $25 - 105\text{MHz}$ . The deployment took place in different remote locations, such as Axel Heiberg Island in Canadian Arctic. This radiometer uses a blade dipole with two panels. The first two antennas of this project are currently gathering data, and the third is undergoing the construction procedure [116–118].

### **Large aperture Experiment to Detect the Dark Ages (LEDA)**

Driven by the constraint of single-antenna experiments of the global 21cm signal, LEDA collaboration constructed a single-layer multi-antenna instrument (array of simple dipole antennas) to observe the early universe in  $30 - 85\text{MHz}$  band ( $16 < z < 34$ ). This unique 512-input 100MHz correlator is installed in two locations: Long Wavelength Array (LWA) stations at Owen’s Valley Radio Observatory (OVRO) (OVRO-LWA) and the National Radio Astronomy Observatory in Socorro, New Mexico (LWA1). The OVRO-LWA site consists of

251 stands within a  $100m$  radius, which is approximately two times the radius of LWA1. The two stations share the same antenna design and analogue systems, but the digital system is distinct<sup>5</sup>. The integrated LEDA correlator achieved its first light in August 2013 and has been performing science observations ever since [95, 119–122].

### Hydrogen Probe of the Epoch of REIONization (HYPERION)

The Hydrogen Probe of the Epoch of REIONization (HYPERION) project is another global 21cm experiment that was initially deployed at OVRO. It is composed of a single-element radio telescope system with a two-channel interferometric/cross-correlation spectrometer. The system architecture consists of an electrically short fat dipole with a frequency-independent antenna beam between  $30 - 120\text{MHz}$ . The design was directly inspired by the SARAS experiment, albeit tailored specifically for lower frequencies through scaling. [98, 99, 123].

### Broadband Instrument for Global HydrOgen ReioNisation Signal (BIGHORNS)

The Broadband Instrument for Global HydrOgen ReioNisation Signal (BIGHORNS) is a portable total power radiometer that can be deployed in any remote location without access to electricity. The experiment targets the frequency range of  $\approx 50\text{-}200\text{MHz}$ . The first deployments took place at a few radio-quiet locations in Western Australia (Wondinong Station in April 2014, followed by other deployments in Muresk and Perth). The initial

---

<sup>5</sup>OVRO-LWA uses a digital system specially designed for wide-bandwidth cross-correlation.



antenna design was based on an off-the-shelf biconical antenna, which was later replaced with a bespoke conical log spiral antenna [124].

### 3.3 On The Interpretation of EDGES Data

In 2018, the EDGES collaboration presented the measurements of an anomalously large and abrupt absorption signal in the radio spectrum, which was in apparent contradiction to the theoretical expectations [12]. The amplitude of the signal is more than a factor of two greater than the corresponding expected signal from  $\Lambda$ CDM model. Moreover, the shape of the curve does not comply with the smooth transition in the theoretical signal. Figure 3.1 demonstrates the claimed detection, and its comparison with the ARES simulated global 21cm curve generated using the default values of ARES for cosmological and astrophysical parameters [35].

This observed large amplitude can only be the outcome of two scenarios: 1. The gas kinetic temperature is lower than theoretical expectations, 2. There exists some excess radio emission in the background, implying that the temperature of the radio background is hotter than expected in the frequency range corresponding to dark ages and reionization.

The standard cooling mechanism influencing different components of the universe is a result of adiabatic expansion. However, for the gas to be this cold at this redshift, extra cooling mechanisms shall be present at the cosmic dawn to derive the spin temperature to such a low value. Following this idea, many authors have proposed physical mechanisms

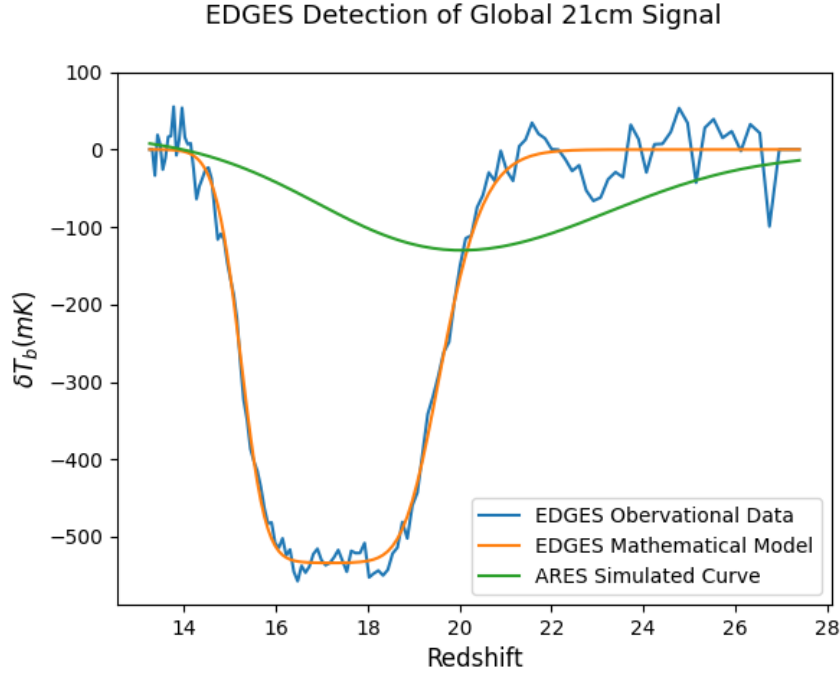


**Figure 3.1:** Detection of global 21cm signal reported by the EDGES collaboration. The blue curve illustrates the observational data, and the orange curve is the mathematical model (flattened Gaussian) which EDGES group used for the purpose of fitting their data. There is no direct connection between this model and the underlying physics of the global 21cm signal. This model is only chosen based on the similarity of its shape to that of the experimental signal. The green curve is an ARES simulation in the exact redshift range of EDGES data. It is generated using the default values of ARES for cosmological and astrophysical parameters [35]. Note the significant discrepancy in the amplitude and shape of the observational and theoretical curves. Figure generated using data from [12].

beyond the standard model of particles and astrophysics to achieve a cooler IGM. DM-baryon interactions can be considered as a source of extra cooling through the transmission of thermal energy from baryonic particles of gas to DM particles [125–130] (refer to 2.3 for a detailed discussion on the influences of various non-standard scenarios on the global 21cm

signal).

Regarding the background radio emission, it is often assumed that the background radio bath is mainly composed of CMB, and subsequent calculations are built upon this approximation. However, the EDGES signal gave rise to the idea that there might be excess radio emission in the cosmic Dawn that increases the spin temperature [131]. Recent studies revealed that the diffuse radio background from astrophysical origins is unable to explain the discrepancy [71, 131].

Apart from the inexplicable amplitude, the shape of the reported signal is also a source of concern, as the width of the trough is evidently different from the theoretical expectation. In fact, only astrophysical models based on strong heating of the IGM are able to justify the width, which is opposite to what is required to obtain large amplitudes. Thus, within the framework of the current formulation of 21cm cosmology, the EDGES reported signal includes inner inconsistency [71, 132].

On top of all these discussions, findings of SARAS2 experiment performed in the same redshift range as ARES have disfavored models offering a cold IGM, which is clearly in tension with EDGES results [109, 110]. Moreover, the modified version of the experiment, SARAS3, has reported the absence of the aforesaid absorption trough in their investigations. From their point of view, considering the potential sources of systematic errors and instrumental artifacts that could have influenced the observed signal, it is unlikely that the reported trough is a signature of an astrophysical phenomenon [72, 112].

## Chapter 4

# Parameter Estimation Methods

We formerly discussed the physics of global 21cm signal and associated observational attempts. We also pointed out the capacity of the global 21cm signal to constrain the cosmological and astrophysical parameters and demonstrate the signatures of theories beyond the standard model. However, the details of the process to extract this piece of information from the existing and upcoming observational data are yet to be addressed.

The majority of proposed non-standard mechanisms are expected to leave their footprints on the value of physical parameters. Therefore, the need to perform proper parameter estimation on the corresponding observational data is undeniable. Based on this knowledge, we dedicate this chapter to the construction of a firm computational framework specifically designed for the global 21cm parameter estimation.

Previous studies have examined various computational algorithms to accomplish this task.

The efforts include MCMC [133, 134], Artificial Neural Networks (ANN) [135], and Fisher Matrix approaches [136]. Sampling algorithms such as MCMC are capable of exploring the entire likelihood surface. On the other hand, neural networks are typically employed for problems where comprehensive mapping of the entire likelihood surface becomes excessively complex. For global 21cm applications, the entire likelihood surface is accessible; thus, the use of MCMC method is preferred.

We proceed by introducing the main parameter estimation algorithm used in our study, which is a combination of LM and MCMC. We explain the reason behind utilizing both of these algorithms for this particular fitting challenge and provide a detailed explanation of the procedure to combine them. We also discuss two different tests used to measure the quality of the proposed fit. In chapter 5, we present the results of applying this fitting method to the observed global 21cm signal (EDGES) and its corresponding theoretical model generated by ARES<sup>1</sup>.

## 4.1 Levenberg-Marquardt (LM)

The LM, also known as the Damped Least-Squares (DLS) method, is a fitting algorithm used for non-linear least-squares problems. This iterative algorithm is based on another root-finding method referred to as "Newton's method". LM is capable of fitting models

---

<sup>1</sup>Python Implementation of the analysis of this thesis is publicly available on GitHub under the dedicated repository: [https://github.com/aryana-haghjoo/My-Project/tree/main/code\\_final](https://github.com/aryana-haghjoo/My-Project/tree/main/code_final)

with Gaussian-shaped likelihood spaces. However, its abilities are limited when it comes to determining error bars.

In this chapter, we derive the basic analytical definition of this method. We start by defining the matrix form of chi-square. Subsequently, we calculate the second-order derivative of chi-square with respect to the parameters of the model. We will show that this calculation leads to defining the covariance matrix, which forms the basis to generate correlated noise for the MCMC algorithm (refer to 4.3.1).

#### 4.1.1 Covariance Matrix

A traditional fitting problem is generally defined as trying to find the parameters in a theoretical model which can best explain a set of data and its associated noise. A possible measure for the quality of fit is the value of likelihood. With the assumption of Gaussian noise, the procedure to maximize the likelihood in the presence of noise leads to the minimization of an expression called the "chi-square". The linear algebra notation of the chi-square is

$$\chi^2 \equiv [d - A(m)]^T N^{-1} [d - A(m)], \quad (4.1)$$

Where  $d$  is the array containing the data points and  $A$  is the model which is dependent on the parameter set  $m$  (the dependency can be nonlinear). Thus,  $A(m)$  is the representation

of the expected value of the data with respect to the theoretical model.  $N$  is also defined as the noise matrix, which in general, is non-diagonal. In the case of a diagonal noise matrix, expression 4.1 takes the form of:

$$\chi^2 = \sum \frac{(x_i - \mu_i)^2}{\sigma_i^2}, \quad (4.2)$$

Where  $x_i$  is the observed data,  $\mu_i$  is the expected value ( $\mu_i = \langle d_i \rangle = A_i(m)$ ), and  $\sigma$  is the error associated with each data point ( $N_{i,i} = \sigma_i^2$ ). We continue by calculating the first two derivatives of the above expression, leading to the construction of the gradient descent method.

$$\frac{d\chi^2}{dm} = - \left( \frac{dA(m)}{dm} \right)^T N^{-1} (d - A(m)) - (d - A(m))^T N^{-1} \left( \frac{dA(m)}{dm} \right) \quad (4.3)$$

We define  $A' \equiv \frac{dA(m)}{dm}$ , and  $r \equiv d - A(m)$ . Thus, the above expression takes the form:

$$\frac{d\chi^2}{dm} = - (A')^T N^{-1} r - r^T N^{-1} A'. \quad (4.4)$$

Since we know that

$$(N^{-1})^T = N^{-1} \quad (4.5)$$

$$[A' N^{-1} r]^T = r^T N^{-1} (A')^T, \quad (4.6)$$

substituting in 4.4, we get

$$\frac{d\chi^2}{dm} = -2 (A')^T N^{-1} r. \quad (4.7)$$

Thus, we can calculate the second derivative:

$$\frac{d^2\chi^2}{dm^2} = -2 \left( \frac{dA'}{dm} \right)^T N^{-1} r - 2 (A')^T N^{-1} (-A'). \quad (4.8)$$

Neglecting the initial term is generally considered safe, as the  $r$  component, which represents the difference between the model and data, can have positive or negative values. Consequently, its average approaches zero. Furthermore, our primary objective is to achieve a zero chi-square gradient. Hence, it is acceptable if the curvature is slightly deviated as long as we attain the maximum likelihood. It is worth noting that the purpose of using LM is solely to generate a covariance matrix for our MCMC. Thus, the generated covariance matrix does not need to be flawless.

Finally, using the above-mentioned logic, we are left with:

$$\frac{d^2\chi^2}{dm^2} = 2 (A')^T N^{-1} A', \quad (4.9)$$

which is the definition of the curvature matrix. Our primary focus lies not on this matrix itself but rather on its inverse. The inverse is called the **Covariance Matrix**. The diagonal



elements of this matrix are simply the variance of each parameter ( $\sigma_{i,i}$ ), while the off-diagonal elements represent the covariance, measuring the dependency of a pair of parameters ( $\sigma_{i,j}$ ).

In general, we expect the covariance matrix to be semi-positive definite<sup>2</sup>.

### 4.1.2 Derivation of the Levenberg-Marquardt Algorithm

In the LM method, on each iteration, the set of parameters  $m$  is replaced with  $m + \delta m$ . To find the  $\delta m$ , the function  $\chi^2(m + \delta m)$  is approximated by its linearization:

$$\chi^2(m) = r^T N^{-1} r \quad (4.10)$$

$$\chi^2(m + \delta m) = \chi^2(m) + \left( \frac{d\chi^2}{dm} \right) \delta m \quad (4.11)$$

Similar to the procedure done in section 4.1, we calculate the derivative of equation 4.11:

$$\frac{d\chi^2(m + \delta m)}{dm} = \frac{d}{dm} (\chi^2) + \frac{d}{dm} \left( \frac{d\chi^2}{dm} \delta m \right) \quad (4.12)$$

We already derived the expression for the first order derivative of chi-square in equation 4.4.

Therefore:

$$\frac{d\chi^2(m + \delta m)}{dm} = -2 (A')^T N^{-1} r + \left( \frac{d^2\chi^2}{dm^2} \right) \delta m + \frac{d\chi^2}{dm} \left( \frac{d}{dm} (\delta m) \right), \quad (4.13)$$

---

<sup>2</sup>A positive definite matrix only possesses positive eigenvalues. However, for a semi-positive definitive matrix, eigenvalues are non-negative.

where the last term equals zero since  $\delta m$  does not have any fundamental dependencies on  $m$ . Regarding the second term, we have already found the expression for the second derivative of chi-square in 4.9. Thus, we are left with:

$$\frac{d\chi^2(m + \delta m)}{dm} = -2 (A')^T N^{-1} r + 2 (A')^T N^{-1} A' \delta m \quad (4.14)$$

Setting  $\frac{d\chi^2(m + \delta m)}{dm} = 0$ , we get:

$$A'^T N^{-1} A' \delta m = A'^T N^{-1} r \quad (4.15)$$

$$\delta m = \left( A'^T N^{-1} A' \right)^{-1} A'^T N^{-1} r \quad (4.16)$$

Equation 4.16 represents the basis for **Newton's method**. Unfortunately, this method suffers from convergence issues, especially on complicated likelihood surfaces. To overcome this obstacle, the algorithm is modified by adding a new term to the left-hand side of equation 4.16. This term includes a control parameter  $\Lambda$  that is updated on each iteration depending on the quality of fit.

$$\left( A'^T N^{-1} A' + \Lambda I \right) \delta m = A'^T N^{-1} r \quad (4.17)$$

$$\delta m = \left( A'^T N^{-1} A' + \Lambda I \right)^{-1} A'^T N^{-1} r \quad (4.18)$$

Now the basic idea is apparent: On each iteration, a set of parameters  $m$  will be replaced by  $m + \delta m$ , and the chi-square is calculated based on the perturbed parameters. Subsequently, the new chi-square is compared to its value in the last step. If we encounter a higher value, the  $\Lambda$  will be multiplied to a constant arbitrary number ( $> 1$ ). Otherwise, it will be divided with another constant value ( $> 1$ ). For practical purposes, if  $\Lambda$  takes a value lower than a constant small arbitrary number, we set it equal to zero. If the  $\Lambda$  is zero, and the chi-square is less than an arbitrary threshold value, we declare the **convergence** of the algorithm.

A flow chart depiction of this method is shown in Figure 4.1.

## 4.2 Markov Chain Monte Carlo (MCMC)

Given that LM is not always effective in finding the best-fit point for complex likelihood spaces, a more powerful algorithm such as MCMC is necessary in many real-life applications. MCMC is particularly effective in fitting non-Gaussian likelihood spaces and has a guaranteed convergence, regardless of the starting point in parameter space. However, the algorithm is computationally heavy due to its iterative nature, which is based on the evaluation of the chi-square on each step. Initially, an arbitrary point in parameter space is given to MCMC as its initial trial step, and the associated chi-square is calculated. Then, a random point is drawn from a Gaussian distribution, where the mean is set at the last point in the chain<sup>3</sup>. Subsequently, the new chi-square is compared to the previous one from the last trial step.

---

<sup>3</sup>In Python applications, the `numpy.randn` function is used to serve this purpose.

If the new chi-square is lower, the new trial point is accepted into the chain. If the new chi-square is higher, the trial point is accepted with a probability determined by a specific criterion. This criterion is defined based on Gaussian insights:

$$Probability = e^{\frac{-1}{2}(\chi_{new}^2 - \chi^2)} \quad (4.19)$$

As a measure of MCMC convergence speed, the "acceptance ratio" is used to determine the fraction of trial steps that end up getting accepted into the chain. It should be noted that the convergence of the MCMC is not dependent on the value of the acceptance ratio, but it influences the number of trial steps before the algorithm reaches its convergence. A low acceptance ratio will result in the need for more trial steps, therefore, a longer period of run-time.

A visual summary of MCMC algorithm is illustrated in Figure 4.2.

#### 4.2.1 Convergence Test

The MCMC algorithm requires to explore different regions of the parameter space in order to reach convergence. Various methods have been developed to ensure the convergence of this approach, one of which involves the investigation of the behavior of the power spectrum. The power spectrum represents the distribution of power at different frequencies in the MCMC chain. In the case of a fully-converged MCMC chain, the power spectrum must demonstrate

the behavior of white noise, with power uniformly distributed among all frequencies. On the other hand, the power spectrum of an unconverged chain shows ascending power for lower frequencies. Therefore, the criterion for ensuring the convergence of an MCMC is the flatness of the chain power spectrum in low frequencies when plotted on a log-log scale. Figure 4.3 and 4.4 illustrate the difference between a converged and an unconverged chain.

### 4.3 Combination of MCMC and LM

MCMC is a computationally heavy algorithm due to its iterative nature. If the chi-square calculation process on each step is also a time-consuming task, the MCMC will experience a rather long run-time before reaching the converged state. One of the proposed methods to deal with this issue and help the MCMC to converge faster is to use the insights provided by the outputs of LM. It is worth mentioning again that our sole rationale to use LM in our application is to generate a covariance matrix for the MCMC.

We previously discussed that the parameters of a model might be correlated with each other, and the strength of this correlation is dictated by the elements of the covariance matrix. During a basic MCMC fitting process, we draw random samples from independent one-dimensional Gaussian distributions constructed for each of the parameters. These samples do not take the possible correlations of parameters into account. On the other hand, a modified MCMC, which is combined with LM, generates samples using a multivariate Gaussian distribution (joint normal distribution) and has the capacity to

encompass such characteristics. This method will pave the way to increasing the probability of these samples getting accepted into the final chain. Eventually, we are able to summarize that this approach (feeding the MCMC with a posterior distribution) will assist the MCMC to explore more efficient regions of parameter space and converge faster. Figure 4.5 portrays this technique briefly.

The correlation between distinctive pairs of parameters can be visually assessed using *corner plots*. A corner plot displays the pairwise scatter plots of all the parameters in the chain and it is particularly useful when dealing with high-dimensional parameter spaces. These plots provide insights to identify possible mutual dependencies. If there is a strong correlation between two parameters, it may indicate a degeneracy or a trade-off between those parameters in the model. Figure 4.6, which shows the corner plots for a four-variable Gaussian model, emphasizes the importance of sampling from a multivariate normal distribution and taking the correlations between the parameters into account.

By utilizing the covariance matrix provided by the LM algorithm, we possess the ability to generate an arbitrary number of correlated noise samples easily. The covariance matrix must be calculated at the point of "best fit" found by the LM. This procedure is described thoroughly in the following section.

### 4.3.1 Generating Correlated Noise

Correlated noise, as opposed to white noise, refers to a type of noise or random variation in a set of samples that exhibits a correlation or relationship with another variable. In other words, it is a noise that is not completely random but instead has some level of dependency on other parameters. The mathematical tool to quantify these correlations is the covariance matrix, which is often used to characterize the statistical properties of the noise.

The off-diagonal elements of a covariance matrix correspond to the covariance between each pair of parameters. Thus, by drawing samples from the covariance matrix, we are genuinely sampling from the multivariate normal distribution with the deviation values describing the uncertainties in the parameters. Two equivalent approaches can be used to generate correlated noise: Cholesky and eigenvalue decomposition of the covariance matrix. For practical reasons, we prefer to use the eigenvalue decomposition for our applications<sup>4</sup>. The procedure is as follows: A matrix of random variables drawn from a one-dimensional Gaussian is constructed in the desired shape ( $n \times m$ , corresponding to the number of samples and the number of parameters, respectively). Then, this matrix is multiplied by the eigenvalue matrix and scaled by the square root of the eigenvalues. The transposition of the product will provide the desired correlated samples.

To gain more precision, it is possible to use the eigenvalues decomposition of the normalized covariance matrix (where diagonal samples all equal unity). The normalization

---

<sup>4</sup>Normally, calculating the Cholesky decomposition takes a shorter amount of time.

process is done by multiplying the covariance matrix with its own diagonal. Eventually, the drawn samples are denormalized by scaling them with the square root of the diagonal matrix.

## 4.4 Algorithm Validation

To ensure the accuracy and reliability of the results produced with the described algorithm, we present two distinctive validation tests. The criterion will also assess the performance of the algorithm and the overall quality of the model fitting.

### 4.4.1 The Chi-Square Consistency Test

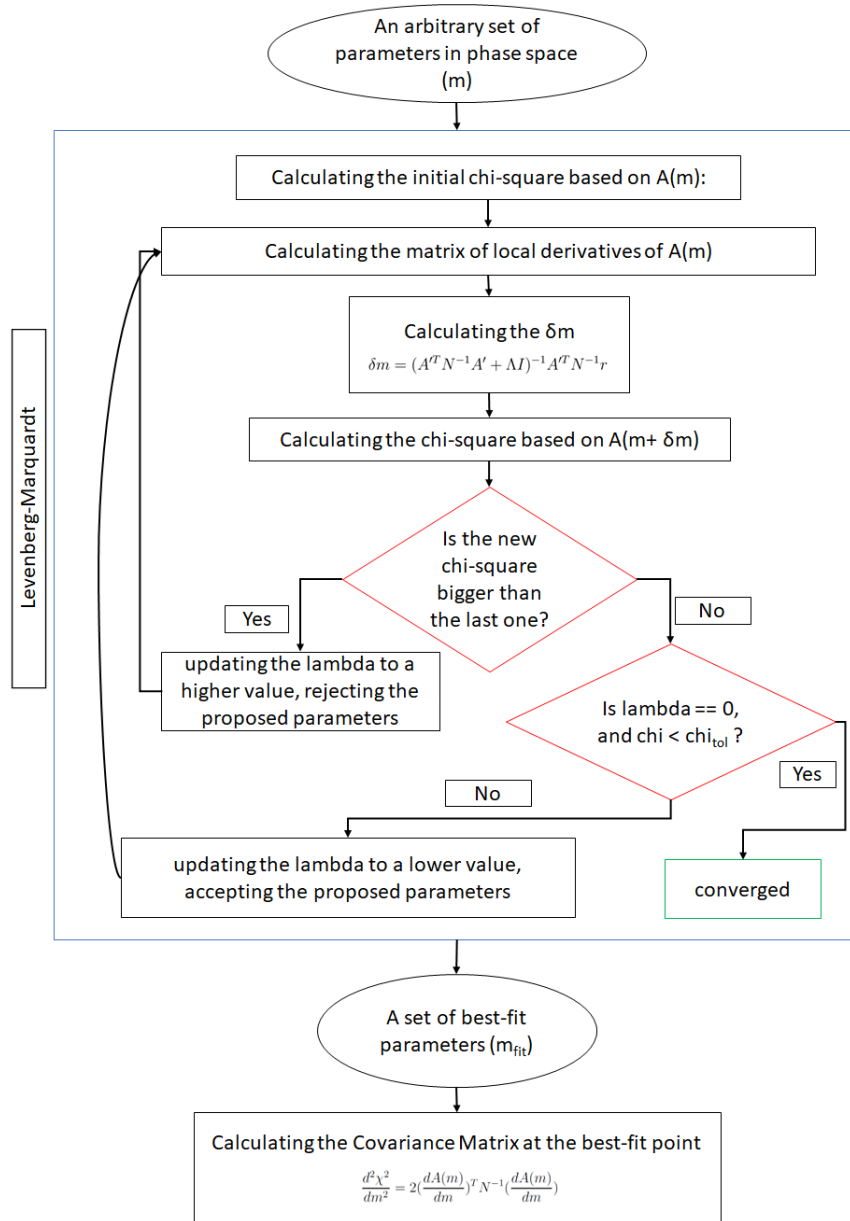
The primary focus of this approach lies in examining the results obtained from the LM and the associated drawn samples. Numerous samples are drawn from the covariance matrix, and their corresponding chi-square is computed. Given that the covariance matrix holds the information on parameter uncertainties, it is anticipated that, on average, the disparity in chi-square statistics between two distinct samples should be roughly equivalent to one unit per each parameter of the model. This expectation arises from the fact that the chi-square statistic scales according to the uncertainties inherent in both the data and model, which have magnitudes around one.

Figure 4.7 shows an example of the distribution of disparity between the chi-square values.



#### 4.4.2 The Chi-Square Parameter Correlation Test

An alternative approach for result verification involves creating plots that depict the relationship between the chi-square values of drawn samples and individual parameters. With reference to the defined chi-square equation (see Equation 4.1), which captures the non-linear dependence of chi-square on model parameters, it is anticipated that a parabolic trend will be observed. Figure 4.8 illustrates plots of chi-square values against parameters for the identical mathematical model as presented in Figure 4.7.



**Figure 4.1:** Flow chart depicting the Levenberg-Marquardt algorithm. The algorithm starts with the calculation of the  $\chi^2$  based on the theoretical model predicted by the initial set of parameters. Then, the new  $\delta m$  is found using 4.18, and its associated  $\chi^2$  is calculated. The new  $\chi^2$  is compared to its value from the last iteration, and the value of the  $\Lambda$  is determined by the success or failure of the current iteration. The algorithm is considered as converged if  $\Lambda = 0$ , and the  $\chi^2$  decreases less than a threshold amount.

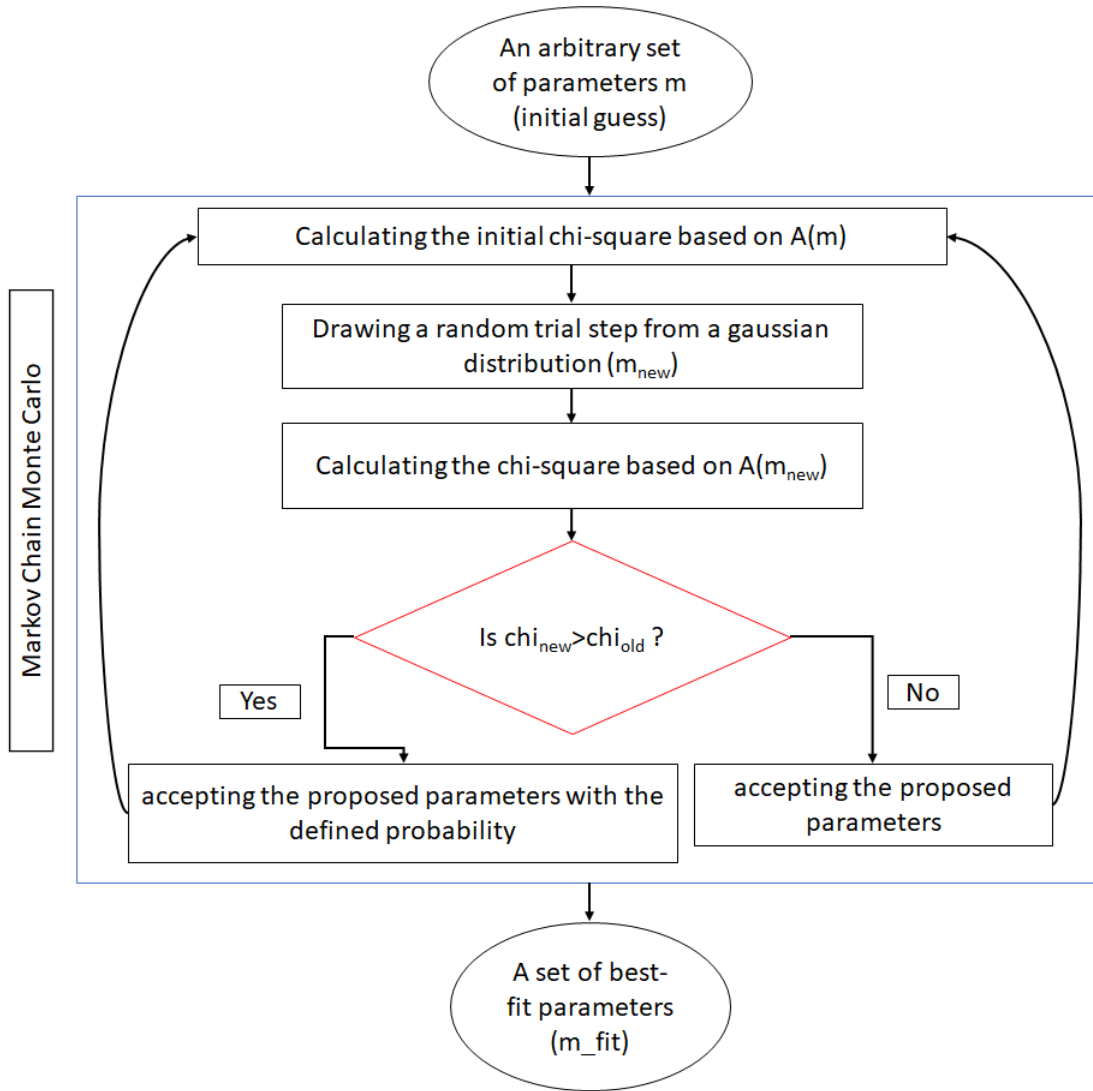


**Figure 4.2:** Flow chart depicting the MCMC algorithm. The algorithm starts with the calculation of the  $\chi^2$  based on the theoretical model predicted by the initial set of parameters. Then, a new set of parameters are drawn from independent one-dimensional Gaussian distributions, and the associated  $\chi^2$  is calculated. The new  $\chi^2$  is compared to its value from the last iteration. If  $\chi^2$  has lowered, the new combination of parameters is accepted into the chain. Otherwise, the parameters will be accepted by the probability defined in 4.19. The algorithm itself does not contain control mechanisms to test its own convergence. Therefore, other approaches, such as power spectrum investigation, are employed (refer to section 4.2.1 and Figures 4.4 and 4.3).

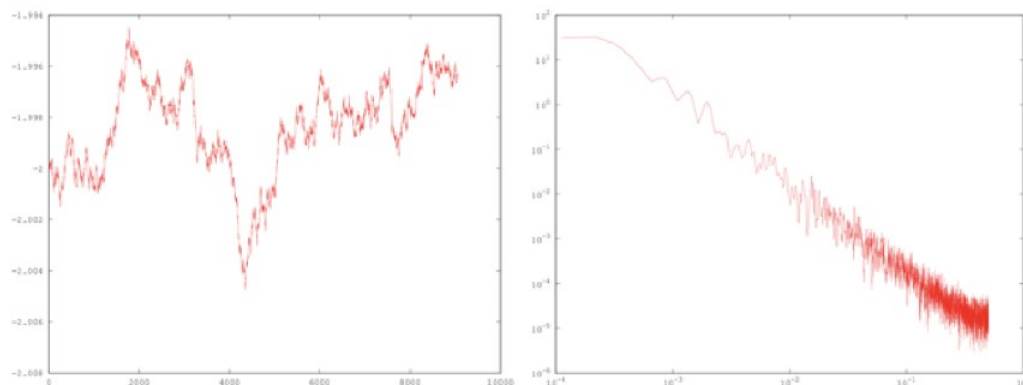


**Figure 4.3:** An unconverged MCMC chain (left panel) and its power spectrum (right panel): A converged MCMC chain is expected to exhibit the behavior of white noise. Thus, on the power spectrum, the power shall be uniformly distributed among different frequencies (after the burn-in phase of the MCMC). Here, the power tends to increase in lower frequencies, and the chain itself does not indicate the behavior of white noise. Therefore, this chain is not yet converged. Figure from Jonathan Sievers [137].

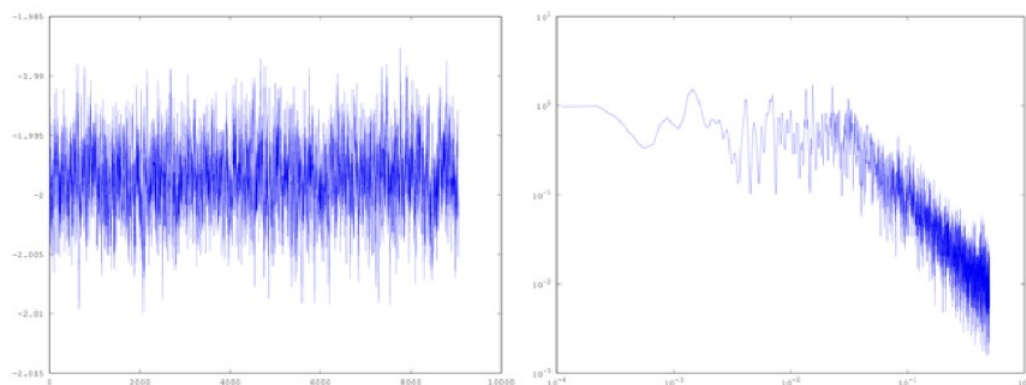


**Figure 4.4:** A converged MCMC chain (left panel) and its power spectrum (right panel): A converged MCMC chain is expected to exhibit the behavior of white noise. Thus, on the power spectrum, the power shall be uniformly distributed among different frequencies (after the burn-in phase of the MCMC). Here, the flat behavior of the power spectrum is evident, and the chain itself represents white noise. Figure from Jonathan Sievers [137].

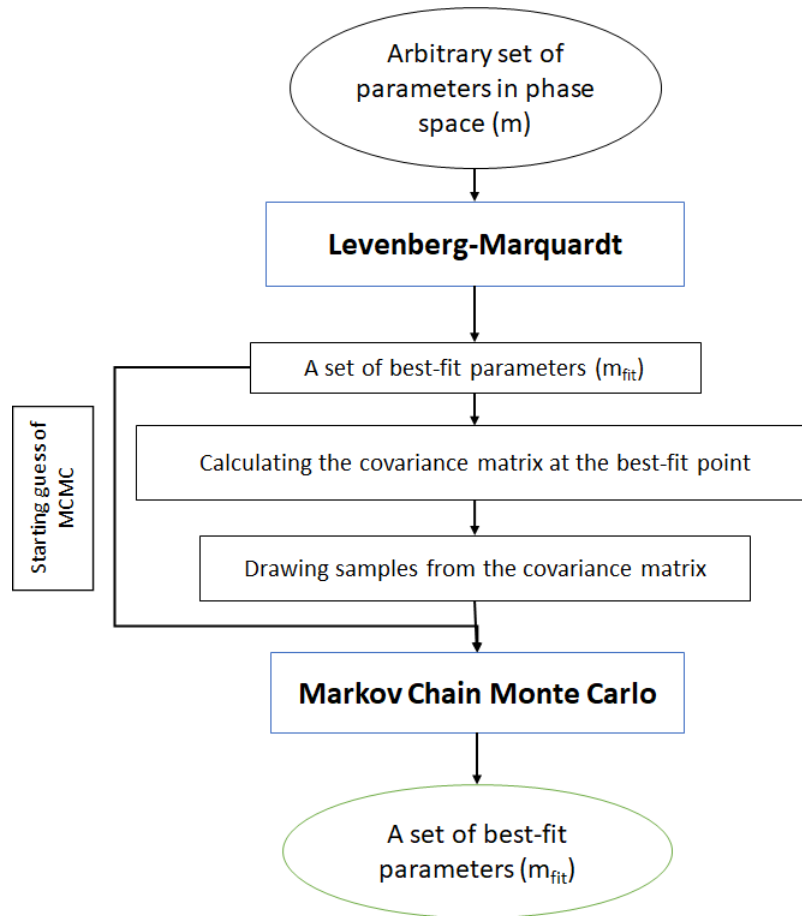


**Figure 4.5:** Flow chart of the procedure to combine MCMC and LM. We start with an arbitrary combination of parameters in phase space and run the LM algorithm to find the best-fit point and the covariance matrix. Then, we draw sufficient samples from the covariance matrix to use them as the posterior distribution of our MCMC. Eventually, the output of this combined method is a set of best-fit parameters and their associated error bars.

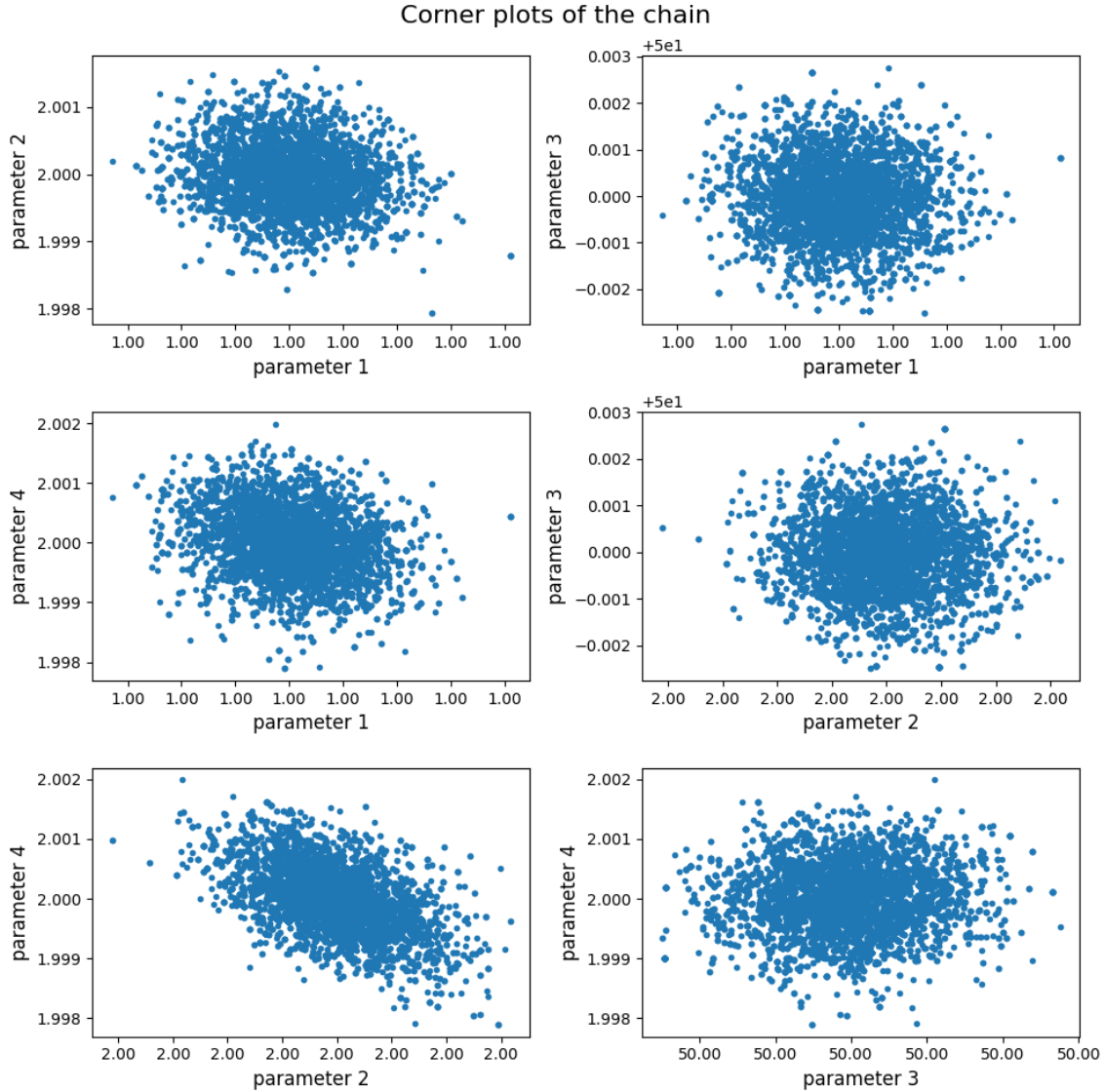


**Figure 4.6:** Corner plots (pairwise parameter contours) of a typical MCMC chain from a four-variable Gaussian model. A corner plot is the pairwise scatter plots of all the parameters in a MCMC chain, providing a visual assessment of the correlation between parameters. These plots are especially advantageous in dealing with high-dimensional parameter spaces. Corner plots are also capable of identifying possible degeneracies. In this figure, the lower right panel clearly shows patterns of correlation between a pair of parameters. Sampling from a multivariate normal distribution based on the covariance matrix associated with these samples will take the correlations into account.

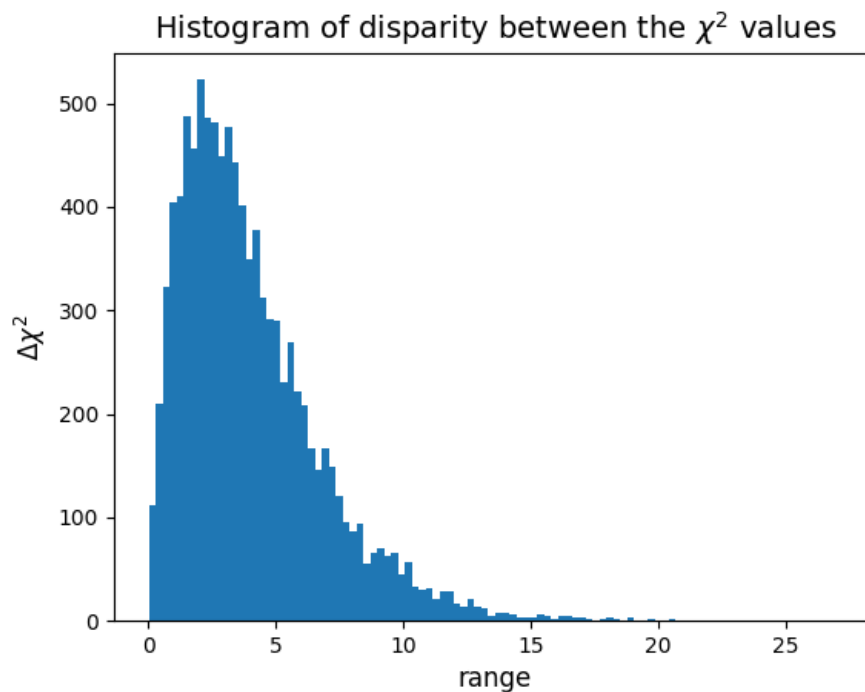


**Figure 4.7:** Histogram illustrating the distribution of the disparity between the chi-squares of drawn samples for a four-variable Gaussian model. The samples are drawn from the covariance matrix calculated at the point of best fit (output of LM). We expect the average difference in the  $\chi^2$  statistics for two different samples to be of order unity per each parameter. On this plot, the average of disparity is 4.03, and the standard deviation is 2.83, in acceptable agreement with our expectations. Therefore, the best-fit parameters are considered a "good fit".

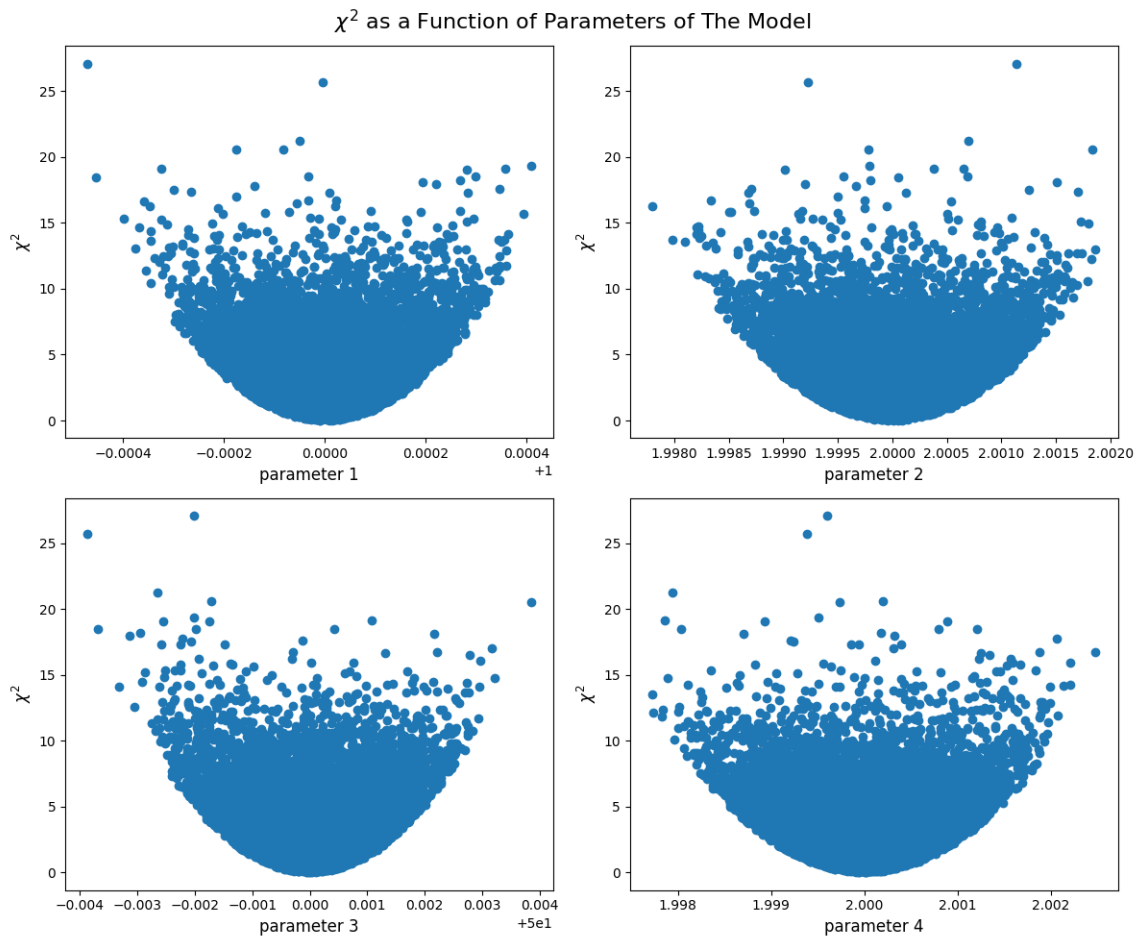


**Figure 4.8:** Figures demonstrating the values of chi-square associated with the drawn samples versus the values of parameters for a four-variable Gaussian model. The  $\chi^2$  is expected to have a parabolic dependency on the value of parameters based on its non-linear definition (4.1). This is a test to confirm the accuracy of the covariance matrix and the procedure of sample drawing.



## Chapter 5

# Results and Analysis

Following the discussions of chapter 4 on formulating a data fitting algorithm based on the synchronized utilization of LM and MCMC, this chapter is devoted to demonstrating the results of applying this method to the global 21cm signal. As an example, we offer a theoretical best-fit curve for the EDGES data.

An essential step in the process of model fitting is to determine the parameters of the physical model. As we choose to use ARES for generating the theoretical curve, the parameterization is restricted to the notation employed by ARES. We will briefly introduce our chosen parameters and revisit their connection to the underlying physics of the global 21cm line. We proceed by evaluating the quality of fit by estimating the parameters of a mock data set, which in fact, is an ARES-generated curve. The reliability of the results is proven by considering the values of estimated parameters and the assumed error bars of

the mock data.

Finally, we represent the results of parameter estimation for EDGES data. These results will show us that the anomalous behavior of this data (with respect to theoretical expectations) is an obstacle to providing a fit to this signal.

## 5.1 Key Astrophysical Parameters

Based on the discussions of 2.1, the shape and amplitude of the global 21cm signal is dependent on underlying astrophysical processes, especially those related to the Star Formation Rate (SFR) and reheating of the IGM. In this section, we will take the discussion further and address our current understanding of this dependency on four astrophysical parameters, which are able to map the parameter space of the global 21cm signal. Constraining these parameters will result in improved comprehension of the thermal history of the IGM and the population of X-ray sources during high-redshift epochs [3].

It is essential to mention that although it is theoretically possible to investigate the cosmological parameters with this signal as well (refer to equation 2.14 for the dependency of the global curve on cosmological parameters), the accuracy of the observational data is yet insufficient for constraining these parameters. Moreover, the 21cm signal is the only identified probe for some astrophysical mechanisms during the dark ages and EoR, while cosmological parameters can be studied using CMB as well. Therefore, we introduce four astrophysical parameters hereunder, which will form the basis of our analysis.

1.  $f_X$ : *High-redshift proportionality constant in X-ray luminosity and SFR relation* [35].

X-ray photons generated by galaxies and quasars are likely the most important cause of heating the low-density IGM [16]. Considering the fact that the nature of high-redshift objects is not properly studied, it is impossible to give an exact theory for the high-redshift X-ray background. The safest course of action is to assume that the relation between X-ray luminosity and SFR in high redshift contains a proportionality constant  $f_X$ <sup>1</sup>:

$$L_X = 3.4 \times 10^{40} f_X \left( \frac{SFR}{1 M_\odot \text{ yr}^{-1}} \right) \text{ erg s}^{-1}. \quad (5.1)$$

The normalization was chosen such that, when  $f_X = 1$ , the total X-ray luminosity per unit SFR is consistent with that observed in starburst galaxies at the present epoch [3, 16].

2.  $N_{lw}$ : *Number of photons emitted in the Lyman-Werner band ( $11.5\text{eV} < E < 13.6\text{eV}$ ) per baryon of star formation.* This parameter is referred to as *pop\_rad\_yield\_0\_* in ARES documentation [35, 138].
3.  $N_{ion}$ : *Mean number of ionizing photons ( $E > 13.6\text{eV}$ ) produced per baryon of star formation.* This parameter is referred to as *pop\_rad\_yield\_2\_* in ARES documentation [3, 35].

---

<sup>1</sup>A more precise calculation will reveal that  $f_X$  is not a constant, as it ascends with redshift. This comes from the fact that the primordial mass function is strongly weighted toward the high-redshift end, resulting in a larger proportionality constant between X-ray production and SFR at high redshifts.

4.  $f_{esc}$ : Fraction of ionizing photons that escape their host galaxy into the IGM [35].

$f_{esc}$  and  $N_{ion}$  are both defined in the process of calculating the evolution of ionization fraction  $\bar{x}_i$ :

$$\bar{x}_i = \frac{\zeta f_{coll}}{1 + \bar{n}_{rec}} \quad (5.2)$$

$$f_{coll} = \int_{m_{min}}^{\infty} dm \, m \, n(m) \quad (5.3)$$

$$\xi_{ion} = A_{He} f_* f_{esc} N_{ion} \quad (5.4)$$

$f_{coll}$  is the collapse fraction (fraction of gas inside collapsed objects, fraction of mass in halos more massive than  $m_{min}$ ),  $\bar{n}_{rec}$  is the mean number of recombinations per ionized hydrogen atom,  $\xi_{ion}$  is the ionizing efficiency,  $f_*$  is the star formation efficiency (fraction of baryons converted into stars), and  $A_{He} = 4/(4 - 3Y_p) = 1.22$ . The mass fraction of helium,  $Y_p$ , is a correction factor to convert the number of ionizing photons per baryon in stars to the fraction of ionized hydrogen. Our limited understanding of the mass distribution of the emitting stars causes an uncertainty in the number of ionizing photons per baryon  $N_{ion}$ , that is emitted by galaxies. There is also considerable uncertainty in the fraction of ionizing photons  $f_{esc}$  that escape their host galaxy to ionize the IGM. Therefore, our study is toward the demand to constrain these parameters with observational data [3, 16].

Alternatively, we could have utilized  $f_*$  as a parameter of our model. However, since

$f_{esc}$  and  $N_{ion}$  act as multiplication factors to  $f_*$  in the expression for ionizing efficiency

5.4, thus, both of them are individually degenerate with star formation rate.

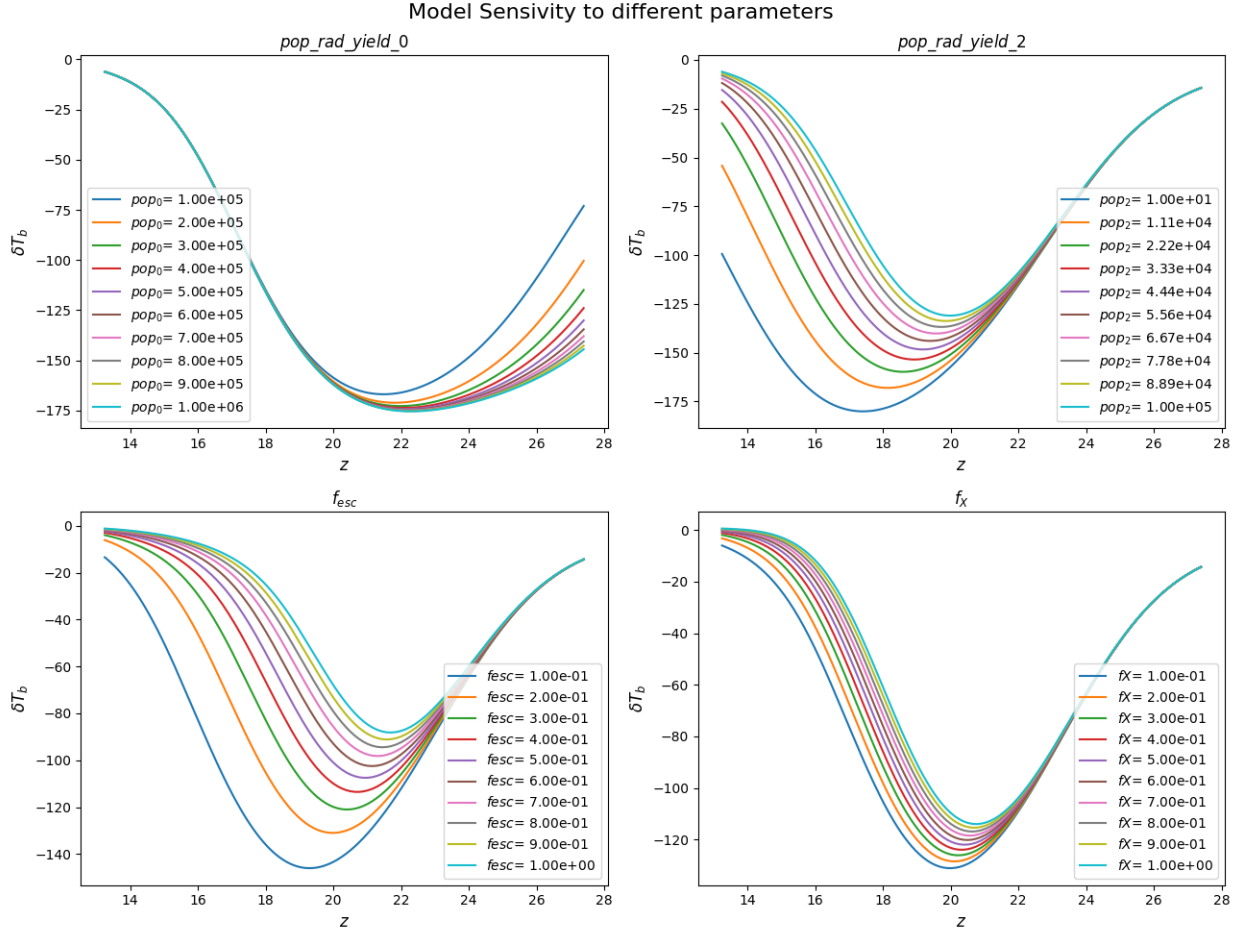


**Figure 5.1:** Behaviour of ARES-generated global 21cm models with respect to four astrophysical parameters: *pop\_rad\_yield\_0*-, *pop\_rad\_yield\_2*-,  $f_{esc}$ , and  $f_X$ . In each panel, the corresponding parameter possesses 10 different values, and other parameters are kept at the values of  $10^4$ ,  $10^5$ , 0.2, and 0.1, respectively. Each parameter is capable of affecting the shape and depth of the absorption trough.

Figure 5.1 shows the influence of change in the values of the above-mentioned parameters

on the global 21cm curve generated by ARES. It must be noted that these parameters are only physically meaningful in a limited region of phase space (a hypercube where the combination of parameters is physically meaningful). Going beyond this region will result in a failure in calculating the global 21cm curve. our developed script is designed to handle this issue and stop it from aborting the whole run <sup>2</sup>, but the MCMC might not be able to reach convergence if the algorithm faces numerous samples beyond the allowed region.

## 5.2 Parameter Estimation of Mock Data

Prior to applying our developed algorithm to fit real-world data, we perform a validation test by using it to fit a mock data set. We create an ARES curve based on a predetermined set of parameters, treating it as mock data with an assumed error bar of  $10^{-3}\text{K}$  on each data point. We confirm the correct functioning of the algorithm by comparing the obtained fitted parameters to the expected values.

The results of this validation test are shown in Table 5.1. The initial row contains the genuine parameters employed in generating the mock data, while the second row exhibits the fitting outcome. Subsequently, the third row displays the one-sigma error bar of the fit, which is based on the standard deviation of MCMC chain. The last row demonstrates the relative fitting error, which serves as a measure for assessing the disparity between the true

---

<sup>2</sup>The Python code for the MCMC is designed such that it will return an arbitrarily large chi-square for that combination of parameters beyond the permitted hypercube. Therefore, the probability of these points getting accepted into the chain will be automatically low.

values of astrophysical parameters and their corresponding fit.

Figure 5.2 is the illustration of the data in table 5.1. The blue dotted curve and the red curve on the left panel depict the mock data and the corresponding fit, respectively. On the other hand, the right panel, which is the zoomed version of the same plot, demonstrates the two-sigma confidence interval of the fit. The overall output is an acceptable fit considering both the shape and amplitude of the signal.

Figure 5.3 indicates the white-noise behavior of parameters throughout the chain, and Figure 5.4 shows a flat behavior for the chain power spectrum, which is both in agreement with our anticipation for a converged chain. Performing *chi-Square consistency test* on our samples showed that the average disparity between the chi-square of drawn samples is 49.20 (Figure 5.5), roughly an order of magnitude larger than the initial expectation ( $\approx 4$ ) (refer to Figure 4.7). The *chi-square parameter correlation test* (Figures 5.6) did not show parabolic behavior initially. However, Figure 5.7, which demonstrates the zoomed version of the 5.6, gives insights on parabolic behavior for lower values of chi-square. Figure 5.8 illustrates the corner plots of this chain. The lower left panel indicates that the  $f_X$  and  $pop\_rad\_yield\_2$  have the highest amount of correlation in all pairs of parameters.

### 5.3 Parameter Estimation of EDGES data

This section demonstrates the results of applying our developed method to the EDGES data, which is the only claimed observational data set of the global 21cm signal. We formerly

Parameter Value	$pop\_rad\_yield\_0\_$	$pop\_rad\_yield\_2\_$	$f_{esc}$	$f_X$
True values	$1 \times 10^4$	$1 \times 10^3$	0.1	0.1
Fitted values	$9.9999 \times 10^3$	$9.9941 \times 10^2$	$1.0002 \times 10^{-1}$	$1.0000 \times 10^{-1}$
Error-bar of fit	$3.4727 \times 10^{-2}$	$3.8932 \times 10^0$	$3.6299 \times 10^{-4}$	$3.3186 \times 10^{-6}$
Fitting Error	0.0001%	0.0264 %	0.0152%	0.0003%

**Table 5.1:** Results of fitting a mock data set with MCMC chain. The first row is the actual parameters used to generate the mock data. The second row is the fit value of the same astrophysical parameters. The third row is the one-sigma error bar of fit, and eventually, the fourth row represents the relative fitting error which is a measure of disparity between the values of the first and second rows.

discussed that standard physical mechanisms are unable to explain the large amplitude of this data as it is roughly more than two times higher than the most optimistic theoretical curves. On the other hand, ARES, which generates the theoretical global 21cm curve, is based on the predictions of standard physics. Therefore, in order to gain a more realistic fit of the EDGES data, we tend to use a suppressing multiplication factor which draws the amplitude of the data to half of its original value. Furthermore, as a matter of convenience in the first-step analysis, we refrain from employing the actual noise model used by the EDGES group. Instead, we approximate the noise using the radiometer equation. The details of this approach is presented in section 5.3.1.

### 5.3.1 Error Bar Calculation

In order to obtain the error bars of the EDGES data for the parameter estimation process, it is possible to use the EDGES noise model directly. Another option is to take advantage



of the approximation provided by the radiometer equation, which expresses the sensitivity of a radio antenna [139, 140]:

$$\frac{\delta T}{T_{sys}} = \frac{1}{\sqrt{Bt}}, \quad (5.5)$$

where  $B$  is the bandwidth,  $t$  is the exposure time, and  $T_{sys}$  is the system temperature. Assuming a bandwidth of  $10^6$  Hz, an exposure time of one day, and a temperature of 3000 K, we get:

$$\delta T_{EDGES} = 10^{-2} \text{ K} = 10 \text{ mK}. \quad (5.6)$$

### 5.3.2 Results

The outcomes obtained by applying our methodology to the EDGES data are presented in Table 5.2. In the first row, the best-fit parameters for the half-amplitude data are displayed. Subsequently, the second row exhibits the one-sigma error bar of the fit, derived from the standard deviation of the MCMC chain.

Figure 5.9 is the visual demonstration of the data from Table 5.2, with the blue dotted curve representing the data and the red curve portraying the corresponding fit on the left panel. The right panel, being a zoomed version of the same plot, illustrates the two-sigma confidence interval of the fit. The overall findings reveal a notable discrepancy when compared to the observed data, suggesting the implausibility of achieving the EDGES curve by solely considering the expectations of standard physics.

Figure 5.10 shows the white-noise behavior of parameters throughout the chain, and Figure 5.11 shows a flat behavior for the chain power spectrum, confirming that it has converged. The performed *chi-square consistency test* on the samples indicated an average disparity of 0.28 between the chi-square values of the drawn samples (Figure 5.12), significantly lower (roughly two orders of magnitude) than the initial expectation of approximately 4. The *chi-square parameter correlation test* (Figures 5.13) revealed parabolic behavior only for parameters *pop\_rad\_yield\_2* and  $f_X$ . However, upon examining the zoomed version of Figure 5.13 in Figure 5.14, it became evident that the two remaining parameters also exhibit parabolic behavior at lower values of chi-square.

The chain's corner plots are depicted in Figure 5.15. Among all six panels, only the middle left panel, which represents the values of  $f_X$  and *pop\_rad\_yield\_0*, demonstrates a correlation between a pair of parameters.

While the results of the validity tests, including the chi-square consistency test and chi-square parameter correlation test, did not meet our initial expectations for both mock and EDGES data, we have compelling evidence that the MCMC chains have achieved complete convergence (refer to Figures 5.4 and 5.11). Furthermore, we demonstrated that the same methodology successfully passed the validity tests when employing a simple four-variable Gaussian model (Refer to Figures 4.7 and 4.8). Consequently, the discrepancy observed in the validity test results appears to stem from the theoretical model generator, ARES. It is plausible that the chosen parameterization is unsuitable, and the inherent degeneracy in

parameter definitions may be contributing to the observed issues.

Parameter Value	$pop\_rad\_yield\_0\_$	$pop\_rad\_yield\_2\_$	$f_{esc}$	$f_X$
Fitted values	$4.5493 \times 10^3$	$2.4759 \times 10^3$	$3.7010 \times 10^{-1}$	$1.3639 \times 10^{-1}$
Error-bar of fit	$1.8083 \times 10^{-1}$	$7.6298 \times 10^1$	$1.1408 \times 10^{-2}$	$6.5033 \times 10^{-6}$

**Table 5.2:** Results of fitting EDGES data with MCMC chain. The upper row is the fit value of four astrophysical parameters of the model, and the lower row is the one-sigma error bar of fit. We anticipated the fitted value for  $f_X$  to exceed 1, given that it is set to unity for the local universe. The observed discrepancy implies a potential issue either in the EDGES data or in the assumptions made during the definition of  $f_X$  (refer to section 5.1 for the exact definition of  $f_X$ ).

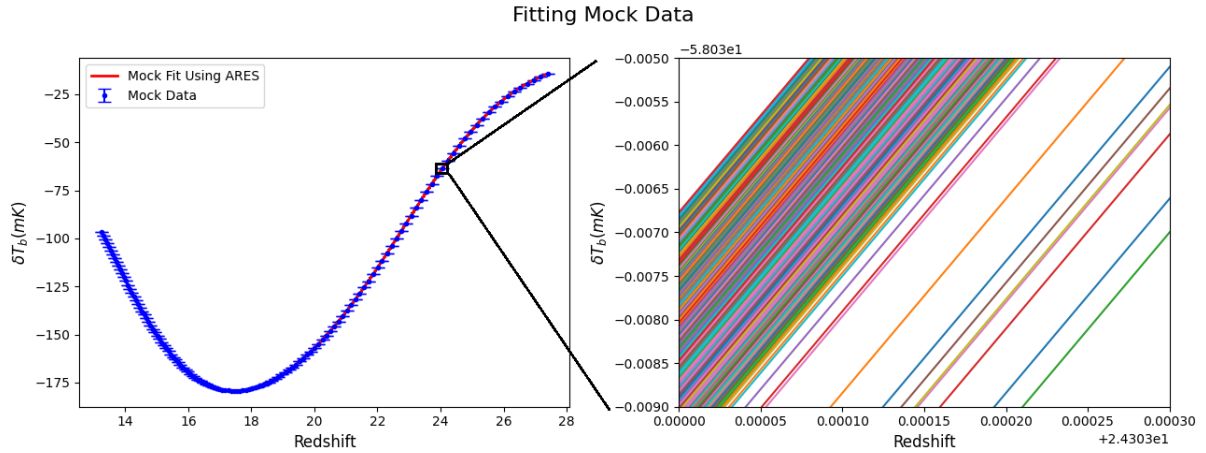


**Figure 5.2:** Results of fitting mock data. On the **left panel**, the blue dotted curve represents the mock data and the assumed uncertainty ( $10^{-3}\text{K}$ ) generated by feeding the parameters of table 5.1 to ARES. The red curve demonstrates the fit curve, which is an excellent fit to the data, further validating the developed fitting method. The **right panel** is the zoomed version of the left figure, showing the two-sigma confidence interval of the fit (8698 distinctive curves), which is not visible on the left.

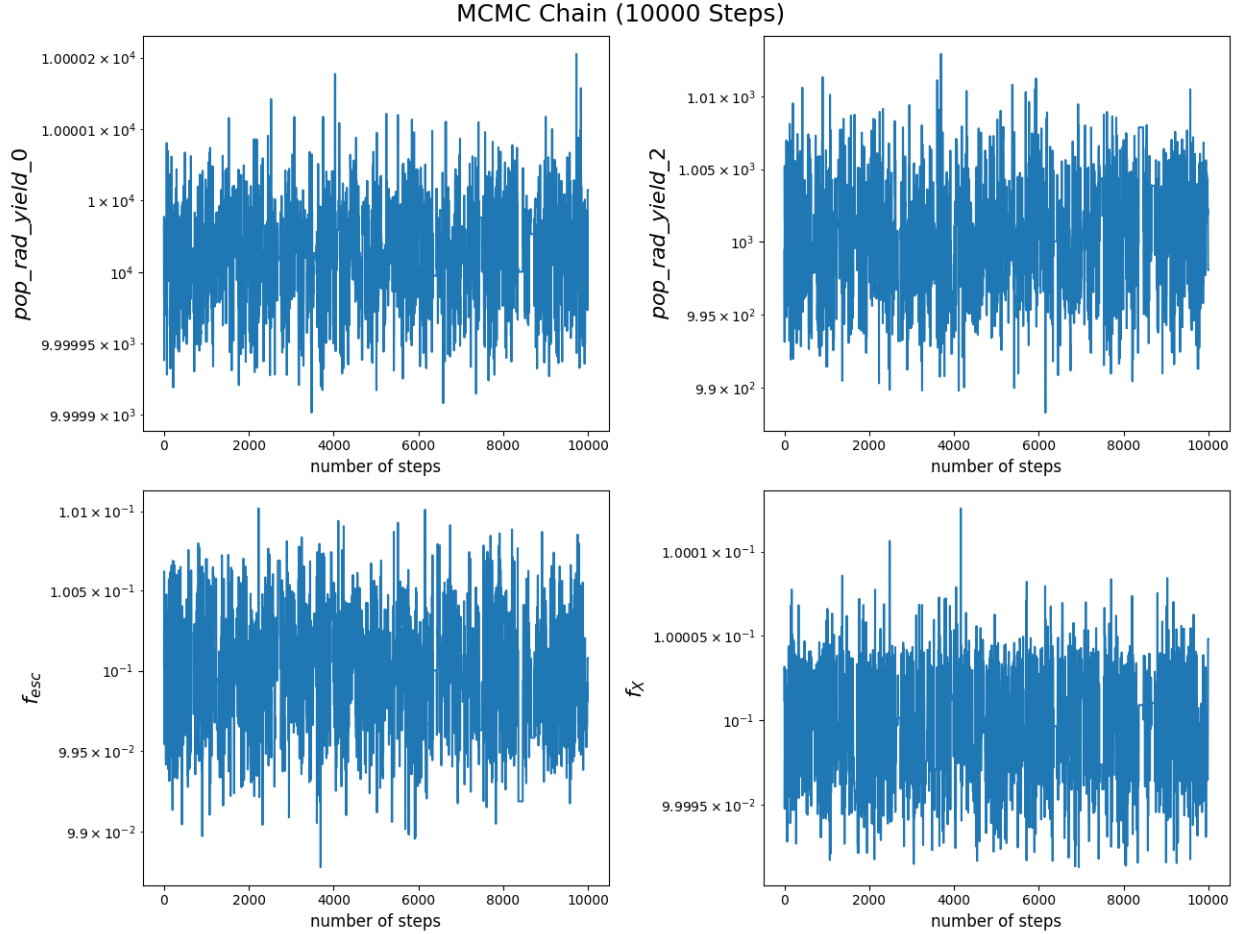


**Figure 5.3:** Trend of parameters in the  $10^4$  steps MCMC chain to fit the mock data. The depicted white noise behavior is considered as the sign of the convergence of the MCMC chain (refer to section 4.2.1). The acceptance ratio of the chain is 20.5%. The one-sigma error bar of the fit (table 5.1) is the standard deviation of this chain.

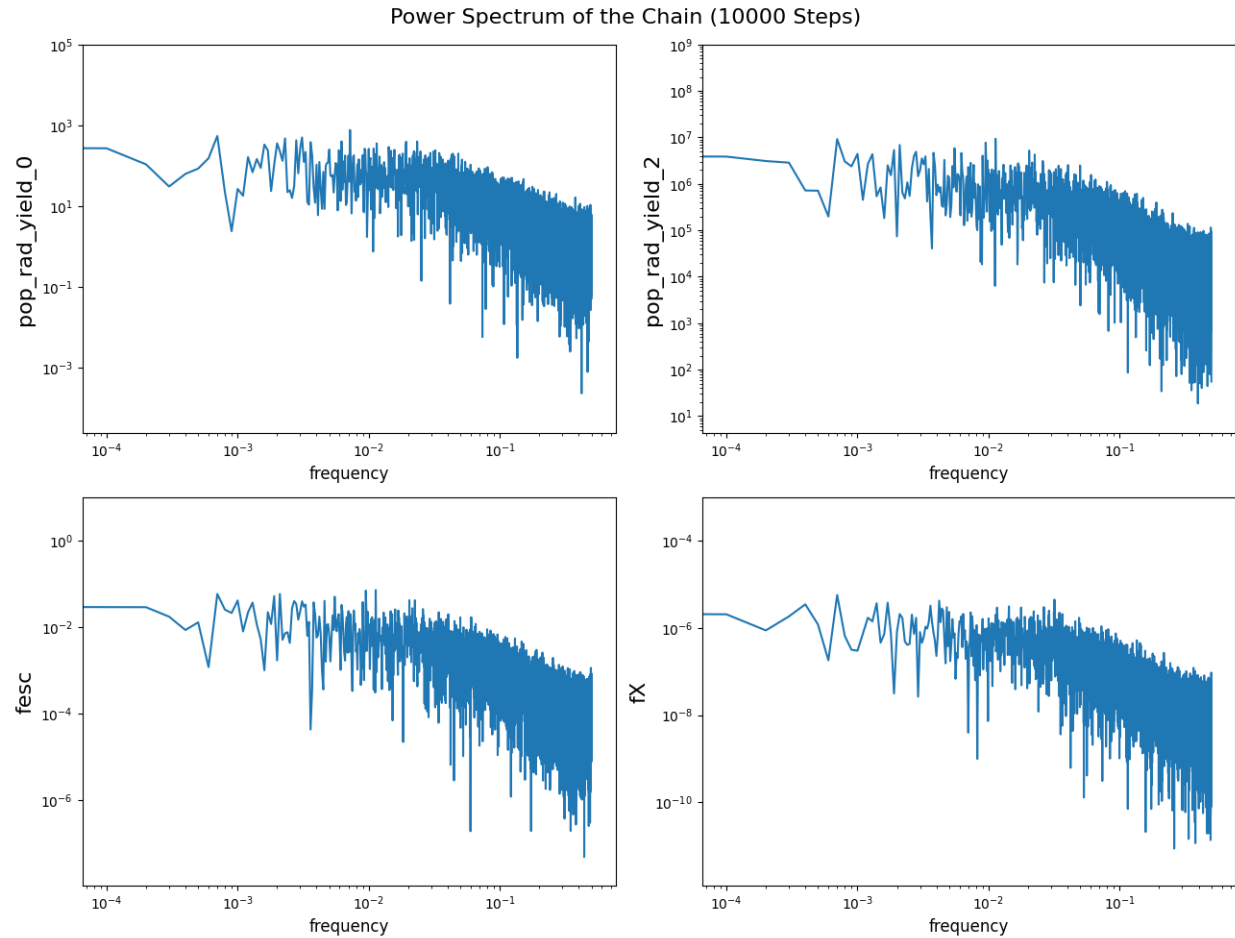


**Figure 5.4:** Power Spectrum of the  $10^4$  steps MCMC chain to fit the mock data. The power is uniformly distributed among different frequencies after the burn-in phase. Therefore, this plot is the proof for convergence of the chain (refer to section 4.2.1).

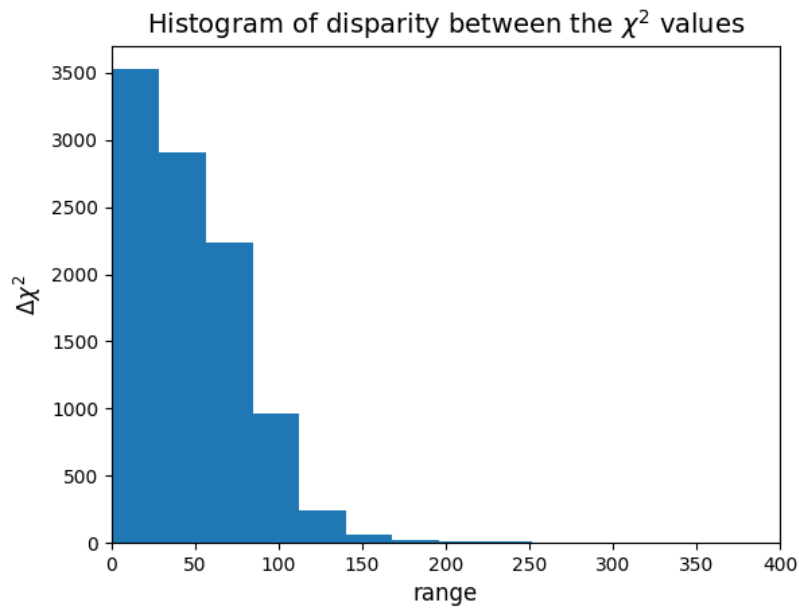


**Figure 5.5:** Histogram of disparity in the chi-square of drawn samples for the mock data MCMC chain, the mean is 49.20 with a standard deviation of 41.98. Based on the discussions of 4.4.1, we expected the mean to be approximately 4.

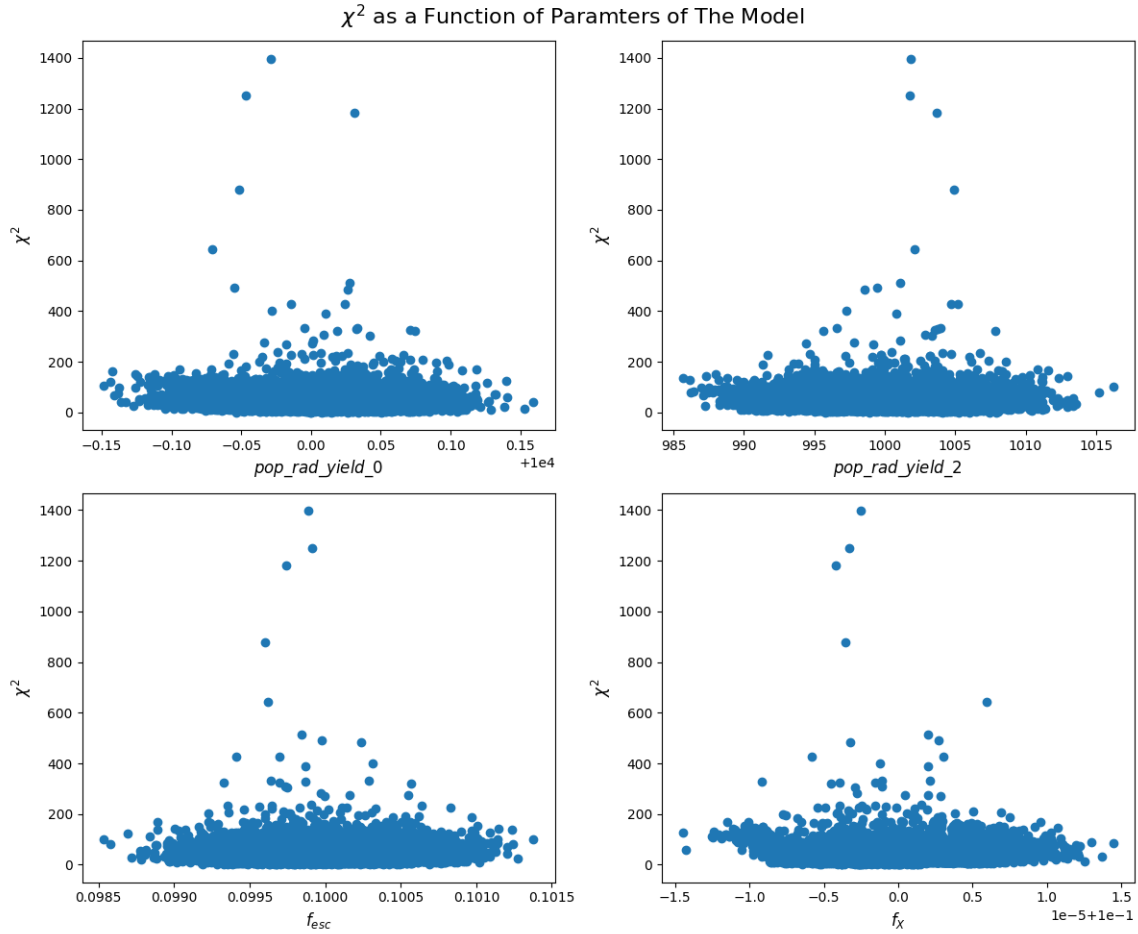


**Figure 5.6:** Figures demonstrating the values of chi-square associated with the drawn samples versus the values of parameters for the mock data set. The  $\chi^2$  is expected to have a parabolic dependency on the value of parameters. However, the parabolic behavior is not obvious in these plots.

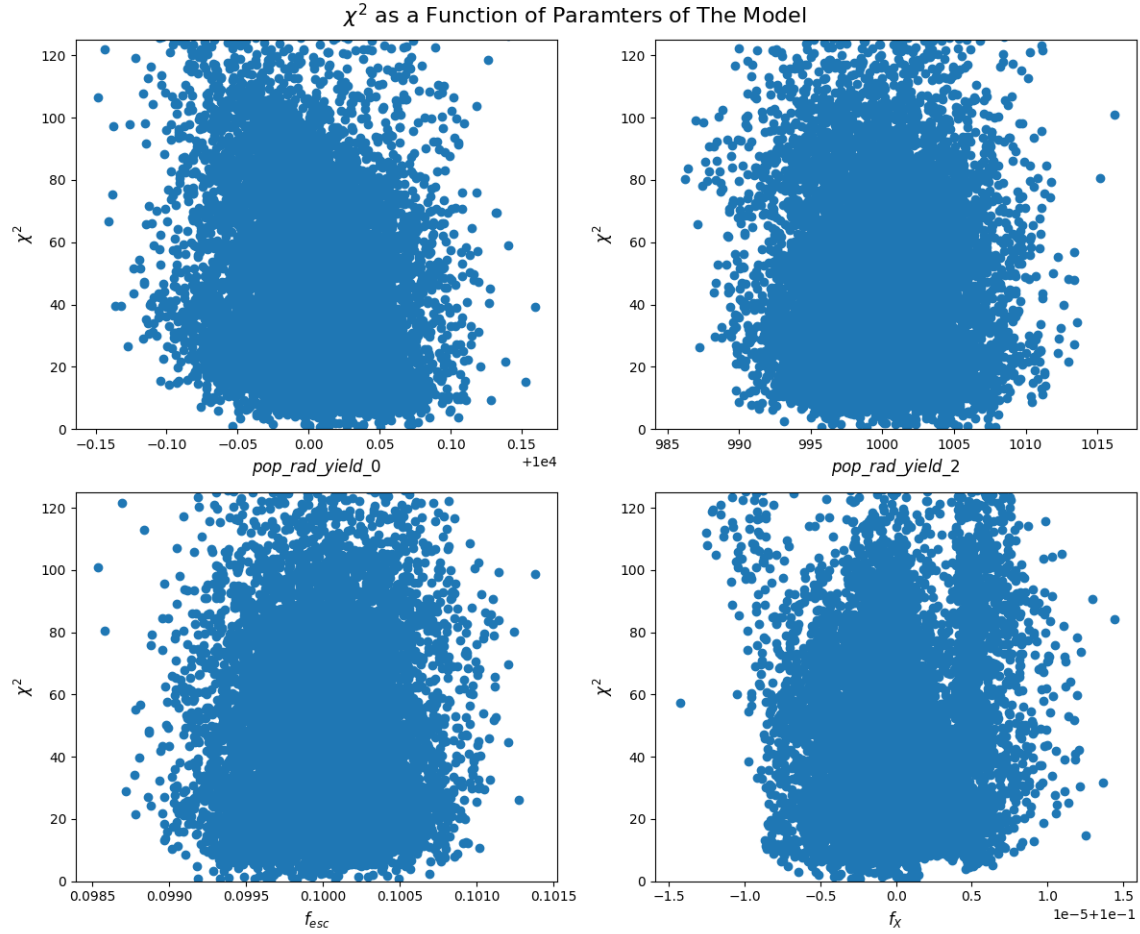


**Figure 5.7:** Zoomed version of figure 5.6, A weak parabolic behaviour is observed for low values of  $\chi^2$ . However, the overall shape is not completely consistent with the expectations of Figure 4.8.



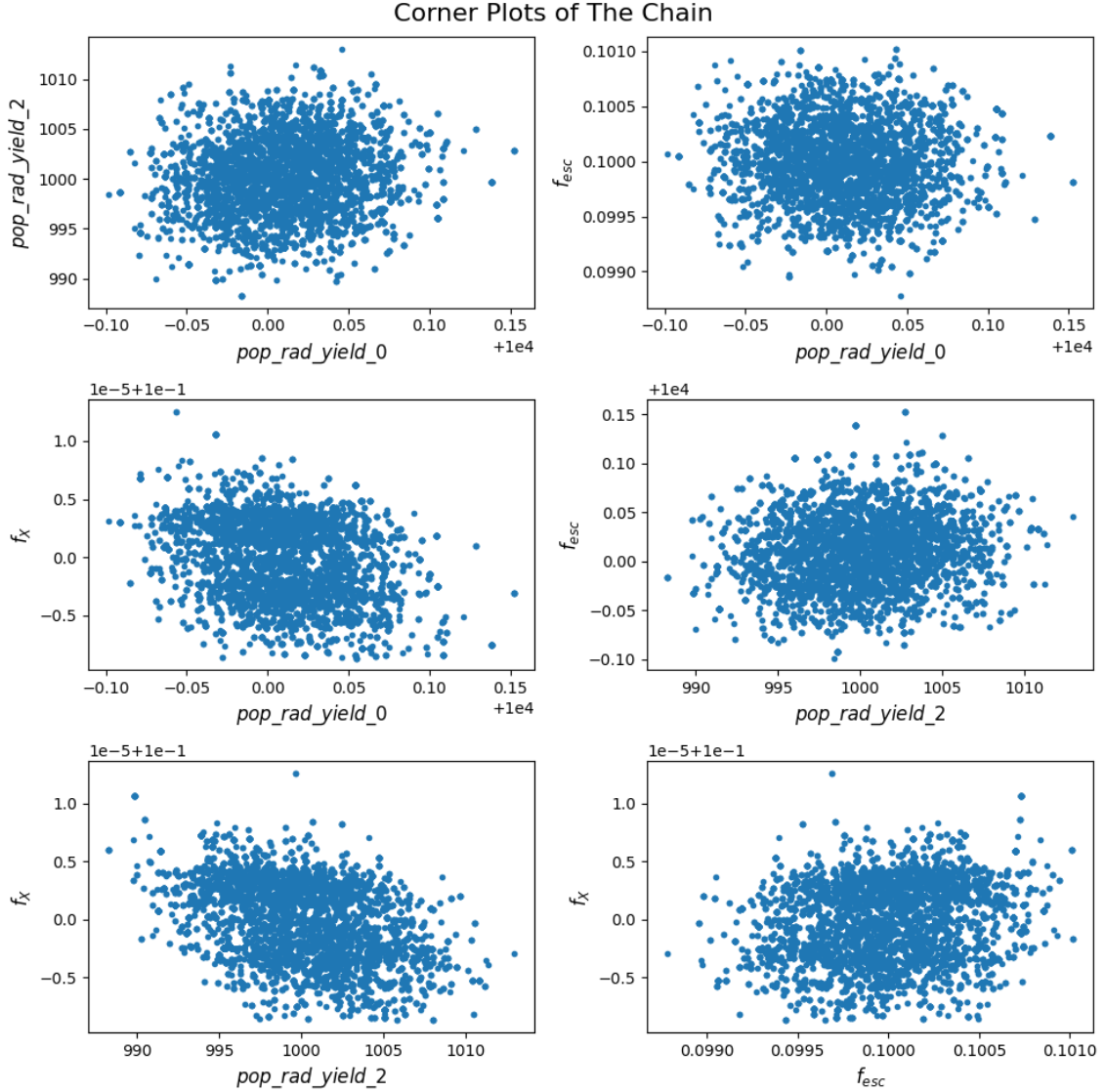


**Figure 5.8:** Corner plots of the mock data chain indicate the correlation between the parameters. The lower left panel, which depicts the values of  $f_X$  and  $pop\_rad\_yield\_2$ , shows the highest amount of correlation between a pair of parameters among all the six panels.

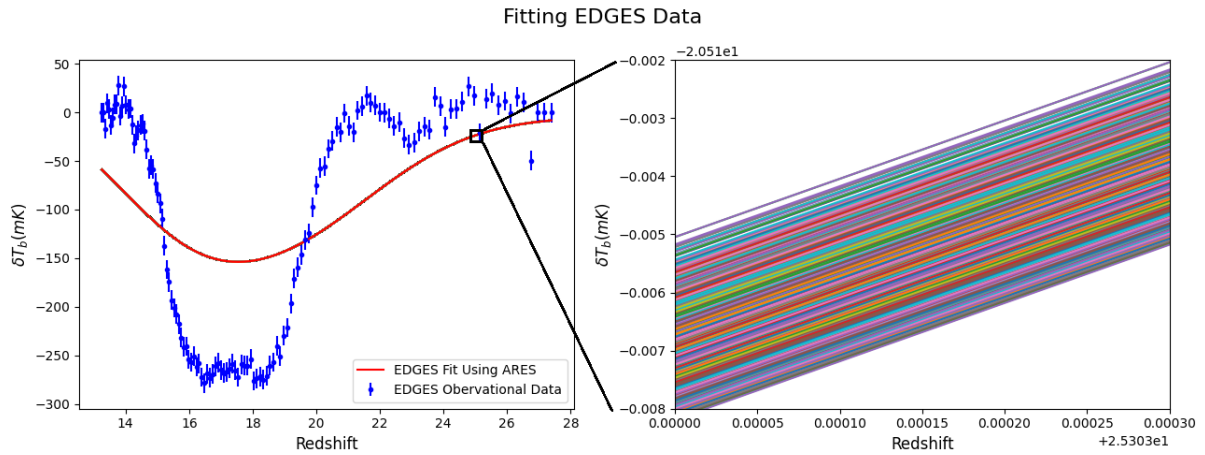


**Figure 5.9:** Results of fitting EDGES data. On the **left panel**, the blue dotted curve represents the half-amplitude EDGES data and the associated uncertainty calculated using the radiometer equation (10mK). The red curve demonstrates the fit curve (table 5.2). Despite using the half-amplitude data, the fit portrays a significant discrepancy with respect to the observed data, further suggesting the impossibility of achieving the EDGES curve with the current well-accepted standard physics. The **right panel** is the zoomed version of the left figure, showing the two-sigma confidence interval of the fit (8780 distinctive curves), which is not visible on the left.

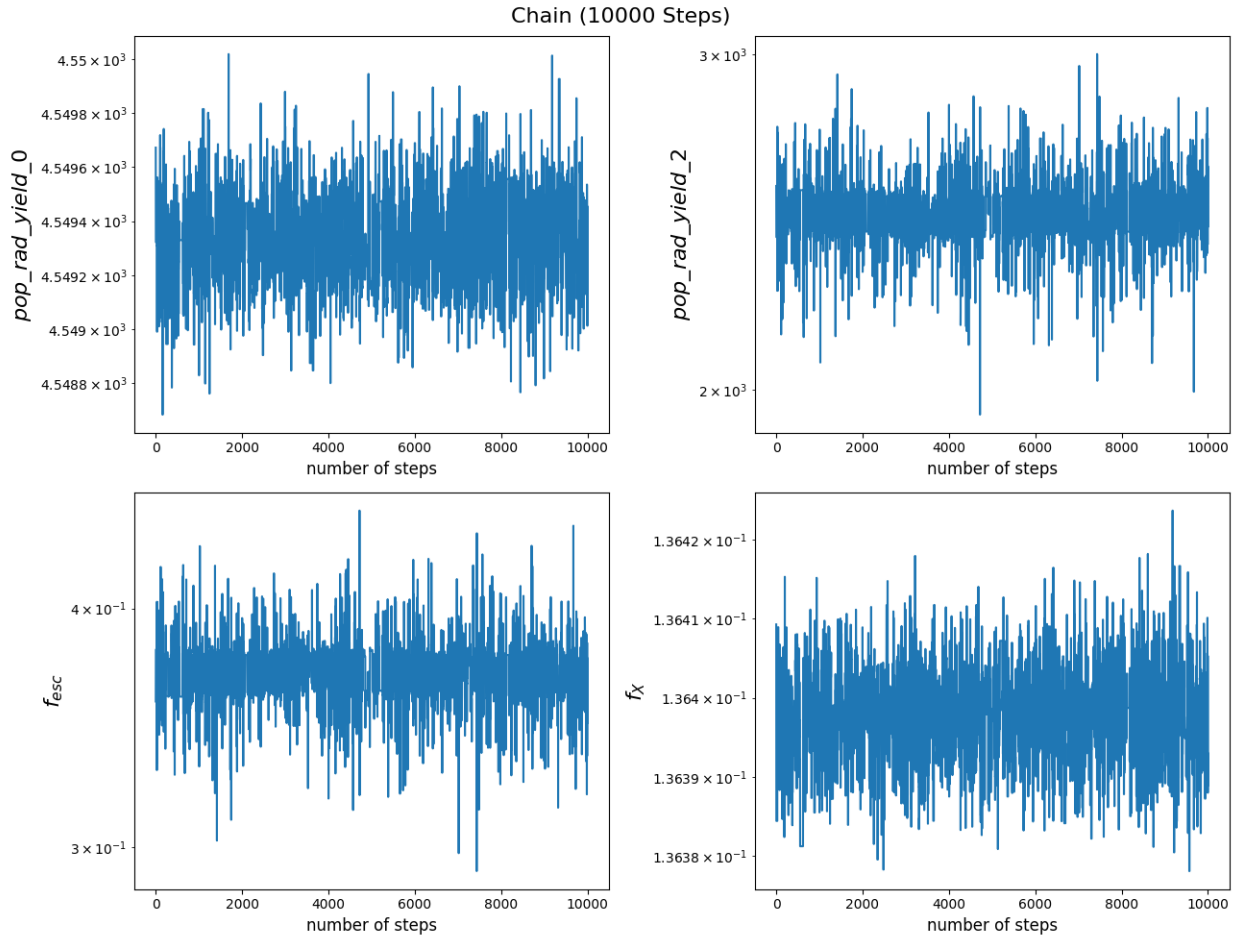


**Figure 5.10:** Trend of parameters in the  $10^4$  steps MCMC chain to fit the EDGES data. The depicted white noise behavior is considered as the sign of the convergence of the MCMC chain (refer to section 4.2.1). The acceptance ratio of the chain is 23.02%. The one-sigma error bar of the fit (table 5.2) is the standard deviation of this chain.

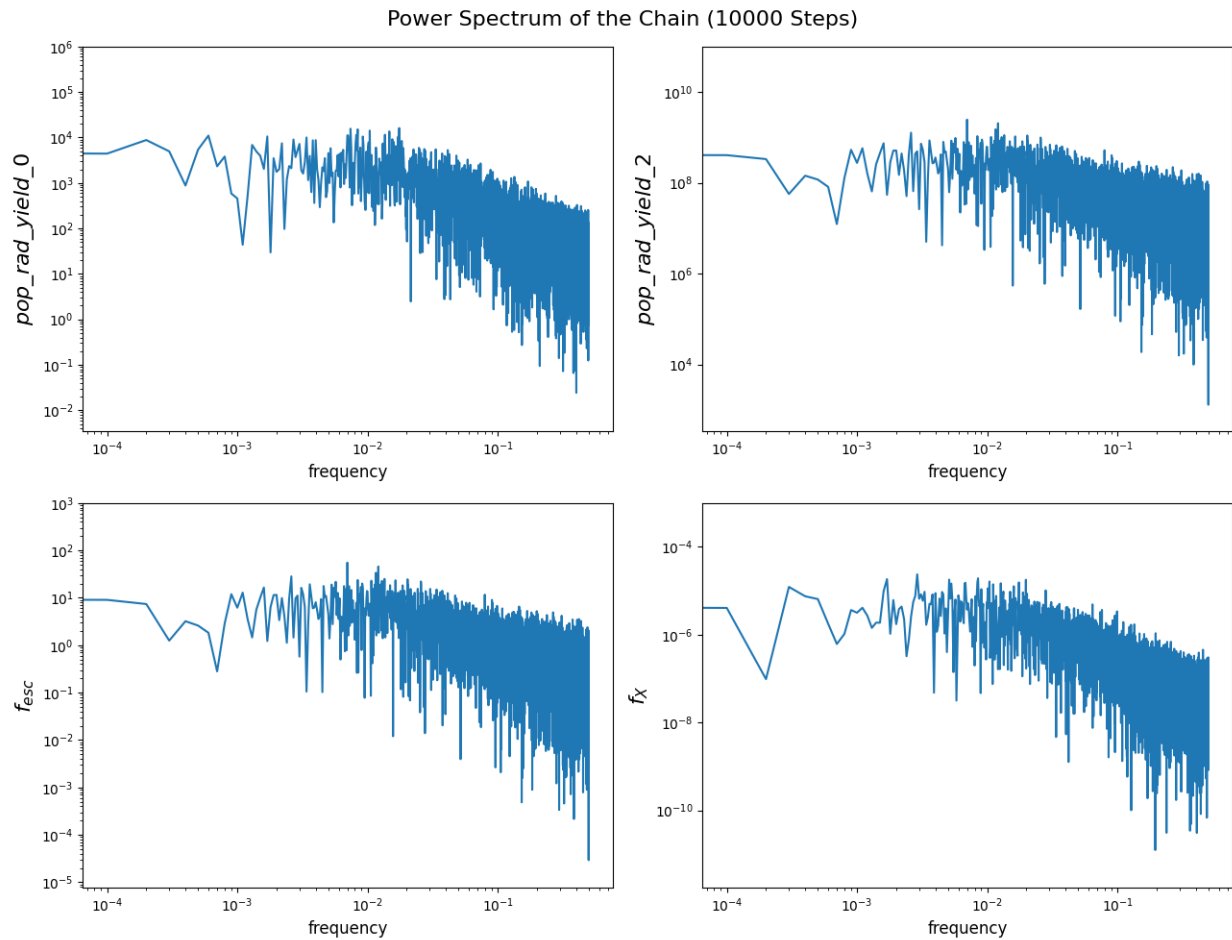


**Figure 5.11:** Power Spectrum of the  $10^4$  steps MCMC chain to fit the EDGES data. The power is uniformly distributed among different frequencies after the burn-in phase. Therefore, this plot is the proof of convergence of the chain (refer to section 4.2.1).

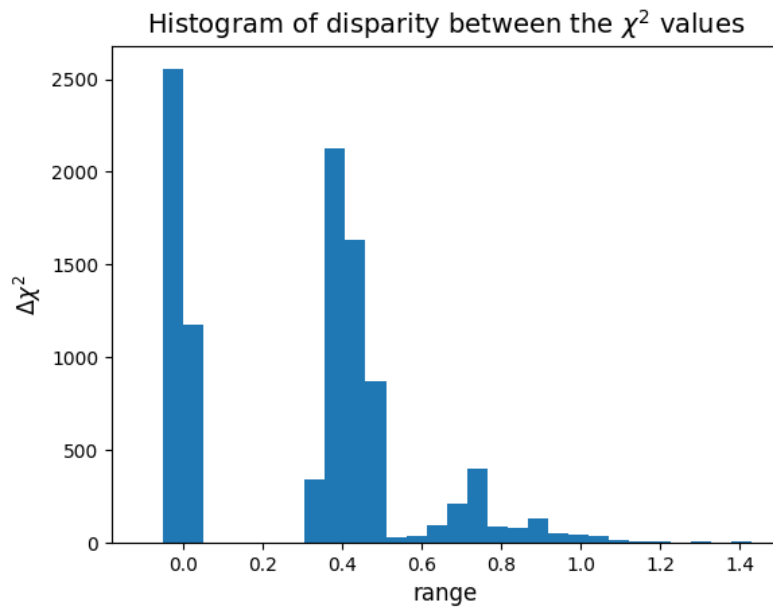


**Figure 5.12:** Histogram of disparity in the Chi-Square of drawn samples for the EDGES data MCMC chain, the mean is 0.28 with a standard deviation of 0.3. Based on the discussions of 4.4.1, we expected the mean to be approximately 4.

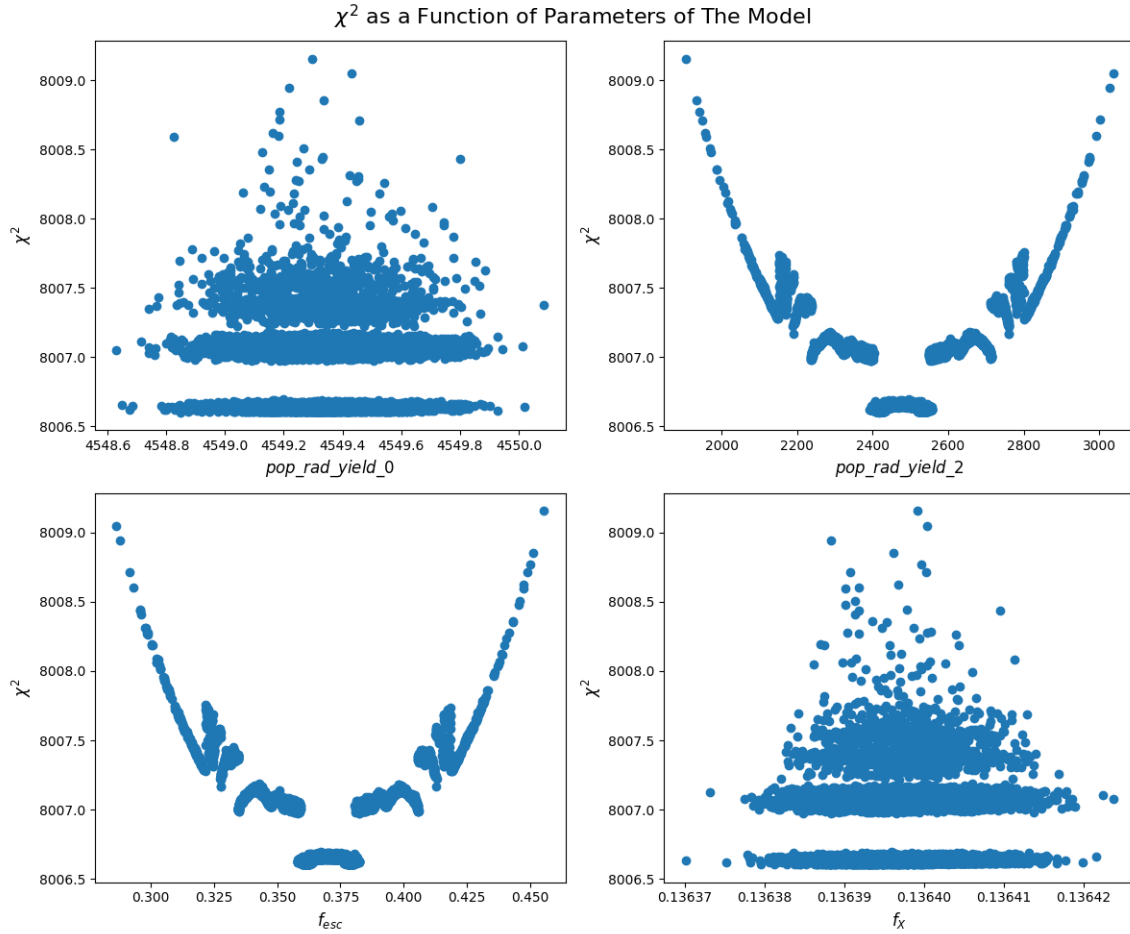


**Figure 5.13:** Figures demonstrating the values of chi-square associated with the drawn samples versus the values of parameters for the EDGES data set. The  $\chi^2$  is expected to have a parabolic dependency on the value of parameters, which is only evident in two of the panels (upper left and lower right).

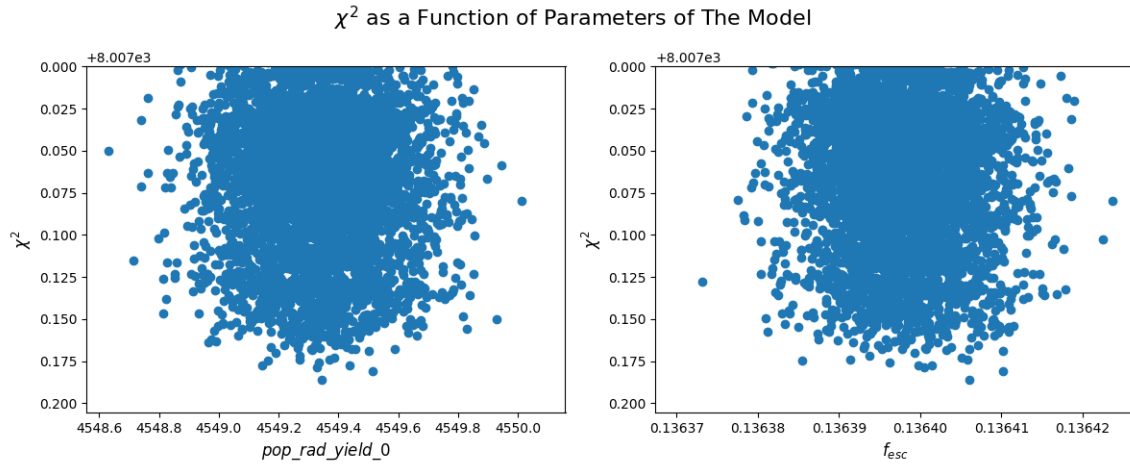


**Figure 5.14:** Zoomed version of the upper left and lower right panels of Figure 5.13. A weak parabolic behavior is observed for low values of  $\chi^2$ . However, the overall shape is not completely consistent with the expectations of Figure 4.8.

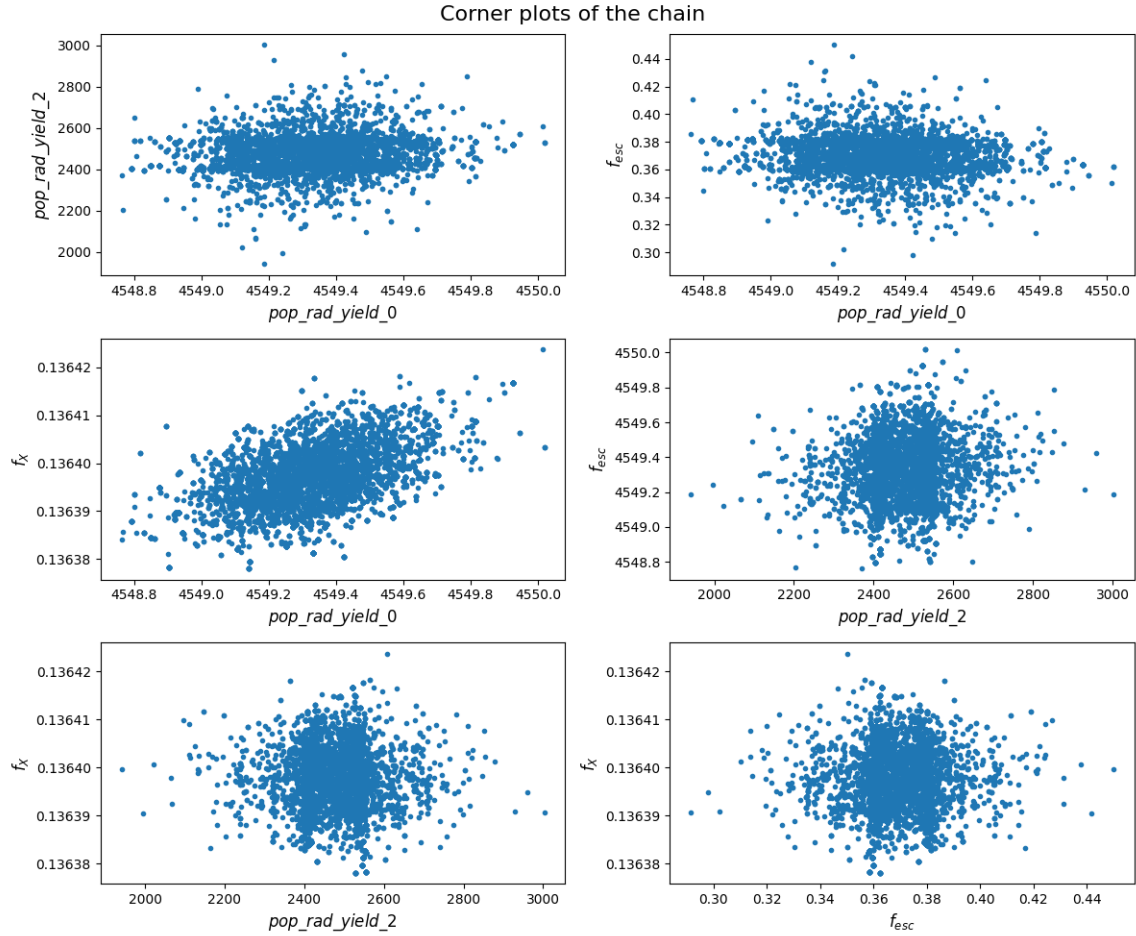


**Figure 5.15:** Corner plots of the EDGES data MCMC chain indicate the correlation between the parameters. The middle left panel, which depicts the values of  $f_X$  and  $pop\_rad\_yield\_0$ , appears to show the only correlation between a pair of parameters among all the six panels.



## Chapter 6

# Summary and Conclusion

Constraining the period between the dark ages and reionization has recently emerged as one of the challenges of modern radio astronomy. The motivation behind this interest is the fact that there is a clear correlation between the key features of the global 21cm signal and underlying astrophysical properties of the high redshift Universe (e.g.,  $\text{Ly}\alpha$  intensity, the X-ray heating rate, and the production rate of ionizing photons). These correlations can be used to directly link measurements of the global 21cm signal to astrophysical quantities [141]. Therefore, numerous researchers have conducted various parameter estimation methods for the data gathered from the observations focused on this signal.

In [142], authors reported one of the first attempts to forecast constraints on four astrophysical parameters of interest from mock observations of the global 21cm signal. They especially focused on the behavior of the turning points on the global curve to

constrain model parameters. Such measurements have the ability to constrain the ionization and thermal state of the IGM simultaneously. On the other hand, a combined study of the 21cm power spectrum and global signal measurements has the benefit of reducing the number of essential parameters needed to describe the global signal. Moreover, taking advantage of this new piece of information will result in a lower error bar on the values of cosmological parameters compared to the previously reported constraints [143].

In an attempt to constrain astrophysical and cosmological parameters at the same time, the *CosmoReionMC*, a MCMC-based parameter estimation package, was introduced in 2021. The theoretical model of this analysis includes the effect of five cosmological and seven astrophysical parameters (related to stellar populations). Utilization of this package on EDGES data showed that a short-lived population of metal-free (PopIII) stars with efficient radio emission is required to match the reported absorption amplitude. This new finding suggested an earlier reionization compared to the analysis only based on CMB and quasar data. Although this method was successful in matching the position and depth of the EDGES absorption trough, however, its abilities were limited in matching the exact shape of the signal [133].

Besides the traditionally well-known MCMC approaches, ANNs may also be used to extract the astrophysical parameters from the simulated and observational data sets and infer the physical state of the gas at high redshifts. This method showed particular precision

in the mock data and was able to construct the magnitude of the EDGES data but faced difficulties in mimicking the flattened nature of this observational signal [135].

Motivated by the findings of previous studies, in this thesis, we examined the capability of the global 21cm signal to assist us in our investigation of the existence of mechanisms beyond the standard model of cosmology and particle physics. The literature review provided a recap of the physics of the 21cm special line, its evolution through the thermal history of the universe, computational tools to simulate the global signal, and the signatures of non-standard physics. We also discussed the experimental efforts to observe this signal through the utilization of radio interferometers and the associated challenges and obstacles.

Knowing the fact that the global 21cm signal is sensitive to the underlying astrophysical processes, it is expected that the majority of the suggested non-standard scenarios would leave imprints on the value of the corresponding parameters. Therefore, we are optimistic that if such theoretical proposals exist in the early universe era, they will be revealed through parameter estimation of the existing and upcoming data. Following this idea, we introduced a parameter estimation method based on the coordinated use of LM and MCMC, providing a robust framework for fitting the observed data and exploring the parameter space, respectively. By employing this method, we developed a Python script specially designed for global 21cm applications, which takes advantage of an efficient simulator, ARES, to generate the theoretical model.

Finally, we presented the results of applying this method to the only claimed detection

of global 21cm signal, the EDGES data. Considering the anomalous amplitude and shape of the reported signal and the fact that the current version of our simulator ARES only contains the standard mechanisms, the output best-fit curve includes notable discrepancies with respect to the overall behavior of the empirical data. Although the developed method failed to provide us with an acceptable fit to the EDGES, the process is entirely independent of the data and can be used for future released observational data sets. Furthermore, since ARES is an open-source Python module, it is possible to update the code such that it encompasses any arbitrary non-standard physics scenario. This investigation is reserved for future studies.

In summary, theoretical predictions of the influence of non-standard physics on global 21cm signal will result in the construction of a framework to decide whether the precision of prospective experiments is sufficient for observing non-standard effects.

We faced certain limitations while working on this research. The majority of those are associated with the implementation of the Python script. A strongly limiting obstacle is related to the ARES's run-time, which is in the order of a few seconds per each simulation (approximately 4 to 5 seconds for different combinations of parameters). Given that ARES is computationally heavy, any iterative algorithm demanding to run ARES on each step is likely to require strong computational resources<sup>1</sup>. This was the main reason that led us to combine the MCMC with LM in order to have a more efficient chain and guarantee its

---

<sup>1</sup>As an example, the run time for the MCMC results presented in chapter 5 was approximately 13 hours.

convergence.

In future studies, we plan to take the analysis further and include a realistic noise model rather than an approximation. Subsequently, we shall incorporate certain non-standard effects into the ARES simulations. The same methodology will be executed to observe variations in the best-fit curve. The results will hopefully aid us to realize if existing and future observational data (like EDGES) contain the signatures of new physics and can be explained through these proposed theories.

# Bibliography

- [1] C. Carilli, S. Furlanetto, F. Briggs, M. Jarvis, S. Rawlings, and H. Falcke, “Probing the dark ages with the square kilometer array,” *New Astronomy Reviews*, vol. 48, no. 11, pp. 1029–1038, 2004. Science with the Square Kilometre Array.
- [2] S. G. Murray, B. Greig, A. Mesinger, J. B. Muñoz, Y. Qin, J. Park, and C. A. Watkinson, “21cmfast v3: A python-integrated c code for generating 3d realizations of the cosmic 21cm signal,” *arXiv preprint arXiv:2010.15121*, 2020.
- [3] J. R. Pritchard and A. Loeb, “21 cm cosmology in the 21st century,” *Reports on Progress in Physics*, vol. 75, no. 8, p. 086901, 2012.
- [4] C. Evoli, A. Mesinger, and A. Ferrara, “Unveiling the nature of dark matter with high redshift 21 cm line experiments,” *Journal of Cosmology and Astroparticle Physics*, vol. 2014, no. 11, p. 024, 2014.
- [5] M. Valdes, A. Ferrara, M. Mapelli, and E. Ripamonti, “Constraining dark matter through 21-cm observations,” *Monthly Notices of the Royal Astronomical Society*,

- vol. 377, no. 1, pp. 245–252, 2007.
- [6] R. H. Brandenberger, R. J. Danos, O. F. Hernandez, and G. P. Holder, “The 21 cm signature of cosmic string wakes,” *Journal of Cosmology and Astroparticle Physics*, vol. 2010, no. 12, p. 028, 2010.
- [7] S. Balaji, M. E. Ramirez-Quezada, and C. Boehm, “Radio sky reveals primordial electron-proton interactions,” *arXiv preprint arXiv:2204.13711*, 2022.
- [8] P. K. Natwariya and A. C. Nayak, “Bounds on sterile neutrino lifetime and mixing angle with active neutrinos by global 21 cm signal,” *Physics Letters B*, vol. 827, p. 136955, 2022.
- [9] O. F. Hernández, “Wouthuysen-field absorption trough in cosmic string wakes,” *Physical Review D*, vol. 90, no. 12, p. 123504, 2014.
- [10] I. F. Mirabel and L. F. Rodriguez, “Black holes at cosmic dawn in the redshifted 21cm signal of hi,” *New Astronomy Reviews*, p. 101642, 2022.
- [11] O. F. Hernández, “The global 21-cm signal of a network of cosmic string wakes,” *Monthly Notices of the Royal Astronomical Society*, vol. 508, no. 1, pp. 408–413, 2021.
- [12] J. D. Bowman, A. E. Rogers, R. A. Monsalve, T. J. Mozdzen, and N. Mahesh, “An absorption profile centred at 78 megahertz in the sky-averaged spectrum,” *Nature*, vol. 555, no. 7694, pp. 67–70, 2018.

- [13] J. Mirocha, “Decoding the x-ray properties of pre-reionization era sources,” *Monthly Notices of the Royal Astronomical Society*, vol. 443, no. 2, pp. 1211–1223, 2014.
- [14] N. Patra, R. Subrahmanyam, A. Raghunathan, and N. Udaya Shankar, “Saras: a precision system for measurement of the cosmic radio background and signatures from the epoch of reionization,” *Experimental Astronomy*, vol. 36, pp. 319–370, 2013.
- [15] X. Chen, “15 - mapping the universe with 21cm observations,” in *Big Data in Astronomy* (L. Kong, T. Huang, Y. Zhu, and S. Yu, eds.), pp. 379–406, Elsevier, 2020.
- [16] S. R. Furlanetto, S. P. Oh, and F. H. Briggs, “Cosmology at low frequencies: The 21 cm transition and the high-redshift universe,” *Physics reports*, vol. 433, no. 4-6, pp. 181–301, 2006.
- [17] K. M. Gerodias, “Simulations and data analysis for hirax and chord,” *McGill University*, 2023.
- [18] H. Shimabukuro, K. Hasegawa, A. Kuchinomachi, H. Yajima, and S. Yoshiura, “Exploring the cosmic dawn and epoch of reionization with the 21 cm line,” *Publications of the Astronomical Society of Japan*, vol. 75, no. Supplement\_1, pp. S1–S32, 2023.



- 
- [19] R. Barkana and A. Loeb, “In the beginning: the first sources of light and the reionization of the universe,” *Physics reports*, vol. 349, no. 2, pp. 125–238, 2001.
- [20] S. Wouthuysen, “On the excitation mechanism of the 21-cm (radio-frequency) interstellar hydrogen emission line,” *The Astronomical Journal*, vol. 57, pp. 31–32, 1952.
- [21] G. B. Field, “Excitation of the hydrogen 21-cm line,” *Proceedings of the IRE*, vol. 46, no. 1, pp. 240–250, 1958.
- [22] A. Liu, J. R. Pritchard, M. Tegmark, and A. Loeb, “Global 21 cm signal experiments: A designer’s guide,” *Physical Review D*, vol. 87, no. 4, p. 043002, 2013.
- [23] A. Cohen, A. Fialkov, R. Barkana, and R. A. Monsalve, “Emulating the global 21-cm signal from Cosmic Dawn and Reionization,” *Monthly Notices of the Royal Astronomical Society*, vol. 495, pp. 4845–4859, July 2020.
- [24] H. Trac, R. Cen, and A. Loeb, “Imprint of inhomogeneous hydrogen reionization on the temperature distribution of the intergalactic medium,” *The Astrophysical Journal*, vol. 689, no. 2, p. L81, 2008.
- [25] A. Mesinger and S. Furlanetto, “Efficient simulations of early structure formation and reionization,” *The Astrophysical Journal*, vol. 669, no. 2, p. 663, 2007.

- [26] T. R. Choudhury, M. G. Haehnelt, and J. Regan, “Inside-out or outside-in: the topology of reionization in the photon-starved regime suggested by  $\text{Ly}\alpha$  forest data,” *Monthly Notices of the Royal Astronomical Society*, vol. 394, no. 2, pp. 960–977, 2009.
- [27] M. A. Alvarez, M. Busha, T. Abel, and R. H. Wechsler, “Connecting reionization to the local universe,” *The Astrophysical Journal*, vol. 703, no. 2, p. L167, 2009.
- [28] R. M. Thomas, S. Zaroubi, B. Ciardi, A. H. Pawlik, P. Labropoulos, V. Jelić, G. Bernardi, M. A. Brentjens, A. De Bruyn, G. J. Harker, *et al.*, “Fast large-scale reionization simulations,” *Monthly Notices of the Royal Astronomical Society*, vol. 393, no. 1, pp. 32–48, 2009.
- [29] O. Zahn, M. Zaldarriaga, L. Hernquist, and M. McQuinn, “The influence of nonuniform reionization on the cmb,” *The Astrophysical Journal*, vol. 630, no. 2, p. 657, 2005.
- [30] C. H. Bye, S. K. Portillo, and A. Fialkov, “21cmvae: A very accurate emulator of the 21 cm global signal,” *The Astrophysical Journal*, vol. 930, no. 1, p. 79, 2022.
- [31] H. Bevins, W. Handley, A. Fialkov, E. de Lera Acedo, and K. Javid, “Globalemu: a novel and robust approach for emulating the sky-averaged 21-cm signal from the cosmic dawn and epoch of reionization,” *Monthly Notices of the Royal Astronomical Society*, vol. 508, no. 2, pp. 2923–2936, 2021.

- 
- [32] A. Mesinger, S. Furlanetto, and R. Cen, “21cmfast: a fast, seminumerical simulation of the high-redshift 21-cm signal,” *Monthly Notices of the Royal Astronomical Society*, vol. 411, no. 2, pp. 955–972, 2011.
- [33] “Documentation of 21cmFast.” Retrieved from <https://21cmfast.readthedocs.io/en/latest/>.
- [34] “21cmFast GitHub Repository.” Retrieved from <https://github.com/21cmfast/21cmFAST>.
- [35] “Documentation of ARES.” Retrieved from <https://ares.readthedocs.io/en/latest/>.
- [36] “ARES GitHub Repository.” Retrieved from <https://github.com/mirochaj/ares>.
- [37] J. Mirocha, S. R. Furlanetto, and G. Sun, “The global 21-cm signal in the context of the high- $z$  galaxy luminosity function,” *Monthly Notices of the Royal Astronomical Society*, vol. 464, no. 2, pp. 1365–1379, 2017.
- [38] J. Mirocha, C. Mason, and D. P. Stark, “Effects of self-consistent rest-ultraviolet colours in semi-empirical galaxy formation models,” *Monthly Notices of the Royal Astronomical Society*, vol. 498, no. 2, pp. 2645–2661, 2020.

- [39] J. Mirocha, “Prospects for distinguishing galaxy evolution models with surveys at redshifts  $z \geq 4$ ,” *Monthly Notices of the Royal Astronomical Society*, vol. 499, no. 3, pp. 4534–4544, 2020.
- [40] J. Mirocha, R. H. Mebane, S. R. Furlanetto, K. Singal, and D. Trinh, “Unique signatures of population iii stars in the global 21-cm signal,” *Monthly Notices of the Royal Astronomical Society*, vol. 478, no. 4, pp. 5591–5606, 2018.
- [41] J. Mirocha, S. Skory, J. O. Burns, and J. H. Wise, “Optimized multi-frequency spectra for applications in radiative feedback and cosmological reionization,” *The Astrophysical Journal*, vol. 756, no. 1, p. 94, 2012.
- [42] S. J. Clark, B. Dutta, Y. Gao, Y.-Z. Ma, and L. E. Strigari, “21 cm limits on decaying dark matter and primordial black holes,” *Physical Review D*, vol. 98, no. 4, p. 043006, 2018.
- [43] P. K. Natwariya, “21 cm line astronomy and constraining new physics,” *arXiv preprint arXiv:2301.02655*, 2023.
- [44] Y. Ali-Haïmoud, E. D. Kovetz, and M. Kamionkowski, “Merger rate of primordial black-hole binaries,” *Physical Review D*, vol. 96, no. 12, p. 123523, 2017.

- 
- [45] S. J. Clark, B. Dutta, Y. Gao, Y.-Z. Ma, and L. E. Strigari, “21 cm limits on decaying dark matter and primordial black holes,” *Physical Review D*, vol. 98, no. 4, p. 043006, 2018.
- [46] A. Halder and S. Banerjee, “Bounds on abundance of primordial black hole and dark matter from edges 21-cm signal,” *Physical Review D*, vol. 103, no. 6, p. 063044, 2021.
- [47] A. Chatterjee, P. Dayal, T. R. Choudhury, and A. Hutter, “Ruling out 3 kev warm dark matter using 21 cm edges data,” *Monthly Notices of the Royal Astronomical Society*, vol. 487, no. 3, pp. 3560–3567, 2019.
- [48] M. Pagano and R. Brandenberger, “The 21 cm signature of a cosmic string loop,” *Journal of Cosmology and Astroparticle Physics*, vol. 2012, no. 05, p. 014, 2012.
- [49] S. R. Furlanetto, S. P. Oh, and E. Pierpaoli, “Effects of dark matter decay and annihilation on the high-redshift 21 cm background,” *Phys. Rev. D*, vol. 74, p. 103502, Nov 2006.
- [50] X. Chen and M. Kamionkowski, “Particle decays during the cosmic dark ages,” *Phys. Rev. D*, vol. 70, p. 043502, Aug 2004.
- [51] A. V. Belikov and D. Hooper, “How dark matter reionized the universe,” *Phys. Rev. D*, vol. 80, p. 035007, Aug 2009.

- [52] J. O. Burns, S. Bale, N. Bassett, J. Bowman, R. Bradley, A. Fialkov, S. Furlanetto, M. Hecht, M. Klein-Wolt, C. Lonsdale, *et al.*, “Dark cosmology: Investigating dark matter & exotic physics in the dark ages using the redshifted 21-cm global spectrum,” *arXiv preprint arXiv:1902.06147*, 2019.
- [53] K. K. Boddy, M. Lisanti, S. D. McDermott, N. L. Rodd, C. Weniger, Y. Ali-Haïmoud, M. Buschmann, I. Cholis, D. Croon, A. L. Erickcek, *et al.*, “Snowmass2021 theory frontier white paper: Astrophysical and cosmological probes of dark matter,” *Journal of High Energy Astrophysics*, vol. 35, pp. 112–138, 2022.
- [54] P. K. Natwariya and A. C. Nayak, “Bounds on sterile neutrino lifetime and mixing angle with active neutrinos by global 21 cm signal,” *Physics Letters B*, vol. 827, p. 136955, 2022.
- [55] A. Schneider, “Constraining noncold dark matter models with the global 21-cm signal,” *Physical Review D*, vol. 98, no. 6, p. 063021, 2018.
- [56] J. B. Munoz, Y. Qin, A. Mesinger, S. G. Murray, B. Greig, and C. Mason, “The impact of the first galaxies on cosmic dawn and reionization,” *Monthly Notices of the Royal Astronomical Society*, vol. 511, no. 3, pp. 3657–3681, 2022.
- [57] K. Bechtol, S. Birrer, F.-Y. Cyr-Racine, K. Schutz, S. Adhikari, M. Amin, A. Banerjee, S. Bird, N. Blinov, K. K. Boddy, *et al.*, “Snowmass2021 cosmic frontier white paper: dark matter physics from halo measurements,” *arXiv preprint arXiv:2203.07354*, 2022.

- [58] B. Cyr, *Cosmological Implications of Topological Defects*. PhD thesis, McGill University (Canada), 2022.
- [59] R. Brandenberger, B. Cyr, and R. Shi, “Constraints on superconducting cosmic strings from the global 21-cm signal before reionization,” *Journal of Cosmology and Astroparticle Physics*, vol. 2019, no. 09, p. 009, 2019.
- [60] H. Jiao, R. Brandenberger, and A. Refregier, “Early structure formation from cosmic string loops in light of early jwst observations,” *arXiv preprint arXiv:2304.06429*, 2023.
- [61] A. Vilenkin and E. P. S. Shellard, *Cosmic strings and other topological defects*. Cambridge University Press, 1994.
- [62] O. F. Hernández and R. H. Brandenberger, “The 21 cm signature of shock heated and diffuse cosmic string wakes,” *Journal of Cosmology and Astroparticle Physics*, vol. 2012, no. 07, p. 032, 2012.
- [63] B. Cyr, H. Jiao, and R. Brandenberger, “Massive black holes at high redshifts from superconducting cosmic strings,” *Monthly Notices of the Royal Astronomical Society*, vol. 517, no. 2, pp. 2221–2230, 2022.
- [64] R. Brandenberger, B. Cyr, and T. Schaeffer, “On the possible enhancement of the global 21-cm signal at reionization from the decay of cosmic string cusps,” *Journal of Cosmology and Astroparticle Physics*, vol. 2019, no. 04, p. 020, 2019.

- [65] A. Berndsen, L. Pogosian, and M. Wyman, “Correlations between 21-cm radiation and the cosmic microwave background from active sources,” *Monthly Notices of the Royal Astronomical Society*, vol. 407, no. 2, pp. 1116–1122, 2010.
- [66] B. Cyr, J. Chluba, and S. K. Acharya, “Constraints on the spectral signatures of superconducting cosmic strings,” *arXiv preprint arXiv:2305.09816*, 2023.
- [67] R. Thériault, J. T. Mirocha, and R. Brandenberger, “Global 21cm absorption signal from superconducting cosmic strings,” *Journal of Cosmology and Astroparticle Physics*, vol. 2021, no. 10, p. 046, 2021.
- [68] C. Ringeval and T. Suyama, “Stochastic gravitational waves from cosmic string loops in scaling,” *Journal of Cosmology and Astroparticle Physics*, vol. 2017, no. 12, p. 027, 2017.
- [69] P. Yaninska, “Albatros front-end electronics development,” *MGill University*, 2023.
- [70] T. H. Moso, “Low-frequency observations of the radio sky from marion island,” *University of Kwa-Zulu Natal*, 2021.
- [71] P. Villanueva-Domingo, “Shedding light on dark matter through 21 cm cosmology and reionization constraints,” *arXiv preprint arXiv:2112.08201*, 2021.
- [72] S. Singh, J. Nambissan T, R. Subrahmanyam, N. Udaya Shankar, B. Girish, A. Raghunathan, R. Somashekar, K. Srivani, and M. Sathyanarayana Rao, “On the



- detection of a cosmic dawn signal in the radio background,” *Nature Astronomy*, vol. 6, no. 5, pp. 607–617, 2022.
- [73] A. Mesinger, *The Cosmic 21-cm Revolution: Charting the first billion years of our Universe*. IoP Publishing, 2019.
- [74] G. J. Harker, J. R. Pritchard, J. O. Burns, and J. D. Bowman, “An mcmc approach to extracting the global 21-cm signal during the cosmic dawn from sky-averaged radio observations,” *Monthly Notices of the Royal Astronomical Society*, vol. 419, no. 2, pp. 1070–1084, 2012.
- [75] P. Shaver, R. Windhorst, P. Madau, and A. De Bruyn, “Can the reionization epoch be detected as a global signature in the cosmic background?,” *arXiv preprint astro-ph/9901320*, 1999.
- [76] S. Zuo, X. Chen, R. Ansari, and Y. Lu, “21 cm signal recovery via robust principal component analysis,” *The Astronomical Journal*, vol. 157, no. 1, p. 4, 2018.
- [77] Q.-Z. Huang, F.-Q. Wu, R. Ansari, and X. Chen, “Extracting 21 cm signal by frequency and angular filtering,” *Research in Astronomy and Astrophysics*, vol. 18, no. 9, p. 114, 2018.
- [78] T. L. Makinen, L. Lancaster, F. Villaescusa-Navarro, P. Melchior, S. Ho, L. Perreault-Levasseur, and D. N. Spergel, “deep21: a deep learning method for 21 cm foreground

- removal,” *Journal of Cosmology and Astroparticle Physics*, vol. 2021, no. 04, p. 081, 2021.
- [79] M. Choudhury and A. Datta, “Foreground subtraction and signal reconstruction in redshifted 21cm global signal experiments using artificial neural networks,” *Proceedings of the International Astronomical Union*, vol. 12, no. S333, pp. 280–283, 2017.
- [80] G. Kaur, “21 cm cosmology: signal extraction using machine learning,” 2022.
- [81] M. Choudhury, A. Datta, and A. Chakraborty, “Extracting the 21 cm global signal using artificial neural networks,” *Monthly Notices of the Royal Astronomical Society*, vol. 491, no. 3, pp. 4031–4044, 2020.
- [82] F. De Gasperin, M. Mevius, D. Rafferty, H. Intema, and R. Fallows, “The effect of the ionosphere on ultra-low-frequency radio-interferometric observations,” *Astronomy & Astrophysics*, vol. 615, p. A179, 2018.
- [83] A. P. Rao, “Chapter 16: Ionospheric effects in radio astronomy,”
- [84] E. Shen, D. Anstey, E. de Lera Acedo, A. Fialkov, and W. Handley, “Quantifying ionospheric effects on global 21-cm observations,” *Monthly Notices of the Royal Astronomical Society*, vol. 503, no. 1, pp. 344–353, 2021.

- [85] E. Shen, D. Anstey, E. de Lera Acedo, and A. Fialkov, “Bayesian data analysis for sky-averaged 21-cm experiments in the presence of ionospheric effects,” *Monthly Notices of the Royal Astronomical Society*, vol. 515, no. 3, pp. 4565–4573, 2022.
- [86] J. O. Burns, R. Bradley, K. Tauscher, S. Furlanetto, J. Mirocha, R. Monsalve, D. Rapetti, W. Purcell, D. Newell, D. Draper, *et al.*, “A space-based observational strategy for characterizing the first stars and galaxies using the redshifted 21 cm global spectrum,” *The Astrophysical Journal*, vol. 844, no. 1, p. 33, 2017.
- [87] J. O. Burns, J. Lazio, S. Bale, J. Bowman, R. Bradley, C. Carilli, S. Furlanetto, G. Harker, A. Loeb, and J. Pritchard, “Probing the first stars and black holes in the early universe with the dark ages radio explorer (dare),” *Advances in Space Research*, vol. 49, no. 3, pp. 433–450, 2012.
- [88] L. V. Koopmans, R. Barkana, M. Bentum, G. Bernardi, A.-J. Boonstra, J. Bowman, J. Burns, X. Chen, A. Datta, H. Falcke, *et al.*, “Peering into the dark (ages) with low-frequency space interferometers: Using the 21-cm signal of neutral hydrogen from the infant universe to probe fundamental (astro) physics,” *Experimental Astronomy*, vol. 51, pp. 1641–1676, 2021.
- [89] Y. Shi, F. Deng, Y. Xu, F. Wu, Q. Yan, and X. Chen, “Lunar orbit measurement of the cosmic dawn’s 21 cm global spectrum,” *The Astrophysical Journal*, vol. 929, no. 1, p. 32, 2022.

- [90] T. C. Voytek, A. Natarajan, J. M. J. García, J. B. Peterson, and O. López-Cruz, “Probing the dark ages at  $z \sim 20$ : The sci-hi 21 cm all-sky spectrum experiment,” *The Astrophysical Journal Letters*, vol. 782, no. 1, p. L9, 2014.
- [91] L. Philip, *The Design, Construction and Deployment of PRIZM*. PhD thesis, University of KwaZulu-Natal, Westville, 2019.
- [92] J. Cumner, E. De Lera Acedo, D. de Villiers, D. Anstey, C. Kolitsidas, B. Gurdon, N. Fagnoni, P. Alexander, G. Bernardi, H. Bevins, *et al.*, “Radio antenna design for sky-averaged 21 cm cosmology experiments: the reach case,” *Journal of Astronomical Instrumentation*, vol. 11, no. 01, p. 2250001, 2022.
- [93] L. Philip, Z. Abdurashidova, H. Chiang, N. Ghazi, A. Gumba, H. Heilgendorff, J. Jáuregui-García, K. Malepe, C. Nunhokee, J. Peterson, *et al.*, “Probing radio intensity at high- $z$  from marion: 2017 instrument,” *Journal of Astronomical Instrumentation*, vol. 8, no. 02, p. 1950004, 2019.
- [94] M. Sokolowski, R. B. Wayth, and M. Lewis, “The statistics of low frequency radio interference at the munchison radio-astronomy observatory,” in *2015 IEEE Global Electromagnetic Compatibility Conference (GEMCCON)*, pp. 1–6, IEEE, 2015.
- [95] D. Price, L. Greenhill, A. Fialkov, G. Bernardi, H. Garsden, B. Barsdell, J. Kocz, M. Anderson, S. Bourke, J. Craig, *et al.*, “Design and characterization of the large-

- aperture experiment to detect the dark age (leda) radiometer systems,” *Monthly Notices of the Royal Astronomical Society*, vol. 478, no. 3, pp. 4193–4213, 2018.
- [96] J. Burns, G. Hallinan, T.-C. Chang, M. Anderson, J. Bowman, R. Bradley, S. Furlanetto, A. Hegedus, J. Kasper, J. Kocz, *et al.*, “A lunar farside low radio frequency array for dark ages 21-cm cosmology,” *arXiv preprint arXiv:2103.08623*, 2021.
- [97] J. Burns, S. Bale, R. Bradley, Z. Ahmed, S. Allen, J. Bowman, S. Furlanetto, R. MacDowall, J. Mirocha, B. Nhan, *et al.*, “Global 21-cm cosmology from the farside of the moon,” *arXiv preprint arXiv:2103.05085*, 2021.
- [98] N. Patra, R. Wayth, M. Sokolowski, D. Price, B. McKinley, and D. Kenney, “Hypereion-a precision system for the detection of the absorption profile centred at 78 mhz in the radio background spectrum,” *Publications of the Astronomical Society of Australia*, pp. 1–23.
- [99] N. Patra, C. Day, and A. Parsons, “Radio background measurements at long wavelengths,” in *2017 XXXIInd General Assembly and Scientific Symposium of the International Union of Radio Science (URSI GASS)*, pp. 1–4, IEEE, 2017.
- [100] “Edges: Experiment to detect the global eor signature.” Retrieved from <https://www.haystack.mit.edu/astronomy/astronomy-projects/edges-experiment-to-detect-the-global-eor-signature/>.

- [101] “Experiment to detect the global eor signature (edges).” Retrieved from <https://loco.lab.asu.edu/edges/>.
- [102] A. E. Rogers and J. D. Bowman, “Absolute calibration of a wideband antenna and spectrometer for sky noise spectral index measurements,” *arXiv preprint arXiv:1209.1106*, 2012.
- [103] R. A. Monsalve, A. E. Rogers, J. D. Bowman, and T. J. Mozdzen, “Calibration of the edges high-band receiver to observe the global 21 cm signature from the epoch of reionization,” *The Astrophysical Journal*, vol. 835, no. 1, p. 49, 2017.
- [104] J. D. Bowman and A. E. Rogers, “A lower limit of  $\delta z > 0.06$  for the duration of the reionization epoch,” *Nature*, vol. 468, no. 7325, pp. 796–798, 2010.
- [105] R. A. Monsalve, A. E. Rogers, J. D. Bowman, and T. J. Mozdzen, “Results from edges high-band. i. constraints on phenomenological models for the global 21 cm signal,” *The Astrophysical Journal*, vol. 847, no. 1, p. 64, 2017.
- [106] L. V. Koopmans, R. Barkana, M. Bentum, G. Bernardi, A.-J. Boonstra, J. Bowman, J. Burns, X. Chen, A. Datta, H. Falcke, *et al.*, “Peering into the dark (ages) with low-frequency space interferometers: Using the 21-cm signal of neutral hydrogen from the infant universe to probe fundamental (astro) physics,” *Experimental Astronomy*, vol. 51, pp. 1641–1676, 2021.

- [107] J. D. Bowman, A. E. Rogers, and J. N. Hewitt, “Toward empirical constraints on the global redshifted 21 cm brightness temperature during the epoch of reionization,” *The Astrophysical Journal*, vol. 676, no. 1, p. 1, 2008.
- [108] S. Singh, R. Subrahmanyam, N. U. Shankar, M. S. Rao, B. Girish, A. Raghunathan, R. Somashekar, and K. Srivani, “Saras 2: a spectral radiometer for probing cosmic dawn and the epoch of reionization through detection of the global 21-cm signal,” *Experimental Astronomy*, vol. 45, pp. 269–314, 2018.
- [109] S. Singh, R. Subrahmanyam, N. U. Shankar, M. S. Rao, A. Fialkov, A. Cohen, R. Barkana, B. Girish, A. Raghunathan, R. Somashekar, *et al.*, “Saras 2 constraints on global 21 cm signals from the epoch of reionization,” *The Astrophysical Journal*, vol. 858, no. 1, p. 54, 2018.
- [110] S. Singh, R. Subrahmanyam, N. U. Shankar, M. S. Rao, A. Fialkov, A. Cohen, R. Barkana, B. Girish, A. Raghunathan, R. Somashekar, *et al.*, “First results on the epoch of reionization from first light with saras 2,” *The Astrophysical Journal Letters*, vol. 845, no. 2, p. L12, 2017.
- [111] R. Subrahmanyam, R. Somashekar, N. U. Shankar, S. Singh, A. Raghunathan, B. Girish, K. Srivani, and M. S. Rao, “Saras 3 cd/eor radiometer: design and performance of the receiver,” *Experimental Astronomy*, vol. 51, pp. 193–234, 2021.

- [112] H. Bevens, A. Fialkov, E. de Lera Acedo, W. Handley, S. Singh, R. Subrahmanyam, and R. Barkana, “Astrophysical constraints from the saras 3 non-detection of the cosmic dawn sky-averaged 21-cm signal,” *Nature Astronomy*, vol. 6, no. 12, pp. 1473–1483, 2022.
- [113] J. B. Peterson, T. C. Voytek, A. Natarajan, J. M. J. Garcia, and O. Lopez-Cruz, “Measuring the 21 cm global brightness temperature spectrum during the dark ages with the sci-hi experiment,” *arXiv preprint arXiv:1409.2774*, 2014.
- [114] E. de Lera Acedo, D. de Villiers, N. Razavi-Ghods, W. Handley, A. Fialkov, A. Magro, D. Anstey, H. Bevens, R. Chiello, J. Cumner, *et al.*, “The reach radiometer for detecting the 21-cm hydrogen signal from redshift  $z$  7.5–28,” *Nature Astronomy*, vol. 6, no. 8, pp. 984–998, 2022.
- [115] E. de Lera Acedo, “Reach: Radio experiment for the analysis of cosmic hydrogen,” in *2019 International Conference on Electromagnetics in Advanced Applications (ICEAA)*, pp. 0626–0629, IEEE, 2019.
- [116] R. A. Monsalve, V. Bidula, R. Bustos, C. H. Bye, H. C. Chiang, M. Diaz, X. Guo, I. Hendriksen, E. Horneker, F. Lucero, H. Mani, F. McGee, F. P. Mena, M. Pessoa, G. Prabhakar, O. Restpero, J. L. Sievers, and N. Thyagarajan, “Mapper of the IGM Spin Temperature (MIST): Instrument Overview,” 2023. [Manuscript in preparation].



- [117] I. T. Hendricksen, “Development of a Highly Integrated and Power-Efficient Miniature Version of the MIST Analog Chain,” *Bulletin of the AAS*, vol. 53, jan 11 2021. <https://baas.aas.org/pub/2021n1i533p04>.
- [118] “Mist - mapper of the igm spin temperature.” Retrieved from <https://www.physics.mcgill.ca/mist/>.
- [119] M. Spinelli, G. Kyriakou, G. Bernardi, P. Bolli, L. Greenhill, A. Fialkov, and H. Garsden, “Antenna beam characterization for the global 21-cm experiment leda and its impact on signal model parameter reconstruction,” *Monthly Notices of the Royal Astronomical Society*, vol. 515, no. 2, pp. 1580–1597, 2022.
- [120] G. Bernardi, M. McQuinn, and L. Greenhill, “Foreground model and antenna calibration errors in the measurement of the sky-averaged  $\lambda 21$  cm signal at  $z = 20$ ,” *The Astrophysical Journal*, vol. 799, no. 1, p. 90, 2015.
- [121] L. J. Greenhill, J. Kocz, B. Barsdell, M. Clark, L. Collaboration, *et al.*, “The cosmological dark age and high-throughput real-time computing (leda),” *Exascale Radio Astronomy*, vol. 2, p. 10301, 2014.
- [122] L. J. Greenhill, D. Werthimer, G. Taylor, S. Ellingson, L. Collaboration, *et al.*, “Hi at  $z = 20$ : The large aperture experiment to detect the dark ages,” in *American Astronomical Society Meeting Abstracts# 220*, vol. 220, pp. 104–03, 2012.

- [123] N. Patra, D. de Boer, A. Parsons, C. Day, D. Shen, T. Bhattacharyya, and K. Kundert, “Antenna systems for 21 cm cosmology,” in *2017 International Conference on Electromagnetics in Advanced Applications (ICEAA)*, pp. 1116–1119, Sept. 2017.
- [124] M. Sokolowski, S. E. Tremblay, R. B. Wayth, S. J. Tingay, N. Clarke, P. Roberts, M. Waterson, R. D. Ekers, P. Hall, M. Lewis, *et al.*, “Bighorns-broadband instrument for global hydrogen reionisation signal,” *Publications of the Astronomical Society of Australia*, vol. 32, p. e004, 2015.
- [125] R. Barkana, “Possible interaction between baryons and dark-matter particles revealed by the first stars,” *Nature*, vol. 555, no. 7694, pp. 71–74, 2018.
- [126] J. B. Muñoz and A. Loeb, “A small amount of mini-charged dark matter could cool the baryons in the early universe,” *Nature*, vol. 557, no. 7707, pp. 684–686, 2018.
- [127] J. B. Muñoz, C. Dvorkin, and A. Loeb, “21-cm fluctuations from charged dark matter,” *Physical review letters*, vol. 121, no. 12, p. 121301, 2018.
- [128] A. Fialkov, R. Barkana, and A. Cohen, “Constraining baryon–dark-matter scattering with the cosmic dawn 21-cm signal,” *Physical review letters*, vol. 121, no. 1, p. 011101, 2018.

- 
- [129] A. Berlin, D. Hooper, G. Krnjaic, and S. D. McDermott, “Severely constraining dark-matter interpretations of the 21-cm anomaly,” *Physical review letters*, vol. 121, no. 1, p. 011102, 2018.
- [130] M. S. Mahdawi and G. R. Farrar, “Constraints on dark matter with a moderately large and velocity-dependent dm-nucleon cross-section,” *Journal of Cosmology and Astroparticle Physics*, vol. 2018, no. 10, p. 007, 2018.
- [131] C. Feng and G. Holder, “Enhanced global signal of neutral hydrogen due to excess radiation at cosmic dawn,” *The Astrophysical Journal Letters*, vol. 858, no. 2, p. L17, 2018.
- [132] S. Witte, P. Villanueva-Domingo, S. Gariazzo, O. Mena, and S. Palomares-Ruiz, “Edges result versus cmb and low-redshift constraints on ionization histories,” *Physical Review D*, vol. 97, no. 10, p. 103533, 2018.
- [133] A. Chatterjee, T. R. Choudhury, and S. Mitra, “Cosmoreionmc: a package for estimating cosmological and astrophysical parameters using cmb, lyman- $\alpha$  absorption, and global 21 cm data,” *Monthly Notices of the Royal Astronomical Society*, vol. 507, no. 2, pp. 2405–2422, 2021.
- [134] J. Mirocha, G. J. Harker, and J. O. Burns, “Interpreting the global 21-cm signal from high redshifts. ii. parameter estimation for models of galaxy formation,” *The Astrophysical Journal*, vol. 813, no. 1, p. 11, 2015.

- [135] M. Choudhury, A. Chatterjee, A. Datta, and T. R. Choudhury, “Using artificial neural networks to extract the 21-cm global signal from the edges data,” *Monthly Notices of the Royal Astronomical Society*, vol. 502, no. 2, pp. 2815–2825, 2021.
- [136] J. R. Pritchard and A. Loeb, “Constraining the unexplored period between the dark ages and reionization with observations of the global 21 cm signal,” *Physical Review D*, vol. 82, no. 2, p. 023006, 2010.
- [137] “MCMC Overview.” Retrieved from <https://github.com/sievers/phys512-2021/blob/main/notes/mcmc.pdf>.
- [138] A. Bera, R. Ghara, A. Chatterjee, K. K. Datta, and S. Samui, “Studying cosmic dawn using redshifted HI 21-cm signal: A brief review,” *Journal of Astrophysics and Astronomy*, vol. 44, no. 1, p. 10, 2023.
- [139] P. C. Crane and P. J. Napier, “Sensitivity,” in *Synthesis imaging in radio astronomy*, vol. 6, p. 139, 1989.
- [140] J. Wrobel and R. Walker, “Sensitivity,” in *Synthesis imaging in radio astronomy II*, vol. 180, p. 171, 1999.
- [141] A. Cohen, A. Fialkov, R. Barkana, and M. Lotem, “Charting the parameter space of the global 21-cm signal,” *Monthly Notices of the Royal Astronomical Society*, vol. 472, no. 2, pp. 1915–1931, 2017.

- 
- [142] J. Mirocha, G. J. Harker, and J. O. Burns, “Interpreting the global 21-cm signal from high redshifts. ii. parameter estimation for models of galaxy formation,” *The Astrophysical Journal*, vol. 813, no. 1, p. 11, 2015.
- [143] A. Liu and A. R. Parsons, “Constraining cosmology and ionization history with combined 21 cm power spectrum and global signal measurements,” *Monthly Notices of the Royal Astronomical Society*, vol. 457, no. 2, pp. 1864–1877, 2016.